



KIT SCIENTIFIC REPORTS 7669

Numerical study of void drift in rod bundle with subchannel and CFD codes

Bo Pang

Bo Pang

Numerical study of void drift in rod bundle with subchannel and CFD codes

Karlsruhe Institute of Technology
KIT SCIENTIFIC REPORTS 7669

Numerical study of void drift in rod bundle with subchannel and CFD codes

von
Bo Pang

Report-Nr. KIT-SR 7669

Dissertation, Karlsruher Institut für Technologie
Fakultät für Maschinenbau, 2013
Referenten: Prof. Dr.-Ing. Xu Cheng
Prof. Dr.-Ing. Thomas Schulenberg

Impressum



Karlsruher Institut für Technologie (KIT)
KIT Scientific Publishing
Straße am Forum 2
D-76131 Karlsruhe

KIT Scientific Publishing is a registered trademark of Karlsruhe
Institute of Technology. Reprint using the book cover is not allowed.

www.ksp.kit.edu



*This document – excluding the cover – is licensed under the
Creative Commons Attribution-Share Alike 3.0 DE License*

(CC BY-SA 3.0 DE): <http://creativecommons.org/licenses/by-sa/3.0/de/>



*The cover page is licensed under the Creative Commons
Attribution-No Derivatives 3.0 DE License (CC BY-ND 3.0 DE):*

<http://creativecommons.org/licenses/by-nd/3.0/de/>

Print on Demand 2014

ISSN 1869-9669

ISBN 978-3-7315-0219-7

DOI: 10.5445/KSP/1000041053

Numerical study of void drift in rod bundle with subchannel and CFD codes

Zur Erlangung des akademischen Grades
Doktor der Ingenieurwissenschaften
der Fakultät für Maschinenbau
Karlsruher Institut für Technologie (KIT)

genehmigte
Dissertation
von

Dipl.-Ing. Bo Pang
aus Hubei, VR China

Tag der mündlichen Prüfung: 13. September 2013

Hauptreferent: Prof. Dr.-Ing. Xu Cheng

Korreferent: Prof. Dr.-Ing. Thomas Schulenberg

Karlsruher Institut für Technologie (KIT)
Institut für Fusionstechnologie und Reaktortechnik (IFRT)
Institut für Kern- und Energietechnik (IKET)

Acknowledgements

It is a true pleasure to thank all the people who made this thesis possible. First, I want to greatly thank Prof. Xu Cheng for his guidance and patience during the past several years. Without his help and support, it is impossible for me to accomplish the objectives of this study. I am very grateful to all the help and especially all the encouragement he gave me.

I also want to give my special thanks to Prof. Thomas Schulenberg. Not only his valuable advises, but also his help and encouragement through the whole project work, are greatly appreciated. The enlightening discussions with him helped me greatly to finish the thesis.

Next, my thanks go to Dr. Ivan Otic. His kindly help and valuable advises pushed my understanding of CFD simulation to a whole new horizon. Furthermore, I want to thank all the colleagues in IFRT for their helpful discussions and the great atmosphere we shared in the institute.

For the financial help provided by the German Federal Ministry of Education and Research (BMBF) I owe my grateful thanks. I also want to pay my sincere appreciation to KAERI (Korea Atomic Energy Research Institute) for providing the MATRA code.

I want to thank my wife Ting and all the members of my family for their love and consistent supports during my study in Germany. I wish all of you good health and happiness forever! Last but not least, I want to give my son Yifan my deepest thanks and all the best wishes in the world. You give me the greatest courage to face all the challenges in life!

Karlsruhe, May 13. 2014

Bo Pang

Abstract

Prediction of critical heat flux (CHF) in rod bundle geometry requires information on local flow conditions in subchannels, which depend strongly on the modeling of interchannel mixing. Under two-phase flow conditions, the interchannel mixing between two adjacent subchannels can be decomposed into three elemental components [47, 72]: namely turbulent mixing (TM), diversion cross flow (DC) and void drift (VD). Turbulent mixing occurs from stochastic flow fluctuations, whereas diversion cross flow is induced by a lateral mean pressure difference between interacting subchannels. However, physical mechanism of void drift is not yet well understood. The present study is devoted to simulation and analysis of void drift in rod bundle geometry with the subchannel analysis code MATRA [107] (modified based on COBRA-IV-I [86]) and the CFD code Ansys CFX [2].

In subchannel analysis, diversion cross flow is directly solved with a transverse momentum equation. Constitutive models are required then for turbulent mixing and void drift. The modeling approach currently available in MATRA is based on the equal-volume-exchange (EV) turbulent mixing incorporating void drift (VD) concept proposed by Lahey and Moody [47] (hence referred to as the EVVD model). This is a phenomenological approach based on the experimentally observed strong tendency of a two-phase system approaching a fully developed, equilibrium state. Once this state is established, net exchange due to interchannel mixing ceases. However, one noticeable drawback of the EVVD model is the combined modeling of the non-directional mixing effect turbulent mixing and the directional mixing effect void drift with the same effective mixing velocity. The two mixing effects are not clearly separated in the EVVD model. Nevertheless, the EVVD model is simple to apply and hence widely adopted in state-of-the-art subchannel analysis codes, provided the void fraction distribution at the equilibrium state is known. In MATRA, a modified Levy's model [51] with introduction of a void drift correction factor K_{VD} by Hwang et al. [33] is implemented, in order to determine the void fraction distribution at equilibrium state. However, this model considers only influence of mass flux distribution on the void fraction distribution at equilibrium state. Two types of the EVVD model are available in MATRA with different approaches applied to determine K_{VD} . Both types imply that the gaseous phase (void) tends to accumulate in subchannels with larger mass flux at the equilibrium state. However, separation of turbulent mixing with void drift has not been carried out in MATRA. For assessment of the EVVD model in MATRA, recalculation of selected rod bundle benchmark test cases under both BWR and PWR pressure levels was performed. It revealed that for application to bubbly flow regime under PWR pressure level, the EVVD model in MATRA needs improvement. The tendency of higher void fraction in subchannels of larger mass flux is not valid in the bubbly flow regime under PWR pressure level.

Improvement of the EVVD model should be performed in two aspects. First, turbulent mixing and void drift should be separated with individual effective mixing velocities. Second, the model to determine the void fraction distribution at equilibrium state should be extended, so that influence of geometrical difference between two interacting subchannels is also considered. In the current study, a new phenomenological description of the two-phase interchannel mixing was proposed based on the concept of equal-mass-exchange (EM) turbulent mixing

incorporating void drift (VD). This new type of interchannel mixing model is hence referred to as the EMVD model, with which the three elemental mixing effects, i.e. turbulent mixing, diversion cross flow and void drift, are separated from each other. Lahey et al.'s proposal [47] of approaching an equilibrium state was adopted to model void drift, for which the void fraction distribution at equilibrium state and an effective mixing velocity due to void drift are required.

In order to determine the above two key parameters of void drift, CFD approach was used to simulate two-phase interchannel mixing in rod bundle geometry. The Eulerian two-fluid model was employed to describe the bubbly flow behavior in rod bundle. The liquid phase was modeled as a continuous phase, while the gaseous phase was modeled as dispersed bubbles with a constant bubble diameter. Validation of the employed CFD model was performed by recalculating two-phase interchannel mixing experiments conducted by van der Ros [101] and Gonzalez-Santalo et al. [29]. It revealed that modeling of lift force has strong impacts on the predicted two-phase interchannel mixing. Unfortunately, no general applicable lift force models are available. In the current study, a constant lift force coefficient of 0.05 was recommended based on a detailed sensitivity study.

With the validated CFD model, simulation and analysis of interchannel mixing in the bubbly flow regime under PWR pressure level (157 bars) was carried out. In the first set of simulations, the void fraction distribution at equilibrium state was determined using a cyclic boundary condition. Both mass flux and geometry effects on the void fraction distribution at equilibrium state were considered. A new, extended Levy's model [51] was proposed to calculate the void fraction distribution at equilibrium state. The second set of simulations denoted to determine a dimensionless void drift coefficient β_{VD} , which characterizes the effective mixing velocity due to void drift. Based on a systematic simulation covering PWR working conditions, correlations were proposed to calculate β_{VD} in terms of void fraction, subchannel geometry and a Reynolds number.

The proposed void drift model, i.e. correlation for the void fraction distribution at equilibrium state and for the void drift coefficient β_{VD} , was implemented in MATRA along with the EMVD interchannel mixing model. Validation of the proposed void drift model was performed by recalculating selected test cases of the ISPRA rod bundle benchmark [31] in the bubbly flow regime under PWR pressure level. Compared to the EVVD model, the EMVD model with the proposed void drift model provides a similar prediction accuracy of the subchannel flow parameters. However, with the EMVD model a better physical interpretation of the individual mixing effects was established, for turbulent mixing and void drift are separated. With two-phase CFD models maturing in the future, especially the modeling approaches regarding lift force, further improvement of the void drift model proposed in the current study is to be expected.

Last but not least, selected empirical CHF correlations were assessed with the proposed void drift model. It revealed that the EPRI-1 correlation [62] shows overall the best prediction accuracy and is hence recommended to application in bubbly flow regime under PWR pressure level.

Zusammenfassung

Die Vorhersage der kritischen Heizflächenbelastung (KHB) in einer Stabbündel-Geometrie erfordert Informationen über Strömungszustände in Unterkanälen, die stark vom Queraustausch abhängig sind. Unter zweiphasigen Bedingungen kann der Queraustausch zwischen zwei benachbarten Unterkanälen in drei elementare Komponenten zerlegt werden [47, 72]: turbulente Mischung (TM), Diversion Crossflow (DC) und Void Drift (VD). Turbulente Mischung entsteht aus den stochastischen Strömungsfuktuationen und Diversion Crossflow ist verursacht durch den radialen Druckunterschied zwischen benachbarten Unterkanälen. Aber der physikalische Mechanismus von Void Drift ist noch nicht gut verstanden. Die vorliegende Arbeit beschäftigt sich mit der Simulation und Analyse von Void Drift in einer Stabbündel-Geometrie mit dem Unterkanal-Programm MATRA [107] (modifiziert basierend auf COBRA-IV-I [86]) und dem CFD Programm ANSYS CFX [2].

In der Unterkanalanalyse wird Diversion Crossflow mit einer Impulserhaltungsgleichung direkt berechnet. Modelle zur Beschreibung der Austauscheffekte von turbulenter Mischung und Void Drift sind benötigt. Derzeit in MATRA verfügbare Void Drift Modelle basieren auf dem Konzept, nach dem durch turbulente Mischung und Void Drift Fluidklumpen gleiches Volumens ausgetauscht werden sollen (EVVD Modell [47]). Es setzt voraus, dass ein Zwei-Phasen-System sich dem sogenannten voll entwickelten Gleichgewichtszustand annähert. Ist dieser Zustand erreicht, verschwindet Netto-Austauscheffekt wegen Queraustausch. Ein auffälliger Nachteil des EVVD Modells ist die kombinierte Modellierung der ungerichteten turbulenten Mischung (TM) und des gerichteten Void Drift (VD) mit der gleichen effektiven Mischgeschwindigkeit. Die beiden Effekte sind im EVVD Modell nicht eindeutig voneinander getrennt. Trotzdem ist EVVD Modell in modernen Unterkanal-Programmen weitgehend implementiert und lässt sich leicht anwenden, unter der Voraussetzung, dass die Verteilung des volumetrischen Dampfgehaltes im Gleichgewichtszustand bekannt ist. Ein modifiziertes Modell von Levy [51] mit Einführung des Void Drift Korrekturfaktors K_{VD} durch Hwang et al. [33] wurde in MATRA implementiert, um den volumetrischen Dampfgehalt im Gleichgewichtszustand zu bestimmen. Allerdings berücksichtigt dieses Modell nur den Einfluss der Massenstromdichte auf den Dampfgehalt im Gleichgewichtszustand. Zwei Typen des EVVD Modells mit unterschiedlichen Ansätzen für K_{VD} sind in MATRA vorhanden. Beide Typen implizieren, dass die Gasphase sich im Gleichgewichtszustand in den Unterkanälen mit größerer Massestromdichte ansammelt. Aber die Trennung der turbulenten Mischung mit Void Drift ist bisher in MATRA noch nicht durchgeführt. Für die Bewertung des EVVD Modells wurden Nachberechnungen ausgewählter Stabbündel-Benchmark-Testfälle unter sowohl SWR als auch DWR-Bedingungen durchgeführt. Es zeigt, dass das EVVD Modell in MATRA für die Anwendung auf Blasenströmung unter DWR-Druckniveau eine Verbesserung benötigt. Die Tendenz des höheren volumetrischen Dampfgehaltes im Unterkanal mit größerer Massenstromdichte ist nicht gültig in Blasenströmung unter DWR-Druckniveau.

Die Verbesserung des EVVD Modells soll in zwei Aspekten durchgeführt werden. Erstens sollen die turbulente Mischung und Void Drift mit individueller effektiver Mischgeschwindigkeit berücksichtigt werden. Zweitens soll das Modell zur Berechnung des volumetrischen Dampfge-

halten im Gleichgewichtszustand erweitert werden, so dass der Einfluss des geometrischen Unterschiedes zwischen zwei benachbarten Unterkanälen ebenfalls berücksichtigt wird. In der aktuellen Studie wurde eine phänomenologische Beschreibung des zweiphasigen Queraustausches vorgeschlagen. Dabei wird angenommen dass durch turbulente Mischung Fluidenelemente gleicher Masse (auf Englisch equal-mass) ausgetauscht werden sollen. Dieses neue Modell wird auch als EMVD-Modell bezeichnet. Im EMVD Modell sind die drei elementaren Austauschereffekte, nämlich turbulente Mischung, Diversion Crossflow und Void Drift, klar voneinander getrennt. Für die Modellierung des Void Drift sind die Kenntnisse des volumetrischen Dampfgehaltes im Gleichgewichtszustand und der effektiven Mischgeschwindigkeit aufgrund Void Drift erforderlich.

Um die oben genannten zwei Schlüsselparameter des Void Drift zu bestimmen, wurde der zweiphasige Queraustausch in einer Stabbündel-Geometrie mit CFD Programm simuliert. Das Euler Zwei-Fluid-Modell wurde eingesetzt, um die Blasenströmung zu beschreiben. Die flüssige Phase wurde als kontinuierliche Phase angesehen, während die Gasphase als disperse Phase betrachtet wurde. Die Validierung des verwendeten CFD-Modells wurde durch Nachberechnung des zweiphasigen Queraustausches gemessen von van der Ros [101] und Gonzalez-Santalo et al. [29] durchgeführt. Es zeigt, dass die Modellierung der Auftriebskraft (auf Englisch: lift force) starke Auswirkungen auf den vorhergesagten Queraustausch hat. Leider sind bisher keine generell anwendbaren Modelle zur Beschreibung der Auftriebskraft verfügbar. In der vorliegenden Arbeit wurde ein konstanter Auftriebskoeffizient von 0,05 basierend auf einer detaillierten Sensitivitätsstudie empfohlen.

Mit dem validierten CFD-Modell wurden Simulationen des Queraustausches in Blasenströmung unter DWR-Druckniveau (157 bar) durchgeführt und analysiert. Im ersten Satz von Simulationen wurde der Gleichgewichtszustand mit Hilfe zyklischer Randbedingungen simuliert. Bezüglich des volumetrischen Dampfgehaltes im Gleichgewichtszustand wurden sowohl der Einfluss der Massenstromdichte als auch der Einfluss der Geometrie berücksichtigt. Ein neues, erweitertes Levy-Modell wurde vorgeschlagen, um den volumetrischen Dampfgehalt im Gleichgewichtszustand zu berechnen. Der zweite Satz von Simulationen beschäftigte sich mit der Bestimmung der wirksamen Mischgeschwindigkeit aufgrund Void Drift, die durch Dividieren durch die durchschnittliche Geschwindigkeit in der Hauptströmungsrichtung den sogenannten dimensionslosen Void Drift Koeffizient β_{VD} ergibt. Basierend auf einer systematischen CFD Simulation, die DWR Betriebsbedingungen abdeckt, wurden Korrelationen zur Berechnung von β_{VD} in Bezug auf den volumetrischen Dampfgehalt, die Reynolds-Zahl und die Unterkanal-Geometrie vorgeschlagen.

Das oben vorgeschlagene Void Drift Modell, d.h. die Korrelation für volumetrischen Dampfgehalt im Gleichgewichtszustand und die Korrelation für den Void Drift Koeffizient β_{VD} , wurde zusammen mit dem EMVD Modell in MATRA implementiert. Die Validierung des EMVD Modells wurde durch die Nachberechnungen ausgewählter Testfälle unter Blasenströmung Bedingung und DWR-Druckniveau im Rahmen des ISPRA Stabbündel-Benchmarks [31] durchgeführt. Im Vergleich zum EVVD Modell weist das EMVD Modell mit dem Void Drift Modell aus der vorliegenden Studie eine ähnliche Vorhersagegenauigkeit auf, aber mit einer viel besseren physikalischen Interpretation der einzelnen Austauschereffekte. Turbulente Mischung und Void Drift sind im EMVD Modell eindeutig voneinander getrennt. Mit Weiterentwicklung des Zwei-Fluid-Modells in der Zukunft, vor allem der Modelle zur Beschreibung der Auftriebskraft, ist eine weitere Verbesserung des in der aktuellen Studie vorgeschlagenen Void Drift Modells zu erwarten.

Zum Schluss wurde das EMVD Modell angewendet, um ausgewählte empirische KHB Korrelationen zu bewerten. Die EPRI-1 Korrelation [62] zeigt insgesamt die beste Vorhersagegenauigkeit und wird daher für die Anwendung in Blasenströmung unter DWR-Druckniveau empfohlen.

Contents

Acknowledgements	i
Abstract	iii
Zusammenfassung	v
List of Figures	ix
List of Tables	xiii
Nomenclature	xv
1 Introduction	1
1.1 Motivation	1
1.2 Objectives of this study	3
2 State of the art	5
2.1 Experimental studies on two-phase interchannel mixing phenomena	6
2.1.1 Experimental studies: a brief summary	6
2.1.2 Conclusion and discussion	15
2.2 Modeling approach of two-phase interchannel mixing in subchannel analysis	18
2.2.1 Equal-volume-exchange turbulent mixing incorporating void drift	18
2.2.2 Equal-mass-exchange turbulent mixing incorporating void drift	19
2.2.3 Conclusion and discussion	20
3 Assessment of two-phase interchannel mixing models in MATRA	21
3.1 The MATRA code	21
3.1.1 Subchannel conservation equations	21
3.1.2 Numerical solution scheme	24

CONTENTS

3.1.3	Constitutive relations in MATRA	27
3.2	Interchannel mixing models in MATRA	31
3.2.1	EM model	31
3.2.2	EVVD model	33
3.3	Assessment of the interchannel mixing models in MATRA	34
3.3.1	NUPEC BFBT benchmark	34
3.3.2	ISPRA EUROP benchmark	40
3.4	Conclusion and discussion	43
4	Validation of two-phase CFD model for predicting two-phase interchannel mixing	45
4.1	Eulerian two-fluid model in Ansys CFX	45
4.1.1	Governing equations	45
4.1.2	Interphase momentum transfer	46
4.1.3	Turbulence modeling	47
4.1.4	Solution strategy - the coupled solver	52
4.2	Validation of two-phase CFD model	52
4.2.1	Overview of the employed two-phase CFD model	53
4.2.2	Validation calculation with van der Ros two-channel system	53
4.2.3	Validation calculation with Gonzalez-Santalo two-channel system	58
4.2.4	Conclusion and discussion	66
5	Simulation and analysis of two-phase interchannel mixing with CFD approach	67
5.1	Phenomenological description of two-phase interchannel mixing	67
5.2	Description of the modified void drift model	69
5.3	Simulation and analysis of void drift with two-phase CFD approach	70
5.3.1	Void fraction distribution at equilibrium state	72
5.3.2	Void drift coefficient	78
5.4	Discussion about void drift and lift force	87
6	Validation and application of the proposed void drift model	93
6.1	Validation of the proposed void drift model	93
6.2	Assessment of selected empirical critical heat flux (CHF) correlations	96
7	Conclusion and outlook	101
	Bibliography	103

List of Figures

2.1	Subchannel cross section with dimension in <i>mm</i> (Rowe and Angle [69]).	7
2.2	Radial flow quality profile of air-water two-phase flow in a nine-rod bundle (Schraub et al. [79]).	7
2.3	Comparison of the subchannel average exit conditions (Lahey et al. [48]).	8
2.4	The 4×4 square rod bundle conducted in Columbia University (Castellana and Casterline [14]), dimension in <i>mm</i> ; the Arabic numbers denote subchannels. <i>H</i> and <i>C</i> denote the hotter rods with relative higher heat flux and the colder rods with relative lower heat flux, respectively.	10
2.5	Test section and radial void profile (Tsuge et al. [100]).	11
2.6	Schematic diagram of test sections (Tapucu et al. [91, 92]).	12
2.7	Schematic diagram of Sekoguchi et al. test section [80], dimension in <i>mm</i>	13
2.8	Test sections of experimental investigations on two-phase interchannel mixing phenomena conducted in Kumamoto University, Japan.	13
3.1	An arbitrary subchannel control volume (taken from [86]).	22
3.2	Flow chart diagram of the implicit solution scheme in MATRA.	26
3.3	Test assemblies and power distribution profiles of void distribution tests in the BFBT benchmark [59].	35
3.4	Bundle average exit void fractions calculated with (a) the modified Armand model and (b) the Chexal-Lellouche model.	37
3.5	Subchannel average exit void fractions at different bundle average exit qualities with: (a) the equal-mass-exchange turbulent mixing (EM) model and (b) the equal-volume-exchange turbulent mixing with void drift (EVVD) model (Type II).	38
3.6	Cross-sectional view of the EUROP test section with shaded areas denoting the sampled five subchannels for flow and enthalpy measurement [31].	40
3.7	Calculation of subchannel exit quality of ISPRA EUROP test cases with (a) the EVVD model type I ($K_{VD} = 1.4$) and (b) the EVVD model type II (K_{VD} recalculated with Eq. 3.57 and 3.58).	41
3.8	Calculation of subchannel relative enthalpy increase of ISPRA EUROP test cases with (a) the EVVD model type I ($K_{VD} = 1.4$) and (b) the EVVD model type II (K_{VD} recalculated with Eq. 3.57 and 3.58).	42
3.9	Recalculation of ISPRA EUROP test cases with $K_{VD} = -4.0$	42

LIST OF FIGURES

4.1	Test section investigated by van der Ros [101] (dimension in <i>mm</i>). <i>Z</i> direction is the main streamwise direction.	54
4.2	Block topology and mesh structure approximating the test section investigated by van der Ros [101].	55
4.3	Results of the mesh sensitivity study with the test cases summarized in Tab. 4.1; <i>Z</i> direction is the main streamwise direction.	56
4.4	Results of the drag force study with test cases summarized in Tab. 4.1; <i>Z</i> direction is the main streamwise direction.	57
4.5	Results of the lift force coefficient (C_L) sensitivity study with test cases in Tab. 4.1; <i>Z</i> direction is the main streamwise direction.	59
4.6	Schematic illustration of the test loop used by Gonzalez-Santalo and Griffith [29].	60
4.7	Test section 1 and 3 used by Gonzalez-Santalo and Griffith [29] with dimension in <i>mm</i> ; <i>Z</i> direction is the main streamwise direction.	60
4.8	Block topology and mesh structure describing the test section 3 used by Gonzalez-Santalo and Griffith [29]; <i>Z</i> direction is the main streamwise direction.	62
4.9	Mesh sensitivity study with RUN 39 in Tab. 4.2; <i>Z</i> direction is the main streamwise direction.	62
4.10	Drag force study with RUN 39 in Tab. 4.2; <i>Z</i> direction is the main streamwise direction.	63
4.11	Sensitivity study of the lift force coefficient C_L with test cases in Tab. 4.2; <i>Z</i> direction is the main streamwise direction.	64
4.12	Sensitivity study of the lift force coefficient C_L with bubble diameter of 1 <i>mm</i> for RUN 39 in Tab. 4.2.	65
4.13	Sensitivity study of bubble diameter with RUN 39 in Tab. 4.2.	65
5.1	Axial and lateral interchannel mass flows between two interacting subchannels 1 and 2; <i>Z</i> direction is the main streamwise direction.	68
5.2	Schematic description of void drift process.	70
5.3	Cross-sectional view of the two investigated subchannel combinations: (a) center-center subchannel combination and (b) wall-center subchannel combination.	71
5.4	Boundary conditions for determination of the mass flux effect on void fraction distribution at equilibrium state.	72
5.5	Block topology and mesh structure of the investigated two-channel system consisting of two interacting center subchannels; <i>Z</i> direction is the main streamwise direction.	73
5.6	Dependence of void fraction distribution at equilibrium state on mass flux distribution in two interacting subchannels.	73
5.7	Factor K_1 correlated with the average void fraction of two interacting subchannels.	74
5.8	Boundary conditions for determination of the geometrical effect on void fraction distribution at equilibrium state.	74

LIST OF FIGURES

5.9	Interpolation to equalize the mass flux in a wall subchannel (denoted with the subscript 1) and a center subchannel (denoted with the subscript 2).	75
5.10	Block topology and mesh structure of the investigated two-channel system consisting of a wall subchannel interacting with a center subchannel; Z direction is the main streamwise direction.	76
5.11	Dependence of the factors K_2 and K_3 on the average mass flux in two interacting subchannels.	76
5.12	Geometrical effect on void fraction distribution at equilibrium state for a wall-center subchannel combination with various hydraulic diameter differences.	77
5.13	Factor K_2 and K_3 correlated with the average void fraction of two interacting subchannels.	77
5.14	Superposition of the mass flux effect and the geometrical effect on void fraction distribution at equilibrium state.	78
5.15	Boundary conditions for determination of void drift coefficient in the center-center subchannel combination.	79
5.16	Results of the mesh sensitivity study for determination of void drift coefficient in the center-center subchannel combination.	80
5.17	Summary of the void drift coefficient β_{VD} with feeding factors of 2 and 3.	81
5.18	Dependence of the factors C_1 and C_2 on the average liquid Reynolds number $Re_{l,avg}$ of two interacting center subchannels.	82
5.19	Assessment of the proposed correlation of void drift coefficient in the center-center subchannel combination (feeding factor F_g equals 2 and 3).	83
5.20	Assessment of the proposed correlation of void drift coefficient in the center-center subchannel combination (feeding factor F_g equals 4).	83
5.21	Boundary conditions for determination of void drift coefficient in the wall-center subchannel combination.	84
5.22	Dependence of the void drift coefficient β_{VD} on the average void fraction with varying W/S from 0.6, 0.8, 1.1 to 1.3.	84
5.23	Dependence of the factors C_3 and C_4 on $Re_{l,avg}$ with varying W/S from 0.6, 0.8 to 1.1 (the corresponding $\Delta D_{h,rel}$ varying from 51.0, 36.7 to 18.4%).	85
5.24	Dependence of the factors C_3 on the absolute relative hydraulic diameter difference $\Delta D_{h,rel}$ defined in Eq. 5.34.	86
5.25	Assessment of the proposed void drift coefficient correlation in the wall-center subchannel combination with varying W/S from 0.6, 0.8, 1.1 to 1.3.	87
5.26	Void fraction and liquid velocity on a cross-sectional plane at Z elevation of 0.9 m	88
5.27	Diversion cross flow mechanism interpreted with the static pressure difference in two interacting subchannels.	89
5.28	Gaseous phase velocity and lift force acting on dispersed bubbles.	89
5.29	Study of the relation between void drift and lift force with two interacting center subchannels; Z direction is the main streamwise direction.	90

LIST OF FIGURES

5.30	Diversion cross flow due to lateral pressure difference between two interacting subchannels.	91
5.31	Lift force in the X direction on the defined line for test cases in Tab. 5.4.	91
5.32	The relation between void drift and lift force acting on dispersed bubbles.	92
6.1	Validation of the EMVD model with prediction to measurement ratio of subchannel enthalpy increase and exit mass flux of the wall subchannel.	94
6.2	Validation of the EMVD model with prediction to measurement ratio of subchannel enthalpy increase and exit mass flux of the corner subchannel.	95
6.3	Validation of the EMVD model with prediction to measurement ratio of subchannel enthalpy increase and exit mass flux of the center subchannel.	95
6.4	Assessment of the selected empirical CHF correlations.	100

List of Tables

3.1	Experimental conditions of BFBT test cases recalculated with MATRA	36
3.2	MATRA models used for recalculation of BFBT test cases: assessment of the quality-void relations	37
3.3	Statistical evaluation of subchannel analysis results of test cases with bundle average exit quality 2%, Assembly type 0	39
3.4	Statistical evaluation of subchannel analysis results of test cases with bundle average exit quality 2%, Assembly type 1 and 4	39
3.5	MATRA models used for recalculation of selected ISPRA EUROP test cases: assessment of interchannel mixing models	41
4.1	Inlet conditions of the selected test cases conducted by van der Ros [101] with test section depicted in Fig. 4.1 for validation calculation	55
4.2	Inlet conditions of selected test cases of [29] for validation calculation	61
5.1	Physical properties of the investigated water-steam two-phase system under 157 bar and 345.82 °C	71
5.2	Summary of inlet void fractions with center-center subchannel combination (see Fig. 5.15)	80
5.3	Proposed correlations of void drift coefficient β_{VD} based on CFD simulations conducted in the current study	86
5.4	Summary of boundary conditions for study of the relation between void drift and lift force	90
6.1	Summary of the interchannel mixing terms of mass, momentum and energy between two interacting subchannels i and j	93
6.2	Validity range of selected empirical critical heat flux (CHF) correlations	97
6.3	Summary of flow parameters of selected test cases from [66]	99
6.4	MATRA models for recalculation of the high pressure rod bundle DNB benchmark [66]	99

Nomenclature

Latin letters

A	Axial (main streamwise) cross-sectional area	$[m^2]$
a_1, a_2	Dimensionless constant used in MATRA to evaluating void drift correction factor K_{VD}	$[-]$
A_{gl}	Interphase surface between dispersed gaseous phase and continuous liquid phase	$[m^2]$
A_g	Cross-sectional area occupied by gaseous phase	$[m^2]$
A_l	Cross-sectional area occupied by liquid phase	$[m^2]$
B	Dimensionless constant used in logarithmic velocity profile	$[-]$
C_1, C_2, C_3, C_4	Dimensionless constants used to correlate void drift coefficient β_{VD}	$[-]$
C_D	Dimensionless drag force coefficient	$[-]$
C_L	Dimensionless lift force coefficient	$[-]$
c_p	Specific heat capacity	$[kJkg^{-1}K^{-1}]$
C_W	Dimensionless wall lubrication force coefficient	$[-]$
$C_{\epsilon 1}$	Dimensionless k - ϵ turbulence model constant	$[-]$
$C_{\epsilon 2}$	Dimensionless k - ϵ turbulence model constant	$[-]$
$C_{\mu b}$	Dimensionless constant used in Sato's model of bubble induced continuous phase viscosity	$[-]$
C_{μ}	Dimensionless k - ϵ turbulence model constant	$[-]$
C_{TD}	Dimensionless turbulent dispersion force coefficient	$[-]$
C_{VM}	Dimensionless virtual mass force coefficient	$[-]$
$\Delta D_{h,rel}$	Relative absolute hydraulic diameter difference between two subchannels	$[-]$
\tilde{D}_{VD}	Void diffusion coefficient due to void drift	$[m^2s^{-1}]$
D	Rod outer diameter	$[m]$

Nomenclature

D_g, D_B	Dispersed gaseous phase bubble diameter	[m]
D_h	Hydraulic diameter defined with cross-sectional area and wetted perimeter	[m]
E_{rel}	Averaged absolute relative deviation between β_{VD}^{Corr} and β_{VD}^{CFD}	[-]
F_D	Volumetric drag force	[kgm ⁻² s ⁻²]
F_L	Volumetric lift force	[kgm ⁻² s ⁻²]
F_{TD}	Volumetric turbulent dispersion force	[kgm ⁻² s ⁻²]
F_{VM}	Volumetric virtual mass force	[kgm ⁻² s ⁻²]
F_{WL}	Volumetric wall lubrication force	[kgm ⁻² s ⁻²]
f	Dimensionless friction factor	[-]
F_g	Gaseous phase feeding factor, defined in Eq. 5.28	[-]
f_T	Dimensionless factor used in COBRA-IV-I to correct the imperfect analogy between eddy diffusivity of heat and momentum transfer	[-]
F_X	Force per axial (main streamwise) length acting on subchannel	[Nm ⁻¹]
f_μ	Dimensionless constant used in zero-equation turbulence model	[-]
F_{ij}	Combined drag force due to frictional and local form pressure drop between subchannel i and j over the connecting gap	[Nm ⁻¹]
\mathbf{g}	Gravity acceleration in vector notation	[ms ⁻²]
G	Mass flux in axial (main streamwise) direction	[kgm ⁻² s ⁻¹]
g	Gravity acceleration	[ms ⁻²]
G_{avg}	Average mass flux in axial (main streamwise) direction of two interacting subchannels	[kgm ⁻² s ⁻¹]
\hat{h}	Flowing enthalpy	[kJkg ⁻¹]
h	Static enthalpy	[kJkg ⁻¹]
h^*	Enthalpy transported by diversion cross flow	[kJkg ⁻¹]
h'	Enthalpy transported by turbulent mixing and void drift	[kJkg ⁻¹]
h_m	Enthalpy of two-phase mixture	[kJkg ⁻¹]
h_b	Bundle average enthalpy	[kJkg ⁻¹]
h_{inr}	Relative subchannel enthalpy increase	[-]
h_{lg}	Latent heat	[kJkg ⁻¹]
h_{ls}	Saturation enthalpy of the single liquid phase	[kJkg ⁻¹]

Nomenclature

H_{surf}	Surface heat transfer coefficient	$[Wm^{-2}K^{-1}]$
J	Index denoting the current calculation level in the implicit solution scheme of MATRA	
j	Superficial velocity	$[ms^{-1}]$
K	Dimensionless local pressure drop factor	$[-]$
k	Turbulence kinetic energy	$[m^2s^{-2}]$
K_1, K_2, K_3	Dimensionless factors used to determine void fraction distribution at equilibrium state	$[-]$
K_G	Dimensionless lateral pressure drop factor for rod bundle	$[-]$
K_{ij}	Dimensionless lateral pressure drop factor for two interacting subchannels i and j	$[-]$
K_{VD}	Void drift correction factor	$[-]$
L_c	Centroid-to-centroid distance of two interacting subchannels	$[m]$
L_t	Turbulence length scale	$[m]$
l_{mix}	Mixing length	$[m]$
\overline{M}_ϕ	Interphase momentum transfer exerted on phase ϕ	$[kgm^{-2}s^{-2}]$
m	Mass flow rate in axial (main streamwise) direction	$[kgs^{-1}]$
\mathbf{nw}	Unit normal vector pointing away from the wall	$[-]$
N	Index denoting the outer loop of the implicit solution scheme of MATRA	
n	Number of bubbles in a finite control volume V	$[-]$
N_C	Total number of subchannels	$[-]$
P	Pitch distance between two adjacent rods in a rod bundle	$[m]$
p	Static pressure	$[bar]$
P/D	Pitch to diameter ratio	$[-]$
P/M	Prediction to measurement ratio	$[-]$
P_k	Production rate of turbulence kinetic energy by the mean flow	$[kgm^{-1}s^{-3}]$
p_r	Reduced pressure, defined as system pressure divided by the critical pressure	$[-]$
Δp_f	Frictional pressure drop	$[Pa]$
Δp_K	Local pressure drop	$[Pa]$
Δp_{ij}	Lateral pressure difference between two interacting subchannels i and j	$[Pa]$

Nomenclature

Q	Volumetric flow rate	$[m^3 s^{-1}]$
q''_n	Heat flux input into subchannel from the heated rod indexed with n	$[kJm^{-2} s^{-1}]$
q'	Heat input per axial (main streamwise) length into subchannel	$[kJm^{-1} s^{-1}]$
q_{CHF}	Critical heat flux	$[kJm^{-2} s^{-1}]$
q_{CHF}^{calc}	Critical heat flux calculated with empirical correlations	$[kJm^{-2} s^{-1}]$
q_{CHF}^{exp}	Critical heat flux determined from experimental measurements	$[kJm^{-2} s^{-1}]$
q_{mr}	Relative subchannel exit mass flux	$[-]$
$\bar{\mathbf{R}}_\phi$	Viscous stress tensor of the mean flow velocity of phase ϕ	$[kgm^{-1} s^{-2}]$
$\bar{\mathbf{R}}_\phi^{eff}$	Effective shear stress tensor, i.e. sum of viscous and Reynolds stress tensor, of phase ϕ	$[kgm^{-1} s^{-2}]$
\mathbf{R}'_ϕ	Reynolds stress tensor of phase ϕ	$[kgm^{-1} s^{-2}]$
s	Slip ratio	$[-]$
S, S_{ij}	Gap clearance, gap clearance between subchannel i and j	$[m]$
T	Temperature	$[^\circ C]$
t	Time	$[s]$
T_F	Temperature of fluid in subchannel	$[^\circ C]$
T_W	Temperature of heat conducting wall in subchannel analysis	$[^\circ C]$
T_{rod}	Temperature distribution in fuel rod	$[^\circ C]$
T_{sub}	Subcooled temperature	$[K]$
ΔT_d	Saturation temperature minus bulk fluid temperature at the point of bubble departure from the heated wall	$[^\circ C]$
$\bar{\mathbf{U}}_r$	Relative mean flow velocity in vector notation	$[ms^{-1}]$
$\bar{\mathbf{U}}$	Reynolds averaged mean flow velocity in vector notation	$[ms^{-1}]$
\mathbf{U}	Velocity vector with components u, v and w in X, Y and Z direction, respectively	$[ms^{-1}]$
\bar{U}_t	Mean flow velocity parallel to the wall	$[ms^{-1}]$
u, v, w	Velocity components in X, Y and Z direction, respectively	$[ms^{-1}]$
u^+	Dimensionless flow velocity parallel to the wall	$[-]$

Nomenclature

u^*	Axial velocity transported by diversion cross flow	$[ms^{-1}]$
u'	Axial velocity transported by turbulent mixing and void drift	$[ms^{-1}]$
u_τ	Wall shear velocity	$[ms^{-1}]$
u_g	Gaseous phase velocity in X direction	$[ms^{-1}]$
u_l	Liquid phase velocity in X direction	$[ms^{-1}]$
u_t	Flow velocity parallel to the wall	$[ms^{-1}]$
u_{DC}	Effective mixing velocity of diversion cross flow	$[ms^{-1}]$
V	Volume	$[m^3]$
W	Wall distance, distance between rod and wall	$[m]$
W/S	Wall distance to gap clearance ratio	$[-]$
w'_{ij}	Lateral interchannel mixing flow rate per axial length due to turbulent mixing and void drift from subchannel i to j	$[kgm^{-1}s^{-1}]$
w'_{itoj}	Net lateral interchannel mixing flow rate per axial length due to turbulent mixing and void drift from subchannel i to j , equals $w'_{ij} - w'_{ji}$	$[kgm^{-1}s^{-1}]$
w'_{ji}	Lateral interchannel mixing flow rate per axial length due to turbulent mixing and void drift from subchannel j to i	$[kgm^{-1}s^{-1}]$
w_{1to2}^{DC}	Net lateral interchannel mixing flow rate per axial length due to diversion cross flow from subchannel i to j , see chapter 5.1	$[kgm^{-1}s^{-1}]$
w_{1to2}^{TM}	Net lateral interchannel mixing flow rate per axial length due to turbulent mixing from subchannel i to j , see chapter 5.1	$[kgm^{-1}s^{-1}]$
w_{1to2}^{VD}	Net lateral interchannel mixing flow rate per axial length due to void drift from subchannel i to j , see chapter 5.1	$[kgm^{-1}s^{-1}]$
w_g	Gaseous phase velocity in Z direction	$[ms^{-1}]$
w_l	Liquid phase velocity in Z direction	$[ms^{-1}]$
w_r	relative velocity in Z direction, equal to $(w_g - w_l)$	$[ms^{-1}]$
w_{ij}	Lateral interchannel mixing flow rate per axial length due to diversion cross flow from subchannel i to j	$[kgm^{-1}s^{-1}]$
x	Flow quality	$[-]$
X, Y, Z	Cartesian coordinates	
x_C	Transition quality from slug to annular flow regime used in MATRA	$[-]$

Nomenclature

x_t	True quality, used in COBRA-IV-I and MATRA	[–]
x_{avg}	Average flow quality of two interacting sub-channels	[–]
x_{eq}	Equilibrium quality	[–]
x_{OSV}	Equilibrium quality at onset of significant void, i.e. at the point of bubble departure from the heated wall	[–]
\tilde{y}^+	Recalculated dimensionless wall distance used in the scalable wall function in Ansys CFX	[–]
y^+	Dimensionless wall distance	[–]

Greek letters

α	Space and time averaged volumetric void fraction	[–]
α_p, α_m	Predicted and measured void fraction, respectively	[–]
β	Turbulent mixing coefficient	[–]
β_{SP}	Turbulent mixing coefficient for single phase flow	[–]
β_{VD}	Dimensionless void drift coefficient	[–]
β_{VD}^{CFD}	Dimensionless void drift coefficient obtained from CFD simulation results	[–]
β_{VD}^{Corr}	Dimensionless void drift coefficient obtained with proposed correlation	[–]
δ_{ij}	Kronecker symbol ($\delta_{ij} = 1$ if $i = j$ and $\delta_{ij} = 0$ otherwise)	[–]
ϵ	Dissipation rate of the turbulence kinetic energy	$[m^2 s^{-3}]$
Γ_t	Eddy diffusivity	$[m^2 s^{-1}]$
$\hat{\rho}$	Two-phase mixture momentum density	$[kg m^{-3}]$
κ	Von Karman constant	[–]
λ	Thermal conductivity	$[W m^{-1} K^{-1}]$
λ_l	Thermal conductivity of single liquid phase	$[W m^{-1} K^{-1}]$
μ	Molecular dynamic viscosity	$[kg m^{-1} s^{-1}]$
μ_b	Bubble induced continuous phase dynamic viscosity	$[kg m^{-1} s^{-1}]$

Nomenclature

μ_t	Turbulent dynamic viscosity	$[kgm^{-1}s^{-1}]$
μ_{eff}	Effective dynamic viscosity	$[kgm^{-1}s^{-1}]$
ν_t	Turbulent kinematic viscosity	$[m^2s^{-1}]$
Φ^2	Dimensionless two-phase frictional pressure drop multiplier	$[-]$
π	Mathematical constant defined as ratio of a circle's circumference to diameter	$[-]$
ρ	Density	$[kgm^{-3}]$
ρ^*	Density of fluid transported by diversion cross flow, normally taken as density of the donor subchannel ρ_{donor}	$[kgm^{-3}]$
ρ_{donor}	Fluid density of the donor subchannel	$[kgm^{-3}]$
σ	Turbulent viscosity Prandtl number used in dispersed phase zero-equation turbulence model	$[-]$
σ_ϵ	Dimensionless k - ϵ turbulence model constant	$[-]$
σ_k	Dimensionless k - ϵ turbulence model constant	$[-]$
$\sigma_{t,l}$	Turbulent Schmidt number of the continuous liquid phase volume fraction	$[-]$
τ_W	Wall shear stress	$[Pa]$
θ	A flow regime dependent two-phase turbulent mixing multiplication factor	$[-]$
θ_M	Dimensionless constant used for evaluating θ	$[-]$
ξ_n	Heated perimeter of rod indexed with n that facing the subject subchannel	$[m]$

Superscripts

DC	Flow parameters related to diversion cross flow
ex	Exit flow parameters
in	Inlet flow parameters
TM	Flow parameters related to turbulent mixing
VD	Flow parameters related to void drift

Subscripts

ϕ	Index for phase, ϕ equals g or l
--------	---

<i>avg</i>	Average flow parameters of the two interacting subchannels combined
<i>b</i>	Bundle average flow parameters
<i>calc</i>	Calculated results from simulation
<i>center</i>	Center subchannel
<i>corner</i>	Corner subchannel
<i>EQ</i>	Equilibrium state
<i>exp</i>	Experimental results
<i>g</i>	Gaseous phase
<i>i, j</i>	Subchannel index
<i>itoj, 1 to 2</i>	Net interchannel exchange from subchannel <i>i</i> to <i>j</i> and from subchannel 1 to 2, respectively
<i>J</i>	Flow parameters in the current calculation level in the implicit solution scheme of MATRA
<i>l</i>	Liquid phase
<i>m</i>	Two-phase mixture
<i>SC</i>	Subchannel average flow parameters
<i>SP, TP</i>	Single- and two-phase, respectively
<i>wall</i>	Wall subchannel

Abbreviations

<i>BWR</i>	Boiling water reactor
<i>CFD</i>	Computational fluid dynamics
<i>CHF</i>	Critical heat flux
<i>COBRA</i>	Coolant Boiling in Rod Arrays
<i>DC</i>	Diversion cross flow
<i>EM</i>	Equal-mass-exchange turbulent mixing model
<i>EMVD</i>	Equal-mass-exchange turbulent mixing with void drift model
<i>EV</i>	Equal-volume-exchange turbulent mixing model
<i>EVVD</i>	Equal-volume-exchange turbulent mixing with void drift model
<i>HVC</i>	High void subchannel
<i>LVC</i>	Low void subchannel

Nomenclature

<i>LWR</i>	Light water reactor	
<i>MATRA</i>	Multichannel Analyzer for steady states and Transients in Rod Arrays	
<i>Nu</i>	Nusselt number	[-]
<i>Pr</i>	Prandtl number	[-]
<i>PWR</i>	Pressurized water reactor	
<i>Re</i>	Reynolds number	[-]
<i>Re_B</i>	Bubble Reynolds number	[-]
<i>Re_l</i>	Liquid Reynolds number	[-]
<i>RMSD</i>	Root mean square deviation	
<i>TM</i>	Turbulent mixing	
<i>VD</i>	Void drift	

1. Introduction

1.1 Motivation

Heat removal rate from a water cooled nuclear reactor, such as boiling water reactor (BWR) or pressurized water reactor (PWR), is mainly limited by critical heat flux (CHF). According to Tong and Hewitt [98], CHF is defined as the maximum heat flux occurring just before a change of boiling heat transfer mode (boiling crisis), indicated by an abrupt rise of fuel rod surface temperature that may endanger fuel rod integrity. CHF is one of the most important design parameters of water cooled nuclear reactors. An accurate prediction of CHF contributes to safety margin but also to economic profitability of a nuclear power plant. A widely used approach is empirical correlation based on experimental study over a large range of operation parameters. The experimentally obtained CHF results have usually been related with average flow parameters, even for complex rod bundle geometries. Application of such correlations is confined to the geometries and parameters, for which they were established. An extrapolation beyond the experimental conditions is not reliable. Another approach is to characterize the experimental CHF results with local flow parameters, at which boiling crisis was measured. The resulting correlations may then be extrapolated to other rod bundles with different geometries.

For simple channels, i.e. round tube, annuli, etc., flow conditions at a given axial (stream-wise) position can be readily determined by a heat balance. Although the flow parameters obtained in this manner are the average values over the cross section, they are unique for the considered location and hence can be used to correlate CHF data. In contrast, local flow conditions of a complex nuclear fuel assembly, represented by a rod bundle in square or triangular arrangement, can not be easily determined. For a given set of bundle average operating conditions (i.e. bundle average heat flux, mass flux and inlet temperature), bundle average flow conditions obtained with the heat balance are no longer uniquely related to local flow conditions in the neighborhood of a given rod. To circumvent this difficulty, subchannel analysis is an appropriate and commonly applied numerical approach to determine the local flow conditions. In such analysis, the whole flow area of a rod bundle is divided into a row of parallel, laterally interconnected subchannels. Conservation equations of mass, momentum and energy are then established for each subchannel individually. The main challenge arising in subchannel analysis is flow interactions in lateral direction between adjacent subchannels¹, whose contribution to interchannel exchange of mass, momentum and energy must be taken into account in the basic equations. Consequently, the conservation equations for individual subchannels in a rod bundle are coupled and can only be solved with proper numerical techniques. More importantly, prediction accuracy of subchannel flow parameters, i.e. subchannel mass and enthalpy distribution, depends strongly on modeling of the interchannel mixing, which are normally expressed with additional constitutive equations.

Disregarding the forced lateral interchannel exchange effects caused by extra constructive elements, such as grid spacer, mixing vane or wire wrap, the natural interchannel mixing of

¹In the current study, the flow interacting in lateral direction between adjacent subchannels is referred to as *interchannel mixing*.

a vertical upward¹ two-phase flow in a rod bundle can be normally decomposed into three elemental components [47, 72]:

- Turbulent mixing (TM) that occurs from the stochastic flow fluctuations. Due to the irregular nature of turbulent fluctuation, turbulent mixing is considered to be a non-directional mixing effect.
- Diversion cross flow (DC), which is induced by lateral mean pressure gradient between adjacent subchannels. Different from turbulent mixing, diversion cross flow is a directional mixing effect, which prevails in the opposite direction of the lateral pressure gradient.
- Void drift (VD) is a special phenomenon that occurs only under two-phase flow conditions. According to a phenomenological conception proposed by Lahey and Moody [47], void drift results from a lateral migration of the gaseous phase (void) due to a strong tendency of two-phase system approaching an equilibrium state of phase distribution.

The above subdivision is rather arbitrary and may not be unique. Furthermore, the implicit assumption made that the elemental components can be treated separately may be questionable. Under real flow conditions, all the three effects occur simultaneously and may also influence each other. Nevertheless, this subdivision is very helpful for developing subchannel analysis codes, for it simplifies the mathematical formulation of lateral interchannel exchange terms due to the individual mixing effects. Hence, this decomposition was adopted in the current study.

Among the three components, physical mechanism of void drift is not yet well clarified. Lahey and Moody [47] referred void drift to be a phenomenon resulting from the strong tendency of a two-phase system approaching a fully developed, equilibrium state of void fraction distribution. The void drift model proposed by Lahey and Moody [47] combines the mixing effect due to turbulent mixing and void drift. Although this model is widely adopted in subchannel analysis codes (for instance in the modified COBRA-IIIC [70], in ASSERT-4 [93], in MATRA [33] etc.), geometrical and thermal-hydraulic parameters concerning two-phase flow behaviors are poorly represented. Systematical investigations on void drift covering a wide range of geometrical and thermal-hydraulic parameters are still highly desired for developing more physically reliable models. However, due to the complex nature of two-phase flow systems and the coexistence of the three elemental mixing effects, experimental determination of the individual components in a proper separate manner is not only time- and cost-demanding but also technically restricted. In contrast, a systematic numerical simulation of the two-phase interchannel mixing with CFD code can provide useful information about the physical mechanism occurring in the void drift process. Compared to subchannel analysis code, CFD code solves flow dynamic problems with a much finer mesh structure and in a more physical way. The interchannel mixing terms are directly solved in the conservation equations rather than modeled with constitutive models. Furthermore, interphase exchange terms are also taken into account. Therefore, more detailed information about two-phase flow behaviors can be obtained. A better understanding of the void drift phenomenon and a modification of the void drift models for subchannel analysis can be achieved.

¹Flow behavior in horizontally arranged rod bundles, in which buoyancy force influences interchannel exchange [13, 26, 91], is not the subject of the current study.

1.2 Objectives of this study

In the present study, local flow behaviors of subchannels in rod bundle geometry will be investigated using both subchannel and CFD approach. The primary aim of this study is, based on a detailed systematical CFD analysis, to develop new models describing the two-phase interchannel mixing (especially void drift) for application in subchannel analysis. Furthermore, prediction accuracy of selected empirical CHF correlations will be assessed based on the developed interchannel mixing models. The entire study is divided into six subtasks:

(I) **Preparation of experimental data with rod bundle geometry**

For validation of numerical codes, experimental results of NUPEC BFBT 8×8 square rod bundle benchmark [59] and ISPRA 4×4 square rod bundle benchmark [31] will be used. These benchmark investigations cover a wide range of flow parameters of both BWR and PWR conditions. The experimental results of subchannel flow parameters and critical powers will be prepared for further subtasks.

(II) **Assessment of currently available interchannel mixing models in MATRA**

The MATRA (Multichannel Analyzer for steady states and Transients in Rod Arrays) code [107] developed by KAERI (Korean Atomic Energy Research Institute) based on COBRA-IV-I [86] will be used for subchannel analysis in the current study. In order to investigate the performance of currently available interchannel mixing models in MATRA, selected test cases from rod bundle benchmark in subtask (I) will be recalculated with MATRA. Focus will be put on void drift models in MATRA. Possible improvement demand of the currently available void drift models in MATRA will be identified in this subtask.

(III) **Simulation of two-phase flow behavior in subchannels of a rod bundle geometry with CFD code and development of new models for interchannel mixing**

The commercial CFD code Ansys CFX, release 12.1, will be used in this study for CFD analysis. In this subtask, two-phase flow behavior in subchannels of a rod bundle geometry will be simulated. Systematic CFD investigation covering a wide range of geometrical and thermal-hydraulic parameters of PWR conditions will be carried out. Main parameters affecting void drift will be formulated in dimensionless factors, with which a new void drift model will be proposed. This model will be implemented into MATRA for validation calculation in the subsequent subtask.

(IV) **Validation of the proposed void drift model**

For validation of the proposed void drift model, the prepared rod bundle benchmark results in subtask (I) will be used. Both subchannel flow parameters and critical powers can be used for validation.

(V) **Assessment of selected CHF correlations**

Based on the validated new void drift model, some CHF correlations will be assessed.

The main contribution of this study will be the development of a new model describing void drift, which can also be implemented into other subchannel analysis codes. Furthermore, the experimental database established in this study of subchannel flow parameters and critical powers can be used for validation of other subchannel analysis codes.

2. State of the art

Due to its crucial importance in subchannel analysis, continuous efforts have been made to investigate the physical mechanism of interchannel mixing and hence to establish proper modeling approaches in subchannel analysis codes. The decomposition of the natural interchannel mixing effect¹ into the three elemental components, i.e. turbulent mixing (TM), diversion cross flow (DC) and void drift (VD), was adopted in the current study. This decomposition is very helpful for establishing a subchannel analysis code, provided proper modeling approaches are applied to the individual mixing effects. Among the three elemental effects, diversion cross flow is directly solved with a transverse momentum equation (see chapter 3.1.1). In contrast, constitutive equations are required to describe turbulent mixing and void drift.

In single phase cases, where void drift does not exist, turbulent mixing is the only mixing effect to be modeled. As the first noticeable review on this subject, the contribution given by Rogers and Todreas [65] might be mentioned. In recent years, sophisticated CFD approaches were also applied to investigate the single phase turbulent mixing with very promising outcomes [6, 7, 15, 89]. It is commonly believed that the single phase turbulent mixing induces, if any, negligible net mass exchange between interacting subchannels. An equal-mass-exchange (EM) model, which hypothesizes that lateral mass flow rate from subchannel i to j is equal to that simultaneously from subchannel j to i , can describe the single phase turbulent mixing with sufficient accuracy. But the EM model does not exclude possibilities of a net transfer of momentum and/or energy, which depends on a difference in velocity and/or enthalpy that may exist between interacting subchannels. The most important parameter is a turbulent mixing coefficient β as introduced by Rowe [67] or similar parameters characterizing the effective turbulent mixing velocity. Dependence of the turbulent mixing coefficient β on flow conditions (for instance Reynolds number) and subchannel geometries (P/D ratio etc.) can normally be expressed with empirical correlations [63, 64].

The situation in two-phase cases is more complicated. Experimental observations demonstrated that two-phase interchannel mixing is not equal-mass based. In contrast, considerable net mass exchanges between interacting subchannels were reported [29, 48]. The equal-mass-model is hence not appropriate for modeling the two-phase interchannel mixing. Instead of that an equal-volume-exchange (EV) model was proposed by Lahey and Moody [47], which assumes an exchange of fluid of the same volume but different average densities between interacting subchannels. However, the EV model leads always to an uniform void fraction distribution at the fully developed, equilibrium state. The highly non-uniform phase distribution observed in experiments [29, 48, 72, 85] between interacting subchannels of different cross-sectional areas can not be predicted with the EV model. Although, physical mechanism causing the non-uniform phase distribution is not yet quite understood, it is in general referred to be induced by an additional mixing effect, i.e. void drift (VD). A new phenomenological two-phase interchannel mixing model incorporating turbulent mixing (TM) and void drift (VD) proposed by Lahey et al. [49] seems to be able to predict the non-uniform phase distribu-

¹Forced interchannel mixing is not subject of the current study. One recent reference on this subject is for instance [5].

tion in subchannels. This approach is hence adopted in state-of-the-art subchannel analysis codes, for instance in THERMIT-2 [42], in the modified COBRA-IIIC [70], in FIDAS [87, 88], in ASSERT-4 [93] and in MATRA [33, 106].

In this chapter, experimental investigations on the two-phase interchannel mixing phenomena in the past decades were first reviewed, followed by a brief summary of modeling approaches on two-phase interchannel mixing proposed in diverse subchannel analysis approaches.

2.1 Experimental studies on two-phase interchannel mixing phenomena

2.1.1 Experimental studies: a brief summary

Since operation condition of a nuclear fuel rod bundle has normally high pressure, temperature and high heat flux, a full scale experimental investigation of two-phase flow behaviors in fuel assemblies is time- and cost-demanding. In order to simulate the two-phase steam-water flow, a two-phase mixture of air-water under atmospheric conditions was often used. Despite the fact that the ratio of liquid phase density to gaseous phase density and the surface tension of a air-water two-phase system are much higher than that of a steam-water two-phase system under high pressure, it is assumed that some characteristic trends and conclusions obtained in the air-water system can be applied to the high pressure steam-water system. Furthermore, instead of a full-scale fuel rod bundle (for instance a 18×18 square rod bundle representing a PWR fuel assembly and a 8×8 square rod bundle representing a BWR fuel assembly), a rather simplified geometrical system simulating the real fuel rod bundle was normally employed as test section. Two groups of works can be classified: experiments in a underscaled rod bundle and experiments in two parallel laterally interconnected subchannels (two-channel system). The advantage of a scaled rod bundle geometry lies in its closeness to a real fuel assembly compared to a two-channel system. All the three subchannel configurations (center, wall and corner) encountered in a fuel assembly can be investigated. However construction, operating costs and complexities of a rod bundle are normally much higher than that of a two-channel system. Therefore, a two-channel system is more preferred for the purpose to obtain fundamental information about the two-phase interchannel mixing.

Previous research on two-phase interchannel mixing can be traced back to Rowe and Angle in 1967 [69], who reported the cross flow mixing between two parallel subchannels under boiling conditions. The experiments were carried out with water at a high pressure (62 bar) flowing upwards through a heated test section made up of two subchannels of different cross-sectional areas. Two test sections with different gap clearance (2.0 mm and 0.51 mm, respectively) as depicted in Fig. 2.1 were investigated. For given inlet conditions (temperature, pressure and flow rate), flow split at the test section outlet was adjusted, in order to equalize the pressure of the two subchannels at the end of the test section, at which data on enthalpy and mass flux of the two subchannels were recorded. The measurement data indicated a dependence of the two-phase interchannel mixing upon flow quality. The measured amount of interchannel mixing in the test section of 2.0 mm gap size reached a peak at a low flow quality and then decreased at high flow qualities. This observation suggests that two-phase flow regime may have a significant influence on the two-phase interchannel mixing. One further important observation was that two-phase interchannel mixing depends also on gap clearance. For the relative closer spaced test section with the gap size of 0.51 mm, no significant change in mixing during boiling process was observed as in the case of 2.0 mm gap size. Therefore, when comparing measurement results of different researchers one should be aware of the

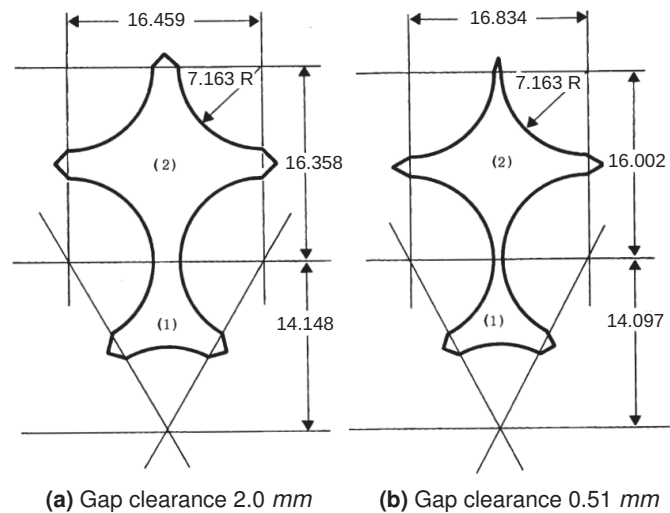


Fig. 2.1: Subchannel cross section with dimension in *mm* (Rowe and Angle [69]).

geometrical dimension of the test section, with which the results were established.

In 1969 Schraub et al. [79] carried out measurement of air-water two-phase flow structure in a nine-rod bundle (3×3 square). Compared to a normal BWR fuel assembly, the bundle was oversized with a rod diameter of 25.4 mm and a pitch of 35 mm . The flow quality was varied from 11 to 62% (annular flow regime). Isokinetic sampling technique was used, in order to obtain information on local flow quality distribution within subchannels of the nine-rod bundle. As depicted in Fig. 2.2, a highly non-homogeneous phase distribution was observed. The corner subchannel has a maximum flow quality of only 5%, whereas the maximum flow quality in the more open center subchannel is higher than 35%. Lahey and Moody [47] speculated the reason of the observed trends is due to a tendency of the gaseous phase “drifting” from corner subchannels to center subchannels with relative larger flow velocities and hence proposed their famous phenomenological void drift model, which considered void drift as an additional interchannel mixing effect to turbulent mixing.

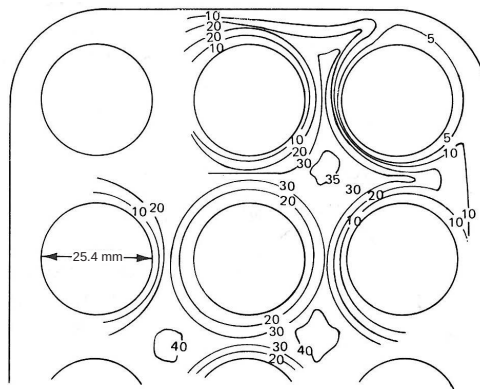


Fig. 2.2: Radial flow quality profile of air-water two-phase flow in a nine-rod bundle (Schraub et al. [79]).

To the present author’s knowledge, the first noticeable contribution to the two-phase inter-channel mixing phenomena between two laterally connected channels was made by van der Ros [101] in 1970 with a air-water two-phase system. The investigated test section was made up of two identical interconnected channels. Air bubbles with well defined bubble diameter in the order of 1 mm were injected into just one of the channel at inlet. Due to the non-equilibrium

inlet condition, the air bubbles were redistributed downstream towards test section outlet. Two test sections of the same subchannel dimension (hydraulic diameter 10 mm) but different gap size (2 mm and 4 mm) were tested. Van der Ros [101] hypothesized that interchannel exchange of individual phases appears due to different mechanisms. While interchannel mixing of the gaseous bubbles behaves rather like a diffusion process, the exchange of the liquid phase is induced by differences in axial pressure gradient between the interacting subchannels. It was also found that the gaseous interchannel mixing increases with the average void fraction to a peak value and then decreases. With rising liquid phase mass flux, the transient time of the air bubbles in the test sections was decreased, which leads further to a reduction of the gaseous interchannel mixing. Furthermore, it was also found that the gaseous mixing is larger with the test section of a wider gap clearance of 4 mm.

In 1971 Lahey et al. [48] performed diabatic measurement on mass flux and enthalpy distribution in a uniformly heated nine-rod bundle (3×3 with a rod diameter of 14.478 mm and a pitch of 18.475 mm) with a steam-water mixture under typical BWR operating conditions. Isokinetic sampling technique was applied to obtain the average flow parameters in corner, wall and center subchannel, respectively. As depicted in Fig. 2.3, a significant flow and enthalpy difference could be found in the different subchannel types. The corner subchannel (subchannel 1) shows quality and mass flux lower than the bundle average values despite its power-to-flow ratio was higher than the bundle average values. In contrast, the center subchannel (subchannel 3) has higher quality and mass flux than the bundle average values. This trend was in agreement with that observed by Schraub et al. [79] in an adiabatic air-water two phase flow in a nine-rod bundle. It was concluded by Lahey et al. [48] that this observed trend of gaseous phase accumulating in center subchannels is related to an affinity of the gaseous phase for less-obstructed high velocity regions, i.e. the center subchannels as in the case of the nine-rod bundle. According to flow regime transition criteria proposed by Mishima and Ishii [57], for the given system conditions (pressure 69 bar and bundle average mass flux $1356 \text{ kgm}^{-2}\text{s}^{-1}$), transition from bubbly to slug flow regime happens at a flow quality about 0.03 and transition from slug to annular flow regime at a flow quality about 0.08¹. As observed in Fig. 2.3, an enhancement of interchannel mixing can be seen at a flow quality related to the slug-annular flow regime transition. As the quality further increases in the annular flow regime, the mixing effect seems to decrease with the quality. No experiment was carried out in the bubbly flow regime, hence no trend on the flow distribution can be concluded in the bubbly flow regime.

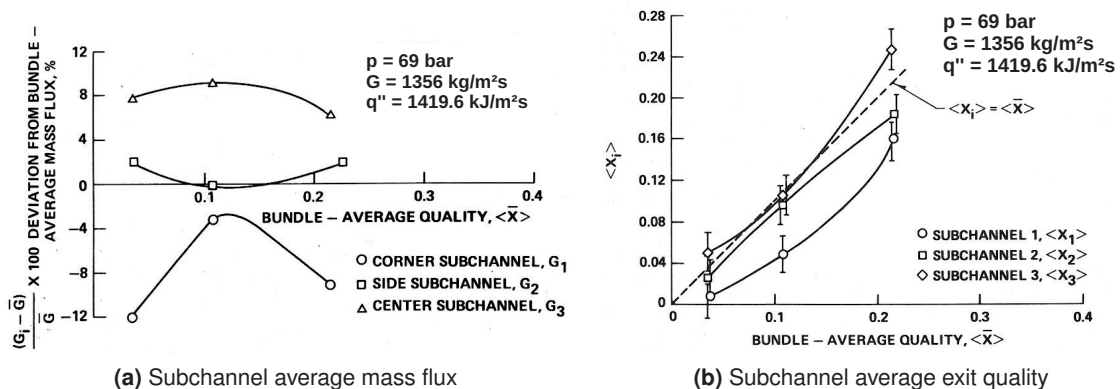


Fig. 2.3: Comparison of the subchannel average exit conditions (Lahey et al. [48]).

¹Although the transition criteria proposed by Mishima and Ishii [57] were established based on experiments with a tube geometry, qualitative transition trends in rod bundle geometry can also be described.

Later in 1972 Gonzalez-Santalo and Griffith [29] measured both effective two-phase interchannel mixing velocity and fully developed equilibrium flow distribution in a two-channel system simulating subchannels of a typical BWR fuel assembly with a air-water system under atmospheric conditions. The air-water mixture was fed unevenly into the two laterally connected subchannels, whose axial (main streamwise) communication length could be varied typically from 57 mm to 387 mm. Phase distribution profiles were measured at the exit of the subchannel. In order to achieve the fully developed state, the two subchannels were allowed to communicate along the entire axial length of 2.44 m of the test section. The fully developed state was considered to be established, when the exit flow rates of the individual subchannels are independent of the inlet phase distribution. The most important findings are summarized as follows:

- The effective mixing velocity is strongly dependent on flow regime. A sharp increase in magnitude of the effective mixing velocity takes place at the transition from bubbly to slug flow regime. The maximum value of mixing velocity occurs apparently in the slug flow regime. Furthermore, the effective mixing velocity depends also on mass flux. In bubbly flow regime the mixing velocity decreases as mass flux increases. In slug flow regime, where the maximum value of mixing velocity occurs, no significant dependence of the mixing velocity on the mass flux can be identified^I.
- The fully developed flow distribution, i.e. the void fraction distribution at equilibrium state, depends on test section geometry. In the case of test section consisting of two identical channels of the same dimension, the two-phase mixture was found equally distributed in the two channels at the equilibrium state^{II}. However, in another test section configuration with one channel considerable larger than the other one (cross-sectional area ratio about 1.5), the void fraction distribution was non-equal in the fully developed state. Furthermore, this non-equal void fraction distribution at equilibrium state depends on flow regime. In bubbly flow regime, a higher concentration of the gaseous phase was observed in the smaller channel. But as void fraction increases, a higher gaseous phase concentration in the larger channel was reached after a transition from bubbly to slug flow regime. Further increasing of the void fraction led to a slowly decrease in the gaseous concentration in the larger subchannel, but it was always larger than that in the smaller channel.

From the above summary it can be concluded, that two-phase interchannel mixing phenomena depends strongly on flow regime, also for bubbly and slug flow regime. The modeling of mixing coefficient and void fraction distribution at equilibrium state should be carried out for bubbly and slug flow regimes separately.

In Columbia University 1972, flow and enthalpy measurement of a steam-water two-phase flow was carried out by Castellana and Casterline [14] with an electrically heated 4×4 square rod bundle at two pressure levels of 34.5 bar and 82.7 bar. The investigated rod bundle geometry, as depicted in Fig. 2.4, with a rod diameter of 10.7 mm and a pitch of 14.1 mm is similar to a typical light water reactor (LWR) fuel rod bundle. While the axial (main streamwise) heat flux distribution was uniform for individual rods, the radial heat flux profile was non-uniform. Heat flux of the colder rods (denoted with “C”) was 86% of that exerted on the hotter rods (denoted with “H”). The bundle average mass flux was varied from 1300 kgm⁻²s⁻¹ to 4000 kgm⁻²s⁻¹ covering the typical mass flux range in a LWR. The average heat flux was adjusted, so that both subcooled and saturated boiling were able to be established in the test section exit. The average mass flux and enthalpy of two sampled center subchannels, namely channel 5 and

^ISince no measurement was carried out in annular flow regime, no conclusion can be made to the behavior of the mixing velocity in this regime.

^{II}This finding was confirmed later by Sadatomi et al. [72] in their experimental study of flow redistribution with two identical channels in slug and annular flow regimes.

11 (outlined in Fig. 2.4 with continuous lines), were measured by separating the two-phase flow of the individual channel flows, respectively. The sampling was carried out without flow or pressure alteration by controlling the pressure level in the sampled and the corresponding not sampled channel to be equal. Despite an uniform inlet mass flux in all the subchannels, the

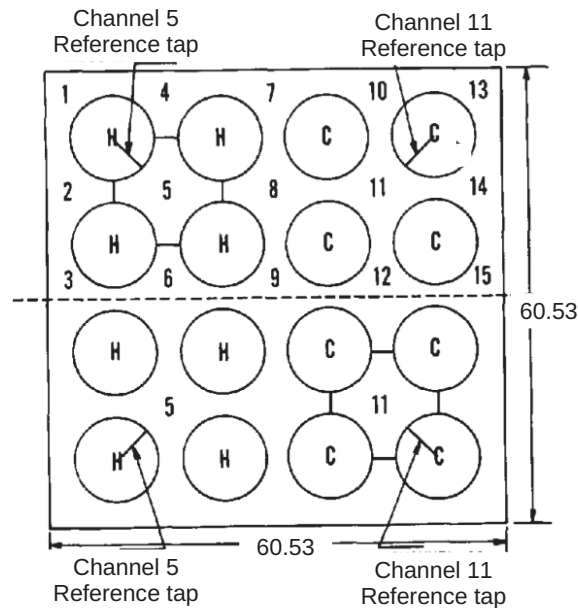


Fig. 2.4: The 4×4 square rod bundle conducted in Columbia University (Castellana and Casterline [14]), dimension in *mm*; the Arabic numbers denote subchannels. *H* and *C* denote the hotter rods with relative higher heat flux and the colder rods with relative lower heat flux, respectively.

measured mass flow and enthalpy in channel 5 and 11 indicated a non-uniform distribution of the two-phase flow in the subchannels at the test section exit. With increasing bundle average flow quality, a flow diversion out of the center subchannels into the peripheral subchannels could be concluded, because the measured mass flux of both sampled center subchannels were lower than that of the bundle average value. It was explained by the authors, due to the higher ratio of heat input to flow area in the center subchannels, boiling will be first established there. Boiling will cause a diversion of flow away from the subchannel as a consequence of an increase in fluid volume and frictional pressure drop. The observation made in this study confirms that two-phase interchannel mixing is not equal-mass based. Furthermore, the explanation given by the authors that an increase in frictional pressure drop in subchannels due to boiling provide an interesting point for further discussion. Even in an axial and radial uniformly heated rod bundle, the ratio of thermal load to flow area is always different for individual subchannel types. An earlier boiling establishment in certain subchannel types which leads to diversion cross flow is almost inevitable. The interchannel mixing effect of diversion cross flow might be always present at least in a developing two-phase rod bundle flow.

Tsuge et al. [100] conducted in 1979 void fraction measurement with a air-water two-phase system in a two-channel test section as shown in Fig. 2.5 (a). The test section consisted of two square channels with different cross section areas. The ratio of the channel width W_1/W_2 was varied from 0.17 to 1.0. Void fraction distribution along the center line of the two subchannels were measured with void probes, as shown in Fig. 2.5 (b) for the case of W_1/W_2 equal to 0.17 and 2 ms^{-1} inlet superficial velocity of both phases. Though the inlet condition was the same in both channels, a clear tendency of gaseous phase accumulating in the larger channel 2 was observed. The radial void fraction profiles in both channels show a core peaking profile, i.e., the local gaseous phase concentration within individual subchannels is higher in the subchannel bulk area. Despite a large difference to typical subchannel geometries

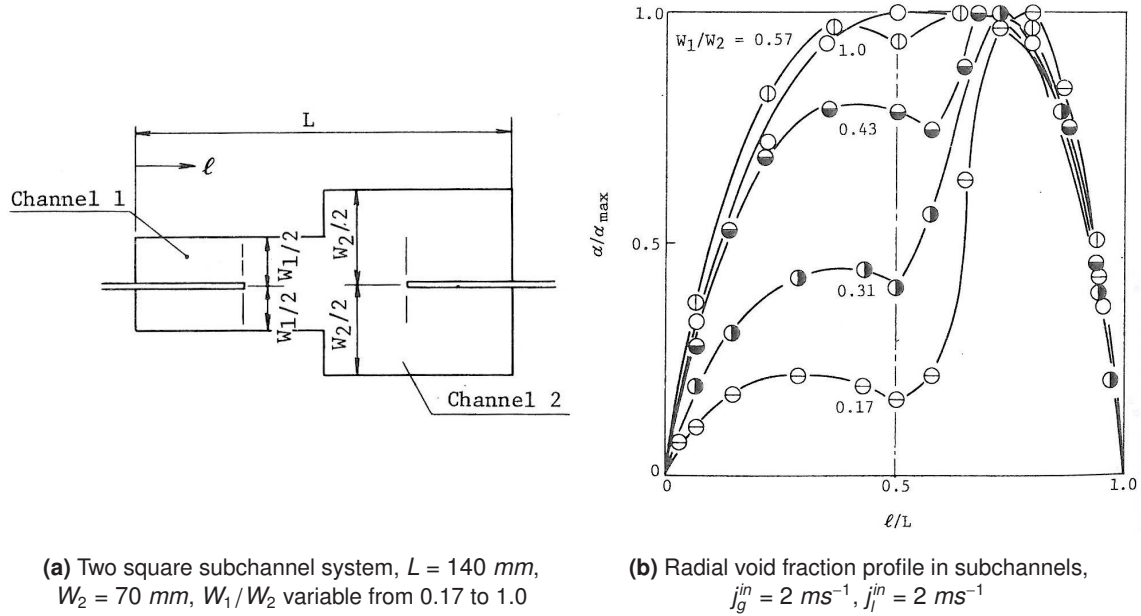
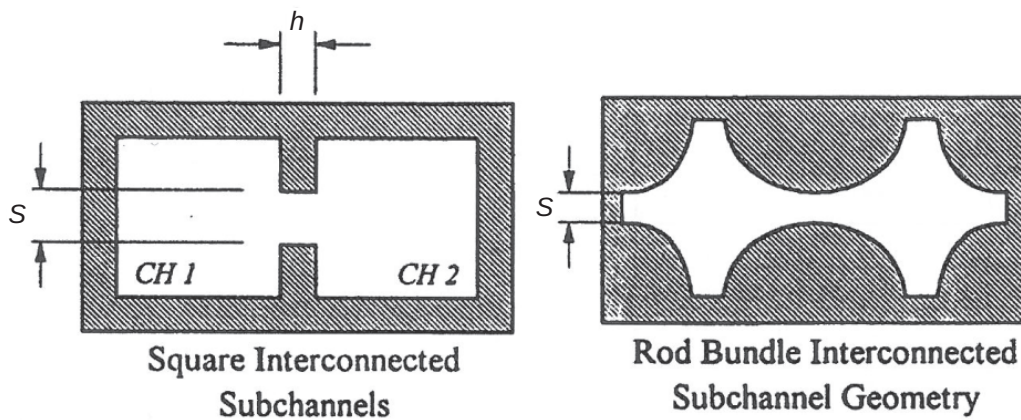


Fig. 2.5: Test section and radial void profile (Tsuge et al. [100]).

encountered in a nuclear fuel assembly, a distinguished feature of the measurement carried out by Tsuge et al. lies in the measured radial void fraction profile in the two interacting subchannels. In contrast, in most of the experimental investigations conducted to study two-phase interchannel mixing only the channel average void fraction was determined. As will be discussed later, beside the average void fraction, local radial void fraction profile may be also important to understand two-phase interchannel mixing specially in bubbly flow regime.

In 1983 Sterner and Lahey [85] performed measurement to determine the fully developed, equilibrium flow quality and mass flux distribution in a 2×2 square rod bundle with a air-water two phase flow. Isokinetic sampling technique was used to measure the flow in three subchannels representing center, wall and corner subchannel of the rod bundle, respectively. All dimensions of the test section (i.e. rod diameter, pitch etc.) were set twice of a typical BWR fuel rod bundle, in order to partially compensate for possible large bubble sizes of air-water system under lower pressure levels. For two bundle average mass flux levels ($451.6 \text{ kgm}^{-2}\text{s}^{-1}$ and $903.2 \text{ kgm}^{-2}\text{s}^{-1}$) the bundle average void fraction was varied in the range of 0% to 52.7%, so that bubbly, slug and churn flow regime were able to be achieved. For all the test runs it was clearly demonstrated that the equilibrium void fraction of corner subchannel with the smallest hydraulic diameter (15.9 mm) is lower than of the test section average value, while the equilibrium void fraction of center subchannel (hydraulic diameter 35.7 mm) is greater than the test section average. In contrast, void fraction of the wall subchannel was found comparable to the bundle average value. In summary, for all the investigated two-phase flow regimes (bubbly, slug and churn) a clear tendency of gaseous phase towards the more open and larger wall and center subchannels could be concluded. This observation confirms the findings obtained by Schraub et al. [79] in annular flow regime. However, the measurement results of Sterner and Lahey [85] on the equilibrium void fraction distribution in bubbly flow regime are different with that observed by Gonzalez-Santalo and Griffith [29], in which it was found that gaseous phase concentrates not in the larger but in the smaller channel. As will be discussed later, more detailed information about bubble size may be necessary to explain the different tendencies observed.

In 1982 Tapucu et al. [91] measured mass exchange rate and pressure difference between two identical square channels (hydraulic diameter of 12.7 mm) laterally interconnected with a gap of 1.5 mm clearance (see Fig. 2.6 (a)). A air-water two-phase mixture was applied as working fluid. Inlet flows of the same mass flux but substantially different void fractions were introduced into the two subchannels. Due to the inlet void fraction difference, interchannel exchange through the gap occurs. Subchannel average void fractions along the test section were determined by measuring electrical conductivity variation between two thin plate electrodes applied on two opposite faces of each channels. Liquid phase exchange between the two channels was obtained by injecting a NaCl solution into the channel with higher inlet void fraction and measuring the salt concentration variation in both channels by sampling the liquid phase at various axial locations along the test section. Several years later in 1988, the same experimental procedure was applied by Tapucu et al. [92] to two identical interconnected center subchannels of a square rod bundle with tighter lattice compared to normal fuel assemblies in BWRs and PWRs (gap clearance 1.7 mm and channel hydraulic diameter 7.2 mm , see Fig. 2.6 (b)). The main findings with the two test sections are similar and hence summa-



(a) Two square interconnected subchannels [91], (b) Two rod bundle interconnected subchannels [92],
 $S = 1.5\text{ mm}$, $h = 3.17\text{ mm}$ and $D_h = 12.7\text{ mm}$ $S = 1.7\text{ mm}$ and $D_h = 7.2\text{ mm}$

Fig. 2.6: Schematic diagram of test sections (Tapucu et al. [91, 92]).

rized together. In test runs with high inlet void fractions (slug-annular flow regime), a clear gaseous and liquid phase exchange between the two interacting subchannels were observed. Although no measurement on void fraction distribution at the fully developed equilibrium state was carried out, an asymptotic behavior of the channel average void fractions along the test section axial (main streamwise) length indicating a tendency towards an equilibrium state was observed. Probably due to the rather small gap clearance, no or negligible phase exchange was able to be determined in test runs with low inlet void fractions (bubbly flow). The conclusion given by Tapucu et al. [92] that in low void fraction ranges the equilibrium void fraction distribution between two identical subchannels is non-uniform, may be questionable. But the observation provides clearly a hint, that the narrow gap can build up a resistance to the interchannel mixing under two-phase flow condition as already be reported by Rowe and Angle [69].

Experiments with a air-water two-phase flow in a simple two-channel system (see Fig. 2.7) was conducted in 1985 by Sekoguchi et al. [80] to determine the mass flow rates of individual phases in each subchannels at the equilibrium state. The test section consisted of a rectangular duct measured $20.0\text{ mm} \times 32.2\text{ mm}$ surrounding a tube of 16.0 mm outer diameter. With an eccentric arrangement of the tube, two subchannels with different cross-sectional areas (ratio about 2 to 1) were formed. The two subchannels were connected with two gaps of the same gap clearance of 2.0 mm . Inlet superficial velocities of each phase were controlled to be the same in both subchannels: i.e. $j_{g,A}^{in} = j_{g,B}^{in}$ and $j_{l,A}^{in} = j_{l,B}^{in}$. It was found that, in the studied flow regimes, i.e. slug, forth and annular regimes, the superficial velocity of

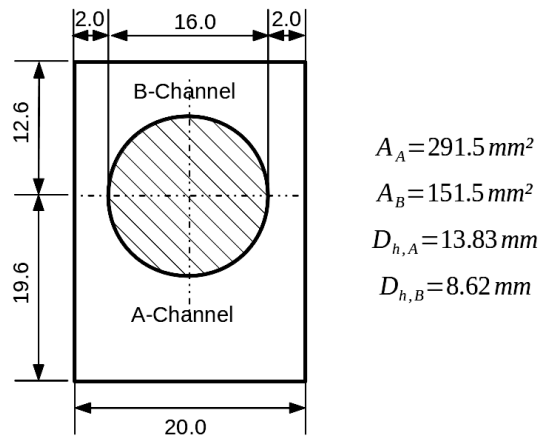


Fig. 2.7: Schematic diagram of Sekoguchi et al. test section [80], dimension in *mm*.

the gaseous phase in the larger subchannel (A-Channel) always exceeds that in the smaller subchannel (B-Channel). Furthermore, the volumetric flow quality, defined as $j_g/(j_g + j_l)$, in the larger subchannel was also found higher than that in the smaller subchannel. These two findings indicate apparently a larger affinity of the gaseous phase to the more open subchannel (A-Channel) with larger cross-sectional area. The observation coincides to that found by Schraub et al. [79], Lahey et al. [48] and Sterner and Lahey [85] in the investigated slug to annular flow regime.

In the past decades, a large amount of experimental investigations on two-phase interchannel mixing phenomena with air-water two-phase flow under atmospheric conditions were carried out in Kumamoto University, Japan (see Sato et al. 1987 [77], Sadatomi et al. 1994 [72], Sadatomi et al. 2004 [73], Sadatomi et al. 2006 [74] for investigations on void fraction distribution at equilibrium state and see Sadatomi et al. 1994 [72], Kawahara et al. 2004 [37], Kawahara et al. 2004 [40], Sadatomi et al. 2005 [75], Kawahara et al. 2009 [41] for investigations on interchannel mixing effect due to void drift). The applied geometrical models, as schematically depicted in Fig. 2.8, varied from simple two-channel systems to a 2×3 multi-rod bundle. The covered flow regimes were mainly slug, churn and annular flow regime. Since test loop construction, experimental procedure and measurement techniques of the above mentioned investigations were quite similar, they are summarized here together.

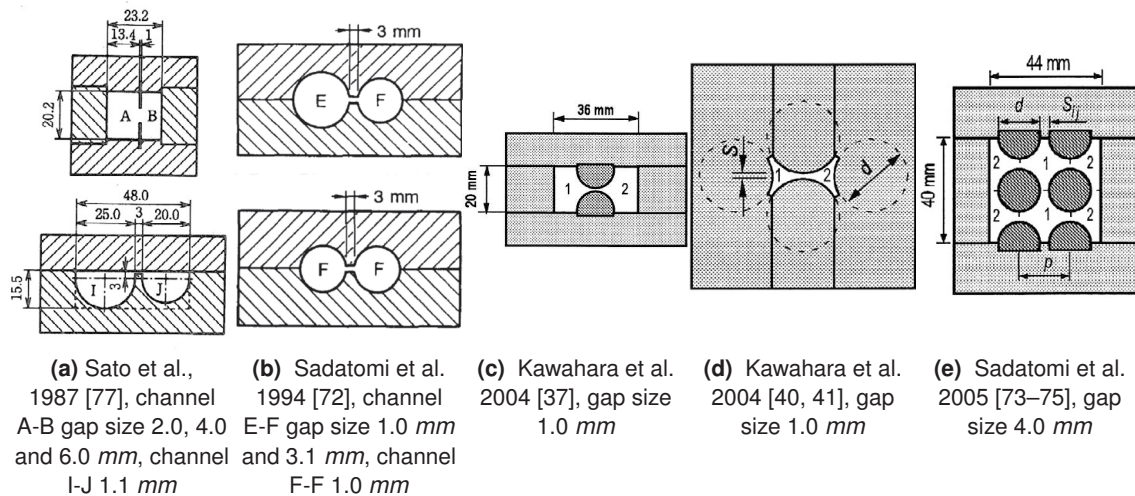


Fig. 2.8: Test sections of experimental investigations on two-phase interchannel mixing phenomena conducted in Kumamoto University, Japan.

All the test sections were made up of three parts: an entry section, a connection section and a discharge section. In the entry and discharge section, the gap between adjacent subchannels was completely blocked so that no interchannel mixing exists, while in the connection section the blockage of the gap was removed so that interchannel mixing through the gap can occur. The most important assumption made by the authors is that turbulent mixing (TM), which is the only active mixing effect at equilibrium state, induces neither net mass exchange nor net volume exchange between interacting subchannels. Furthermore, diversion cross flow was assumed by the authors to be prevented with the following two imposed conditions:

1. Equal pressure gradient of all the subchannels in the entry section
2. Equal time-averaged mean pressure in each subchannels at both inlet and outlet of the connection section

Under these conditions, the two-phase mixture at the end of the connection section was isokinetically split into individual subchannels and discharged. After passing the discharge section the two-phase mixture was finally separated and exit mass flow rates of each phases in individual subchannels were then measured. In order to study the void fraction distribution at equilibrium state, the connection section was extended to the maximal possible length depending on test loop construction. Inlet flow rate ratios of both phases in one defined channel to that in the whole test section was changed step by step according to the measured exit mass flow rates. The equilibrium state was considered to be established, when the exit mass flow rates of both phases in each subchannel are equal to the respective inlet flow rates within uncertainty ranges. The measured exit mass flow rates of both phases were considered to be the phase distribution at equilibrium state. To investigate interchannel mixing effect due to void drift, fixed but non-equilibrium mass flow rate distribution was introduced into the test section inlet. Series of test runs were carried out by changing the connection section length systematically from small to large values. Thus data on interchannel mixing due to void drift in the axial (main streamwise) direction were able to be obtained. The main results and conclusions are summarized here:

- Void fraction distribution at equilibrium state is uniform for two identical interconnected subchannels. In case of interacting subchannels with dissimilar cross-sectional areas, a non-uniformity of void fraction distribution exists in the equilibrium state. A higher concentration of gaseous phase in subchannels with larger cross-sectional area was observed, especially in slug or churn flow regime. This non-uniformity became less significant as void fraction increases further to annular flow regime. Although less measurements were performed in bubbly flow regime, some results were still available. For instance, in the experimental study carried out by Sadatomi et al. 1994 [72] with the E-F test section as depicted in Fig. 2.8 (b), it was found that at high liquid superficial velocities and low gaseous superficial velocities, the gaseous phase concentration was higher in the smaller channel F at the equilibrium state.
- Since diversion cross flow was assumed to be prevented and neither net mass nor net volume exchange was assumed to be resulted from turbulent mixing, the measured interchannel mixing was assumed by the authors to be purely induced by void drift. A void diffusion coefficient based on the void drift model proposed by Lahey and Moody [47] characterizing the effective mixing velocity due to void drift was introduced and determined with help of the experimentally obtained interchannel mixing data. It was found that void diffusion coefficient depends strongly on flow regime. This finding coincides to that of Gonzalez-Santalo and Griffith [29], i.e., two-phase effective interchannel mixing velocity depends strongly on flow regime.

2.1.2 Conclusion and discussion

Conclusion

Despite the large differences in the geometrical and operation conditions applied in the diverse experimental investigations as summarized above, some common conclusions on two-phase interchannel mixing can be drawn here:

- In general, a strong dependence of the two-phase mixing phenomena on flow regime has been reported and confirmed in various investigations. Furthermore, both mass flux and geometrical dimension have influence on the two-phase interchannel mixing.
- Although no general theoretical description of the interchannel mixing under two-phase conditions could be derived, a clear tendency of approaching a fully developed, equilibrium state was observed in diverse investigations. This provides at least a possibility of a phenomenological modeling of the two-phase interchannel mixing phenomena. As proposed by Gonzalez-Santalo et al. [29] and Lahey et al. [47, 49], driving force of the two-phase interchannel mixing is assumed to be a void fraction difference between the existing state and the equilibrium state of void fraction distribution between interacting subchannels $[(\alpha_i - \alpha_j) - (\alpha_i - \alpha_j)_{EQ}]$. The void fraction difference at equilibrium state $(\alpha_i - \alpha_j)_{EQ}$ characterizes the final state due to the mixing process. The proportional ratio between mixing flow rate and the driving force of mixing provides a measure of the effective two-phase interchannel mixing velocity.
- Void fraction distribution at equilibrium state in subchannels of a rod bundle geometry is highly non-uniform. In the rod bundle measurement conducted in [74, 79, 85], dissimilar phase distributions were established in corner, wall and center subchannel, respectively. The same trend was also observed in investigations with simple two-channel systems consisting of two subchannels with different cross-sectional areas [29, 72, 77, 80, 100]. A clear tendency of void drift, which relates to an affinity of the gaseous phase to less obstructed high mass flux subchannels, was observed in high void fraction regimes as reported by Schraub et al. [79] in annular flow regime with a nine-rod bundle, by Lahey et al. [48] in slug-annular flow regime with a nine-rod bundle, by Gonzalez-Santalo and Griffith [29] in slug-churn flow regime with a two-channel system and by Sterner and Lahey [85] in slug flow regime with a four-rod bundle. However, different observations of the void fraction distribution at equilibrium state have been reported in bubbly flow regime of relative lower void fractions. As summarized above, investigations on the equilibrium phase distribution in bubbly flow regime were carried out by Gonzalez-Santalo and Griffith [29] and Sterner and Lahey [85], both with a air-water two-phase system. In the case of Gonzalez-Santalo et al., gaseous phase void fraction was found to be higher in the smaller subchannel with lower mass flux. In the investigation of Sterner et al., however, the smaller corner subchannel showed always lower flow quality, i.e. lower void fraction, than the larger wall and center subchannels with higher mass flux. To the opinion of the present author, the results of Gonzalez-Santalo et al. should be preferred to describe the general tendency in LWR fuel rod bundles, because the geometrical dimension of the two-channel system applied by Gonzalez-Santalo et al. is much closer to a real LWR nuclear fuel assembly.
- Two-phase effective interchannel mixing velocity, as reported by Rowe et al. [69] and Gonzalez-Santalo et al. [29], reaches a maximum at a flow quality typical to slug flow regime or slug-annular transition regime. As flow quality further increases to reach annular flow regime, the two-phase mixing decreases and finally approaches the single phase level as void fraction approached unity.

Discussion about void fraction distribution at equilibrium state in bubbly flow regime

As summarized above, disputes over void fraction distribution at equilibrium state in interacting subchannels of different cross-sectional areas were reported in the bubbly flow regime. Two-phase bubbly flow structure has been intensively experimentally investigated in the past decades in pipe geometry, represented by [54, 55, 61, 82, 83, 102]. With detailed measurement results of bubble size, radial void fraction as well as phase velocity profiles and turbulence structure, the Eulerian two-fluid model has been developed and validated for predicting the bubbly flow structure with CFD approach, represented by [24, 25, 45, 99, 103]. In the current study, a proposal was hypothesized to explain the different trends of void fraction distribution at equilibrium state in bubbly flow regime based on knowledge gathered from local bubbly flow distribution in pipe geometry.

The most important conclusion on the phase distribution in a pipe two-phase bubbly flow can be summarized as that the radial phase distribution depends mainly on lift force exerted on the dispersed bubbles, since lift force acts perpendicular to the main streamwise direction. As proposed by Auton et al. [4], the volumetric lift force (dimension $[Nm^{-3}]$) exerted on dispersed bubbles by their surrounding liquid phase can be expressed as:

$$\mathbf{F}_L = -C_L \cdot \rho_l \cdot \alpha \cdot (\mathbf{U}_g - \mathbf{U}_l) \times (\nabla \times \mathbf{U}_l) \quad (2.1)$$

with $(\nabla \times \mathbf{U}_l)$ denotes the rotation of the continuous liquid phase velocity field \mathbf{U}_l . Considering a flow with Z direction as the main streamwise direction, \mathbf{U}_l can be simplified to $(0,0,w_l)$ with w_l the velocity component in Z direction. Similarly, the gaseous phase velocity \mathbf{U}_g can be given as $(0,0,w_g)$. With these simplifications, $(\nabla \times \mathbf{U}_l)$ is calculated as:

$$\nabla \times \mathbf{U}_l = \begin{pmatrix} \frac{\partial w_l}{\partial X} \\ \frac{\partial w_l}{\partial Y} \\ 0 \end{pmatrix} \quad (2.2)$$

The lift force acting on dispersed bubbles is hence given as:

$$\mathbf{F}_L = C_L \cdot \rho_l \cdot \alpha \cdot \begin{pmatrix} -w_r \frac{\partial w_l}{\partial X} \\ -w_r \frac{\partial w_l}{\partial Y} \\ 0 \end{pmatrix} \quad (2.3)$$

with w_r the relative velocity in Z direction given as $(w_g - w_l)$ and C_L is the dimensionless lift force coefficient. According to Tomiyama et al. [95], the physical mechanism of lift force can be separated into two regions depending on bubble diameter:

- For bubbles with relative small diameters, lift force is mainly induced by a non-uniformity in shear stress due to the inhomogeneous velocity field of the continuous liquid phase. In this case, the lift force coefficient C_L takes positive values. With a positive C_L , lift force acting on bubbles is opposite to liquid phase velocity gradient. Lift force will hence push bubbles towards regions with relative lower liquid phase velocity. As results, inside a pipe flow, lift force acts in the direction towards solid wall and a typical near wall peaking profile of the radial void fraction distribution can be observed. In case of a subchannel flow, bubbles are enforced to move laterally towards solid rod surface and also towards the gap region, since liquid phase velocity in the gap region is lower than that in subchannel bulk.

- As bubble size grows up reaching a critical diameter, bubbles can not keep the spherical form and become distorted. According to Tomiyama et al. [95] and recalculation by Glück [28], the critical bubble size of a air-water two-phase system under atmospheric conditions is about 5.5 *mm* to 6.7 *mm*. For large, deformed bubbles, lift force is related to the presence of a slanted wake behind bubbles. In this case, lift force is apparently caused by the interaction between the wake and the shear field. The dominant wake effect causes lift force to change its direction and C_L will take negative values. Lift force acting on bubbles is then in the same direction of liquid phase velocity gradient and will hence push bubbles towards region with relative larger liquid phase velocity. Inside a pipe flow, bubbles will be pushed towards the bulk region. A radial void fraction distribution profile peaking in the bulk region will be established. In a subchannel flow, lift force will also push bubbles away from the gap region towards subchannel bulk, since liquid phase velocity in the bulk region is higher.

Considering now the case of two subchannels of different cross-sectional areas laterally interconnected with a narrow gap, due to a higher pressure drop in the smaller subchannel, liquid velocity level in this subchannel is lower than that in the larger subchannel. The difference in liquid velocity field leads further to different lift force acting on bubbles in the two subchannels. Regarding the bubble size in the two subchannels, four possible cases will occur:

- Case I: Bubble size in both subchannels is smaller than the critical bubble size.
- Case II: Only the bubble size in the smaller subchannel is larger than the critical bubble size.
- Case III: Only the bubble size in the larger subchannel is larger than the critical bubble size.
- Case IV: Bubble size in both subchannels are larger than the critical bubble size.

In case I, lift force pushes bubbles of both subchannels towards solid rod and wall and also to the connecting gap region. Due to higher velocity level in the larger subchannel, lift force acting on bubbles is also greater than that in the smaller subchannel. This may lead to a tendency of bubbles moving to the smaller subchannel. In case II, lift force pushes bubbles in the smaller subchannel to bulk region, whereas in the larger subchannel it pushes bubbles crossing the gap and finally leads to an enhanced void fraction in the smaller subchannel. In case III, lift force will move bubbles in the larger subchannel to bulk region, whereas bubbles in the smaller subchannel will be pushed towards the gap region and cross the connecting gap. A higher average void fraction in the larger subchannel will be established. Finally in the fourth case, due to the higher velocity level, lift force acting on bubbles in the larger subchannel will prevail and a higher average void fraction in the larger channel is to be expected.

Through this brief discussion it is clear that the bubble size is an essential parameter to predict the tendency of void fraction distribution at equilibrium state. However, this information was not provided in most of the measurements summarized in this chapter. Nevertheless, the above discussion gives us some ideas to explain the opposite trends reported by Gonzalez-Santalo and Griffith [29] and by Sterner and Lahey [85]. The rod bundle used by Sterner et al. is twice oversized compared to a normal BWR fuel rod bundle. Hydraulic diameter of the smallest corner subchannel is about 16 *mm*, while that of the larger wall and center subchannel is over 25 *mm* and 35 *mm*, respectively. The relative large subchannel size enables possibilities of building up large bubbles over the critical size, at least in the larger

wall and center subchannels¹. This corresponds to the cases III or IV of the above discussion. A higher void fraction in the wall and center subchannel than in the corner subchannel is hence to be expected. In contrast, subchannels used by Gonzalez-Santalo et al. is much smaller (hydraulic diameter about 10 mm). It is fairly to assume that bubbles in both subchannels are smaller than the critical size (corresponding to the case I). The observed higher void fraction in the smaller subchannel would be not surprising. In application to a LWR fuel assembly, due to the high pressure level, low surface tension and relative small subchannel hydraulic diameters, small bubbles are prevailing if bubbly flow regime is to be expected. The case I would be close to the bubble size distribution in nuclear fuel rod bundle applications.

2.2 Modeling approach of two-phase interchannel mixing in subchannel analysis

In contrast to single phase case, modeling approach on two-phase interchannel mixing is still limited in subchannel analysis. This is mainly due to the lacking knowledge of physical mechanism of the two-phase mixing phenomena. Up to date empirical correlations incorporating strong simplifications are still the most reliable method to model the two-phase interchannel mixing in subchannel analysis codes. The most widely adopted is the phenomenological modeling approach proposed by Lahey and Moody [47] based on the experimentally observed trend of two-phase system approaching an equilibrium state. In general, two types of approaches for modeling the two-phase interchannel mixing phenomena can be found in the open literature:

1. Modeling based on an equal-volume-exchange turbulent mixing incorporating void drift (EVVD) approach
2. Modeling based on an equal-mass-exchange turbulent mixing incorporating void drift (EMVD) approach

Both approaches apply Lahey's phenomenological proposal, however different assumptions regarding the individual mixing effects have been made.

2.2.1 Equal-volume-exchange turbulent mixing incorporating void drift

The basic idea for derivation of this model was established by Lahey and Moody [47]. Under two-phase flow conditions, as summarized in chapter 2.1, a net mass transfer due to interchannel mixing has been reported by diverse researchers. In the equal-volume-exchange turbulent mixing (EV) model, it is assumed that the same volume of fluid with different densities is exchanged between interacting subchannels. Due to the density difference, net mass is transferred from subchannels of higher density to subchannels of lower density. As pointed out by Lahey and Moody [47], regardless of the magnitude of the mixing effect described by the EV model, an uniform void fraction distribution at equilibrium state in the interacting subchannels is always implied. The experimentally observed strong trends of a two-phase system approaching a non-homogeneous equilibrium state of void fraction distribution can not be predicted by the equal-volume-exchange turbulent mixing model alone. The gaseous phase apparently tends to move towards certain subchannels types. This trend was referred to as a new type of interchannel mixing mechanism besides turbulent mixing, i.e. "void drift",

¹Actually the original purpose of Sterner et al. to use an oversized rod bundle is to compensate for the large bubble sizes in the low pressure air-water two-phase system [see 85, page 6]. This somehow justifies the assumption of a large bubble size at least in the wall and center subchannels.

by Lahey et al. [48]. In order to take the void drift effect into consideration, Lahey et al. [48] hypothesized that the net two phase interchannel mixing is proportional to the non-equilibrium void fraction gradient. This model implies a tendency towards an equilibrium state of void fraction distribution. Once this state is achieved, the net exchange due to mixing ceases. This model combines the equal-volume-exchange turbulent mixing (EV) and the effect of void drift (VD), hence is also known as the EVVD model. Accordingly, the net mass flow rate per unit length due to two-phase interchannel mixing (void drift and turbulent mixing combined) from an arbitrary subchannel i to its neighboring subchannel j with a connecting gap clearance S_{ij} can be expressed as:

$$w'_{itoj} = \left(\frac{\Gamma_t}{l_{mix}} \right)_{TP} \cdot S_{ij} \cdot (\rho_l - \rho_g) \cdot [(\alpha_j - \alpha_i) - (\alpha_j - \alpha_i)_{EQ}] \quad (2.4)$$

with Γ_t is the eddy diffusivity and l_{mix} the mixing length. Hence, $(\Gamma_t/l_{mix})_{TP}$ is the effective two-phase interchannel mixing velocity. The subscripts i and j denote the average flow parameters of subchannel i and j , respectively. The subscripts l and g denote the flow parameters of the single liquid and gaseous phase, respectively. The void fraction difference term $(\alpha_j - \alpha_i)$ denotes the existing void fraction distribution, while the term with the subscript EQ denotes the void fraction distribution at equilibrium state. The difference between the two void fraction distributions is referred to as the non-equilibrium void fraction gradient [48]. As described in Eq. 2.4, the mixing mass flow rate due to turbulent mixing and void drift is combined modeled in the EVVD model and is assumed to be proportional to the non-equilibrium void fraction gradient. The EVVD model is widely applied in state-of-the-art subchannel analysis codes, represented by Hwang et al. [33, 34] in MATRA, Rowe et al. [70] in the modified COBRA-IIIC and Tapucu et al. [93] in ASSERT-4.

2.2.2 Equal-mass-exchange turbulent mixing incorporating void drift

In this approach, represented by the works accomplished in Kumamoto University, Japan [37, 39, 40, 72], turbulent mixing is assumed to be a phenomenon resulting in neither net mass nor net volume exchange in a time averaging aspect for both gaseous and liquid phases between interacting subchannels. Lahey et al.'s idea [47] of two-phase system approaching an equilibrium state of void fraction distribution is adopted for formulating the gaseous mass flow rate due to void drift. Accordingly, the net gaseous void drift volume flow rate over an axial (main streamwise) length of ΔZ is expressed as:

$$Q_{itoj,g} = \tilde{D}_{VD} \cdot [(\alpha_i - \alpha_j) - (\alpha_i - \alpha_j)_{EQ}] \cdot \Delta Z \quad (2.5)$$

Hence the net gaseous void drift mass flow per unit axial length is given as:

$$w_{itoj,g}^{EMVD} = \frac{Q_{itoj,g}}{\Delta Z} \cdot \rho_g = \tilde{D}_{VD} \cdot \rho_g \cdot [(\alpha_i - \alpha_j) - (\alpha_i - \alpha_j)_{EQ}] \quad (2.6)$$

where \tilde{D}_{VD} is the so-called void diffusion coefficient, related with the effective two-phase mixing velocity $(\Gamma_t/l_{mix})_{TP}$ and the gap clearance S_{ij} as [38]:

$$\tilde{D}_{VD} = \left(\frac{\Gamma_t}{l_{mix}} \right)_{TP} \cdot S_{ij} \quad (2.7)$$

The void diffusion coefficient and the void fraction distribution at equilibrium state must be experimentally determined, in order to calculate the two-phase flow redistribution due to inter-channel mixing effects¹.

2.2.3 Conclusion and discussion

As we can see from the above brief description, both EVVD and EMVD approach are based on Lahey et al.'s idea [47] of two-phase system attaining an equilibrium state, but assumptions taken for the three elemental components of interchannel mixing are quite different. Nevertheless, an effective mixing velocity or a void diffusion coefficient, which characterizes the magnitude of two-phase mixing effect, and the void fraction distribution at equilibrium state, which characterizes the final state due to two-phase mixing effect, are the two key parameters to evaluate the void drift phenomenon.

Though the EVVD model is widely used in state-of-the-art subchannel codes, a noticeable drawback must be mentioned. In the EVVD model, see Eq. 2.4, the mixing effect due to turbulent mixing and void drift is modeled in a combined manner. The same effective mixing velocity $(\Gamma_t/l_{mix})_{TP}$ is used for both turbulent mixing and void drift. However, these two mixing effects are induced by different physical mechanisms. Due to the irregular nature of turbulent fluctuations, turbulent mixing is regarded as a non-directional mixing effect, while void drift is a directional mixing effect with a prevailing direction as found in measurements [74, 79, 85] that the gaseous phase (void) has a strong affinity towards certain types of subchannel. The use of the same effective mixing velocity for two different mixing effects in the EVVD model is rather questionable. These two mixing effects are not clearly separated in the EVVD model.

¹Actually this is not sufficient to calculate the flow redistribution due to void drift, because the liquid part of the interchannel exchange is not specified. The liquid phase interchannel mixing mass flux is implicitly determined with an equal pressure gradient constraint exerted on the interacting subchannels, which is believed by the researchers of Kumamoto University to justify the neglecting of diversion cross flow. To the opinion of the present author the equal pressure gradient should be a consequence of diversion cross flow mixing effect. The neglecting of diversion cross flow might be not appropriate.

3. Assessment of two-phase interchannel mixing models in MATRA

In the present study the MATRA code is chosen for subchannel analysis. In this chapter performance of the interchannel mixing models currently available in MATRA was assessed. Two rod bundle benchmarks were chosen as experimental data base: the NUPEC BFBT benchmark [59] under BWR pressure level and the ISPRA EUROP benchmark [31] under PWR pressure level. Selected test cases from the benchmarks were recalculated with MATRA. Prior to discussions and conclusions of the subchannel analysis, the MATRA code and the available interchannel mixing models in MATRA were briefly described and summarized.

3.1 The MATRA code

MATRA is a subchannel analysis code modified based on the COBRA-IV-I code [86]. MATRA is applicable under both BWR and PWR conditions and for both steady state and transient simulations. Compared to COBRA-IV-I, MATRA has been provided with an improved code structure, various functions and models to give a more convenient user environment and to enhance prediction accuracy [107]. Among them, the improved interchannel mixing models for application under two-phase flow conditions [33] is the most worthy to be mentioned. Similar to COBRA-IV-I, a one-fluid approach is also considered to two-phase mixture in MATRA. The local composition of fluid is described by the space- and time averaged void fraction α . Any fluid parameters can be then expressed as the void fraction weighted sum of the individual single phase variables. Taken density in an arbitrary subchannel i as example:

$$\rho_i = \rho_g \cdot \alpha_i + \rho_l \cdot (1 - \alpha_i) \quad (3.1)$$

with the subscripts i and g, l denote the properties of two-phase mixture in the subchannel i , properties of the single gaseous and liquid phase, respectively. In the following subsections, conservation equations of fluid mass, energy, axial and transverse momentum established for two-phase mixture in the subchannel i will be first introduced, followed by a brief description of solution schemes and constitutive relations, which are required to close the subchannel equation system. At the end of this chapter, interchannel mixing models in MATRA will be separately discussed due to its significant impact on the prediction accuracy of subchannel analysis.

3.1.1 Subchannel conservation equations

Considering a subchannel segment with the axial (main streamwise) length of ΔX^I as illustrated in Fig. 3.1, which defines the control volume V with the axial flow area A^{II} , the axial

^IIn chapter 3 the main streamwise wise direction was set in X direction.

^{II}The axial flow area A is assumed to be constant over the axial length ΔX .

flow velocity is denoted with u . The lateral interchannel mixing is defined in the gap region between two fuel rods on an imaginary plane that separating two adjacent subchannels. The gap clearance is S , so that the lateral flow area is $(S\Delta X)$. The lateral velocity cross the gap is denoted with v . For application to LWR rod bundle benchmarks, the working fluid is con-

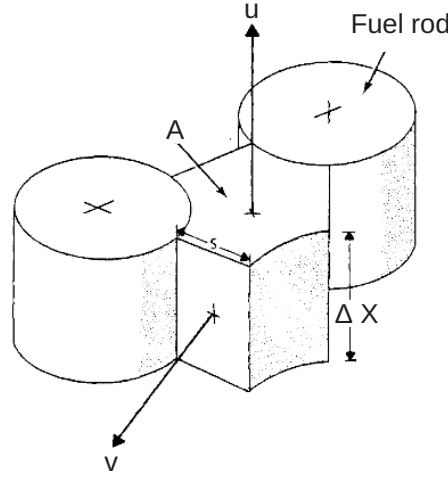


Fig. 3.1: An arbitrary subchannel control volume (taken from [86]).

sidered to be a single-component two-phase mixture¹. Before introducing the basic governing equations established for the two-phase mixture, it is necessary to define the volume and surface averaged flow parameters. Using density and axial mass flux for example, the volume averaged and surface averaged flow parameters are defined as:

$$\langle\langle \rho \rangle\rangle_V \equiv \frac{1}{V} \int_V \rho dV \quad (3.2)$$

$$\langle \rho u \rangle_A \equiv \frac{1}{A} \int_A (\rho u) dA \quad (3.3)$$

with $V = \int_V dV$ and $A = \int_A dA$. For the two-phase mixture considered it is assumed that velocities and volume fractions of each phases are uniformly distributed within the entire control volume V , so that the area averaged mass flux must be equivalent to the volume averaged mass flux in both axial and lateral directions. The axial subchannel flow rate m (dimension $kg s^{-1}$) is hence defined as:

$$m \equiv A \langle \rho u \rangle = A \langle\langle \rho u \rangle\rangle \quad (3.4)$$

The lateral mass flow is defined as a mass flow rate over a unit axial length (dimension $kg m^{-1} s^{-1}$) as:

$$w \equiv S \langle \rho v \rangle = S \langle\langle \rho v \rangle\rangle \quad (3.5)$$

Last but not least, the fluid quality transported by the lateral interchannel mixing flow is assumed to be the same as that transported axially. This allows the same definition of flowing enthalpy and quality in both axial and lateral direction. The flowing enthalpy \hat{h} is defined as:

$$\hat{h} \equiv \frac{\langle \rho u h \rangle}{\langle \rho u \rangle} = \frac{\langle \rho v h \rangle}{\langle \rho v \rangle} \quad (3.6)$$

Similarly, the flow quality x^{II} is defined as:

$$x \equiv \frac{\langle \alpha \rho_g U_g \rangle}{\langle \rho u \rangle} = \frac{\langle \alpha \rho_g V_g \rangle}{\langle \rho v \rangle} \quad (3.7)$$

¹Water is the single chemical component with two different phases: liquid and gaseous phase.

^{II}For convention the small hat \wedge is not added to the symbol denoting flow quality.

With the above definitions the continuity, energy and momentum equation for an arbitrary subchannel i laterally connected with a subchannel j can be expressed as [see 34]:

- Continuity:

$$A_i \frac{\partial \rho_i}{\partial t} + \frac{\partial m_i}{\partial X} + \sum_j w_{ij} + \sum_j (w'_{ij} - w'_{ji}) = 0 \quad (3.8)$$

- Energy:

$$A_i \frac{\partial \rho_i h_i}{\partial t} + \frac{\partial m_i \hat{h}_i}{\partial X} + \sum_j w_{ij} \hat{h}^* + \sum_j (w'_{ij} h_i' - w'_{ji} h_j') = q' \quad (3.9)$$

- Axial momentum:

$$\frac{\partial m_i}{\partial t} + \frac{\partial}{\partial X} \left[m_i \left(\frac{m_i}{\hat{\rho}_i A_i} \right) \right] + \sum_j w_{ij} u^* + \sum_j f_T (w'_{ij} u_i' - w'_{ji} u_j') = -A \frac{\partial p}{\partial X} - F_X \quad (3.10)$$

- Transverse momentum:

$$\frac{\partial w_{ij}}{\partial t} + \frac{\partial w_{ij} \bar{u}_i}{\partial X} = \frac{S_{ij}}{L_c} (\rho_i - \rho_j) - F_{ij} \quad (3.11)$$

In the continuity, energy and axial momentum equation, the first two terms on the left side stand for the transient temporal change and the spatial convective change of the respective flow parameters in subchannel i . The two-phase mixture momentum density $\hat{\rho}_i$ in the axial momentum equation is given with the flow quality x_i and the void fraction α_i of the subject subchannel i as:

$$\frac{1}{\hat{\rho}_i} = \frac{x_i^2}{\alpha_i \rho_g} + \frac{(1 - x_i)^2}{(1 - \alpha_i) \rho_l} \quad (3.12)$$

Hence the expression $(m_i / \hat{\rho}_i A_i)$ has the physical meaning of two-phase mixture momentum transport velocity. Noted that the momentum density $\hat{\rho}_i$ is different to that defined in Eq. 3.1. The third term on the left side refers to the interchannel mixing of mass, energy and axial momentum due to diversion cross flow w_{ij} , which is solved in the transverse momentum equation. Diversion cross flow is a directional interchannel mixing effect. \hat{h}^* and u^* denote the enthalpy and axial momentum that transported by diversion cross flow, respectively. The normal choices of \hat{h}^* and u^* are the corresponding values of the donor subchannel. Taken \hat{h}^* as example:

$$\hat{h}^* = \begin{cases} \hat{h}_i^* & \text{for } w_{ij} > 0 \\ \hat{h}_j^* & \text{for } w_{ij} < 0 \end{cases} \quad (3.13)$$

The last terms on the left side of the continuity, energy and axial momentum equation denote then the contribution of turbulent mixing and void drift. w'_{ij} and w'_{ji} stand for the interchannel mixing flow rate per axial length due to turbulent mixing and void drift combined from subchannel i to j and vice versa¹. Hence $(w'_{ij} - w'_{ji})$ represents the effective lateral mass flow between subchannel i and j due to turbulent mixing and void drift. Similarly, $(w'_{ij} h_i' - w'_{ji} h_j')$ and $(w'_{ij} u_i' - w'_{ji} u_j')$ are the effective enthalpy and momentum transported between subchannel i and j due to turbulent mixing and void drift, respectively. The factor f_T is used in COBRA-IV-I to correct the imperfect analogy between eddy diffusivity of heat and momentum. Since in MATRA both turbulent mixing and void drift are considered in w'_{ij} , this factor is omitted in

¹In COBRA-IV-I w' refers only to turbulent mixing, while in MATRA the void drift effect is also included [see 33].

evaluating the interchannel momentum mixing term. The heat flux on the right hand side of energy equation (Eq. 3.9) is expressed as:

$$q' = \frac{\partial}{\partial X} \left(\lambda_i A_i \frac{\partial T_i}{\partial X} \right) - \sum_j \frac{\lambda_j S_{ij}}{L_c} (T_i - T_j) + \sum_n \xi_n q_n'' \quad (3.14)$$

with three elemental terms¹ stand for the heat input into the fluid in subchannel i due to axial heat conduction, lateral heat conduction and heat input from fuel rods (indexed with n), respectively. Normally the axial and lateral heat conduction terms could be neglected, as long as the change of fluid temperature in both direction is not too large. In two-phase flows with boiling occurrence this is normally the case. Heat flux coming from fuel rods plays the dominant role regarding heat input into subchannel. The source term F_X in the axial momentum equation is expressed as:

$$F_X = A_i \rho_i g + \frac{1}{2} \left\{ \frac{f \phi^2}{\hat{\rho} D_h} + \frac{K}{\hat{\rho} \Delta X} \right\}_i \frac{m_i^2}{A_i} \quad (3.15)$$

The first term of the right hand side is the momentum flux acting on the subchannel due to gravity. The second term is a combined drag force consisting of frictional pressure drop and local pressure drop due to grid spacer with K is the dimensionless local pressure loss coefficient. The source term F_{ij} in the transverse momentum equation is expressed as:

$$F_{ij} = K_{ij} \frac{w_{ij} |w_{ij}| S_{ij}}{2 \rho^* S_{ij}^2 L_c} \quad (3.16)$$

The loss coefficient K_{ij} consists of both frictional and local form (changing of flow area due to the narrow connecting gap) pressure drop of diversion cross flow.

3.1.2 Numerical solution scheme

Two solution schemes are available in COBRA-IV-I, namely an implicit and an explicit scheme. While the implicit scheme is only applicable for steady state or slow transient simulations due to its restriction to cases where the axial (main streamwise) flow rates are positive and considerably larger than the lateral interchannel mixing flows, the explicit solution scheme removes the restriction of positive axial flows and is also applicable to fast transient cases. However, the explicit scheme currently uses only homogeneous equilibrium models for describing two-phase flow properties. The two-phase slip model along with the two-phase friction multiplier model (see detailed descriptions in chapter 3.1.3) are not available in the explicit solution. The explicit solution scheme of COBRA-IV-I was not rechecked while developing the MATRA code [see 43]. Furthermore, in the current study for simulation of two-phase flow behavior in rod bundle geometry the implicit solution scheme was employed exclusively. Hence here only the implicit solution scheme in MATRA will be briefly introduced. Detailed information can be found in [86, 107].

The overall solution scheme consists of three iterative solutions: an external iterative channel sweep of the computational domain from the inlet boundary to the outlet boundary and a separate internal loop for enthalpy and diversion cross flow, respectively. In the external sweep the local flow parameters: enthalpy h_J , density ρ_J , diversion cross flow rate w_J , axial flow rate m_J and pressure p_J are updated at each axial level J in turn. This involves the two internal iterative solutions of the enthalpies in all subchannels and the diversion cross flows in all gaps at

¹Work done by shear stress and body force is considered to be insignificant and hence neglected in the energy equation. Furthermore, the case with heat input from heat conducting wall is not considered.

each axial level, respectively. The external iteration is considered to be converged if the maximum change in diversion cross flow and in axial flow is simultaneously less than the specified input value between successive external iteration steps. A further termination criterion is specified after reaching a maximum number of external iterations, even if the convergence criteria are still not satisfied. The convergence criteria for the two internal iterations are similarly defined, however the external solution is allowed to continue regardless of whether convergence is established or not.

For the inlet boundary, distribution of axial flow rate and enthalpy in all channels are specified, as well as a zero inlet diversion cross flow condition. Constant static pressure (zero lateral pressure difference) condition is specified at the outlet boundary. Since the subchannels are laterally connected with each other, no further lateral boundary conditions are required. On solid fuel rod and heat conducting wall, a thermal boundary condition is provided by heat condition model (fuel model and wall model) for the energy equation. In case that no heat conduction model is employed, the thermal boundary condition is then provided directly via input surface heat flux.

For steady state simulations, initial estimation of enthalpy, diversion cross flow and axial flow required for the current axial level J are defined as values of the previous axial level $J - 1$, if J is larger than 2. For J equal to 1, namely the first axial level, these flow parameters are defined as input boundary. The subchannel pressures are calculated after updating enthalpy and flow rate. Lateral pressure difference between adjacent subchannels is required for solving the transverse momentum equation, for which initial estimation is defined as zero. In transient cases, initial guess of flow parameters are taken as those calculated in the previous time step.

For solving the conservation equations, time and spatial derivative terms in the equations are discretized with a finite difference scheme. Furthermore, two matrix operators are introduced with respect to the hydraulic connection of the adjacent channels and with respect to the thermal connection of the channels with fuel rods (if necessary, also with heat conducting solid walls), respectively. With the connection matrices all the important flow parameters of each channels at a given axial levels J are interrelated and hence must be solved simultaneously before proceeding to the next level $J + 1$. This is done in two steps which requires firstly the iterative solution of the energy equation and in the second step the iterative solution of the combined axial and transverse momentum equation.

The overall implicit solution scheme is schematically depicted in a flow chart diagram shown in Fig. 3.2. Previous to each external channel sweep indexed with N , in order to obtain temperature distribution in fuel rod T_{rod} and heat flux into fluid in subchannel q'' , heat conduction fuel model is solved iteratively for the entire fuel structure using surface heat transfer coefficient H_{surf} and subchannel fluid temperature obtained in the preceding ($N - 1$) iteration. At the first external iteration step ($N = 1$), this information is not yet available hence the fuel model calculation is bypassed. The average surface heat flux specified as input value serves directly as thermal boundary condition to the fluid energy equation. Beginning from the second external iteration step ($N = 2$) the fuel model provides the fuel surface temperature, which is used along with the surface heat transfer coefficient to calculate the heat flux input to the fluid in subchannel.

The first operation at each axial level J in the external channel sweep is the iterative solving of the combined fluid energy and wall heat conduction equation, which provides wall temperature T_W and fluid enthalpy h_J in all subchannels at the current calculation axial level. With the updated fluid enthalpy via the equation of state, the fluid density ρ_J , fluid temperature in subchannel T_F as well as other physical properties are updated. These are used to obtain the coefficients and source terms for iterative solution of the axial and transverse momentum

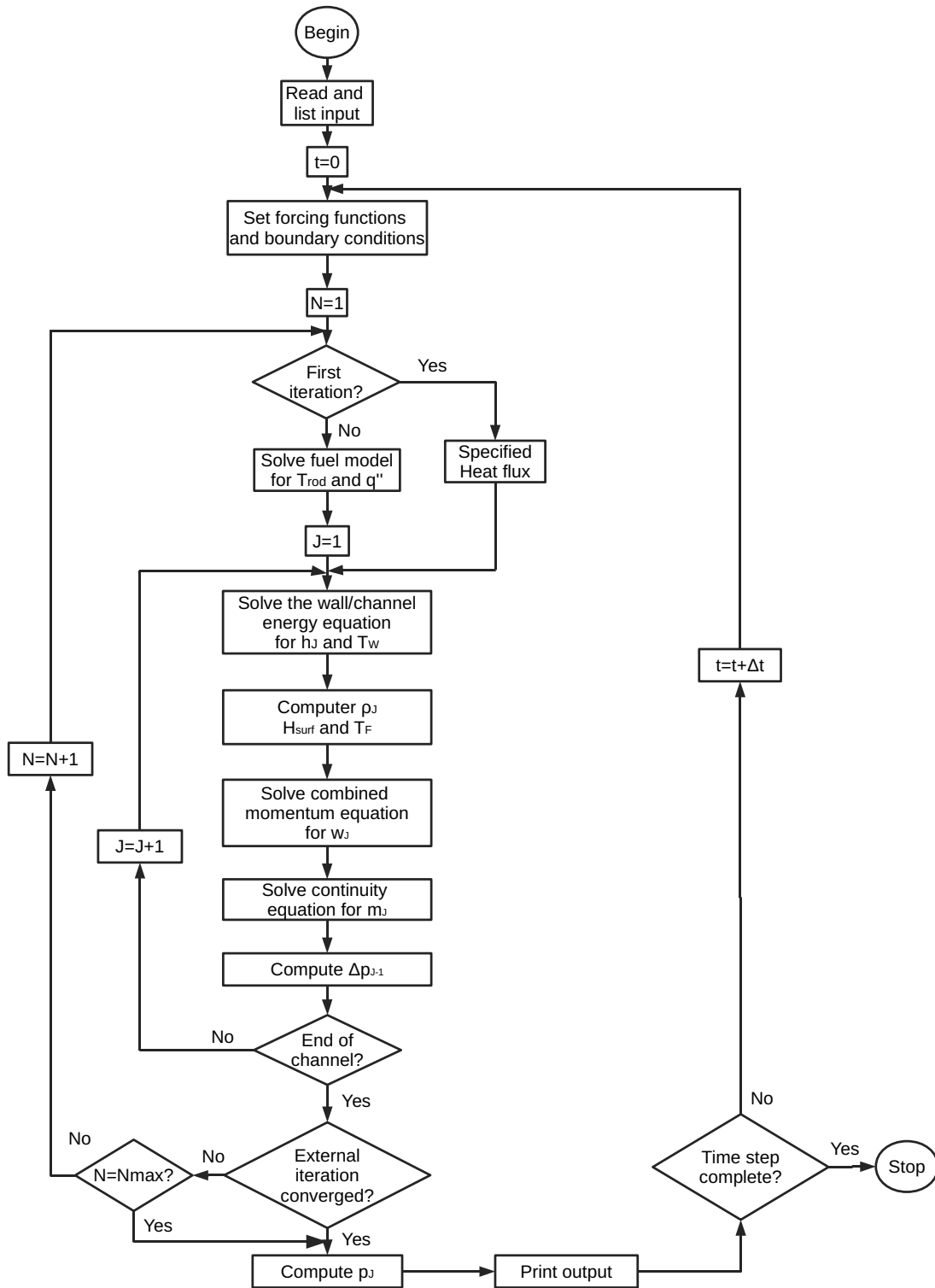


Fig. 3.2: Flow chart diagram of the implicit solution scheme in MATRA.

equation in a combined manner. Also at this time, the new surface heat transfer coefficients H_{surf} are evaluated for solving the fuel model in the next $(N+1)$ external iteration. The diversion cross flow at the current axial level w_J is then obtained by solving the combined momentum equation, where the values of the lateral subchannel pressure difference are taken from the preceding external iteration $N-1$. The updated diversion cross flows and the new fluid density are used in the continuity equation along with the axial mass flow rate of the preceding axial level $J-1$ to calculate the axial mass flow rates of the current axial level m_J . This completes

the updating of all the flow parameters at the current calculation level J . Before continuing the channel sweep to the next axial level $J + 1$, the axial momentum equation is solved using the new diversion cross flow rate to provide new estimation of the lateral pressure difference between subchannels at the preceding axial level Δp_{J-1} for use in the next $(N + 1)$ external iteration step. After finishing updating the flow parameters of all axial levels, the convergence criteria of the external solution loop are checked, in order to justify whether a new external channel sweep is required. If it is not the case, all the channel results will be printed out. In case a further external iteration step is necessary, the iteration index N will be increased to $N + 1$ and the same procedure as described above from inlet to the outlet boundary will be repeated.

3.1.3 Constitutive relations in MATRA

Along with the four conservation equations described in chapter 3.1.1, an equation of state calculating physical properties of the two-phase mixture and a heat conduction equation describing the heat conduction between fuel rods/heat conducting walls and fluid build up a system of six equations, which is sufficient to solve the six dependent variables of fluid density, enthalpy, axial flow rate, diversion cross flow rate, pressure and fuel temperature. However, constitutive relations are required to supply information on surface heat transfer coefficients, friction factors, phase slip ratio, i.e. quality-void relation and interchannel mixing effect due to turbulent mixing as well as void drift. The formation of the equation of state and the constitutive relations will be briefly discussed in the current chapter. Due to its importance on the predicted phase and enthalpy distribution in subchannels, interchannel mixing models in MATRA will be detailed described in the subsequent chapter.

Equation of state

MATRA is applicable for single phase liquids, single phase gases and two-phase mixtures. In this manner, no single equation or correlation for property calculation is able to cover the whole range of applications. A separate procedure is used for each of the three states. All fluid properties in COBRA-IV-I are calculated using the concept of a reference pressure, which is specified at the outlet boundary as input value and applied uniformly over the entire computational domain. Using the reference pressure the saturation properties are obtained, with which the current fluid state, namely subcooled liquid, two-phase mixture or superheated gas, can be identified. This global reference pressure approach neglects the influence of local dynamic and hydrostatic pressure head [86] and is justifiable if the maximum spatial pressure change is considerable small than the reference pressure. For application at very high pressure levels, such as that under typical BWR and PWR working conditions, the global reference pressure approach can be regarded as reasonable, since the axial pressure drop over the rod bundle is negligibly small compared to the reference pressure level of about 70 bar and 160 bar, respectively. However, for application under low pressure conditions the local pressure drop effect on the fluid properties can be considerable large. Therefore, in MATRA the reference pressure for calculating fluid properties can be switched from the global exit pressure to local pressure at each axial levels [see 107].

In COBRA-IV-I properties of the subcooled liquid phase are assumed to follow the saturation liquid line and hence calculated by linear interpolation using the saturation properties supplied by the users as input in a tabular form. In this manner, accuracy of the calculated properties is dependent on the input and may lead to considerable errors, if the saturation property table is poorly provided by the user. Therefore, a new subroutine "TAF" [see 107] is implemented to MATRA to calculate the subcooled properties directly by referencing to the

function “TAF”, which improves the accuracy of the calculated subcooled fluid properties. In the two-phase region, density and enthalpy are related with quality-void functions, while the rest of the properties remain at the saturated liquid values. Since physical properties of the superheated gases were not required in the current study, description of calculating superheated gaseous properties is skipped and referred to literature [86].

Heat transfer coefficient

With the heat transfer coefficient, thermal-hydraulic parameters in subchannels are interfaced with the fuel model/wall model. In a single phase flow, the heat transfer coefficient H_{surf} is correlated with the Reynolds number Re and the Prandtl number Pr :

$$H_{surf} = \frac{\lambda_l}{D_h} \cdot (aRe^b Pr^c + d) \quad (3.17)$$

with λ_l is the fluid thermal conductivity and D_h the subchannel hydraulic diameter. The empirical constants a through d are either input by user or by default set as the respective values of: 0.023, 0.8, 0.4 and 0 to form the Dittus-Boelter equation [22] as:

$$Nu = 0.023Re^{0.8} Pr^{0.4} \quad (3.18)$$

with the Nusselt number defined as $Nu = (H_{surf} \cdot D_h) / \lambda_l$.

For steam-water two-phase applications, a complete package of heat transfer coefficients under non-boiling and boiling conditions is implemented in MATRA. Seven regimes are considered: forced convection, subcooled and nucleate boiling, forced convective vaporization, transition boiling, transition pool boiling, film boiling and pool film boiling. The selection of appropriate correlations is done fully implicitly by the code. Since heat transfer coefficient is not the subject of the current study, detailed description is skipped and referred to literature [58, 86].

Friction factor and local pressure loss coefficient

Frictional pressure drop due to wall shear stress over an axial (main streamwise) increment of ΔX is given by the expression:

$$\Delta p_f = f \cdot \frac{\Delta X}{D_h} \frac{G^2}{2\rho} \quad (3.19)$$

with f is the dimensionless friction factor, G the axial mass flux. Local axial form pressure drop due to flow obstructions such as grid spacers is taken into account by a local pressure loss coefficient K with the following expression:

$$\Delta p_K = K \cdot \frac{G^2}{2\rho} \quad (3.20)$$

Due to the complex geometry in a gap, lateral pressure drop is not determined separately. Instead, the lateral frictional pressure drop is merged with the local form pressure loss due to change of area in the gap region by a constant lateral pressure drop coefficients K_G with the following expression:

$$\Delta p_{ij} = p_i - p_j = K_G \cdot \frac{w_{ij}^2}{2\rho^* \cdot S_{ij}^2} \quad (3.21)$$

with Δp_{ij} represents the lateral pressure difference between two interacting subchannels i and j connected with a gap clearance of S_{ij} . w_{ij} is the diversion cross flow per unit axial length

cross the gap and ρ^* is taken as density of the donor subchannel [47]. Strictly speaking, an individual proportional factor K_{ij} should be used for each connecting gap. This leads however to enormous numerical efforts. Generally a constant factor K_G is applied uniformly to the whole rod bundle. For a typical rod bundle geometry, the value of K_G is in the order of 0.5 [see 86, 90].

For single phase flows, Eq. 3.19, 3.20 and 3.21 apply directly. The friction factor f in Eq. 3.19 is related with the Reynolds number by this manner:

$$f = a \cdot Re^b + c \quad (3.22)$$

with the empirical factors a , b and c are taken the following values depending on the Reynolds number as recommended in [43]:

$$\begin{cases} a = 0.316 \\ b = -0.25 \\ c = 0 \end{cases} \quad \text{for } 5000 < Re < 30000 \quad (3.23)$$

$$\begin{cases} a = 0.184 \\ b = -0.20 \\ c = 0 \end{cases} \quad \text{for } 30000 < Re < 1000000 \quad (3.24)$$

For a given mass flux, pressure drop in a two-phase system can be much greater than that in a corresponding single phase system. The two-phase axial frictional pressure drop is related with the equivalent single liquid phase pressure drop by introducing a two-phase friction multiplier Φ^2 as:

$$\Phi^2 = \frac{\Delta p_{f,TP}}{\Delta p_{f,SP}} \quad (3.25)$$

with the subscripts TP and SP stand for two-phase and single phase flow, respectively. The choice of liquid as the base phase is reasonable in applications in nuclear reactors. In order to obtain the two-phase frictional pressure drop, the single liquid phase frictional pressure drop $\Delta p_{f,SP}$ is firstly calculated with Eq. 3.19 and the single phase friction factor f_{SP} specified in Eq. 3.23 or 3.24 as:

$$\Delta p_{f,SP} = f_{SP} \cdot \frac{\Delta X G^2}{D_h 2\rho_l} \quad (3.26)$$

with ρ_l the density of the liquid phase. Therefore, the two-phase frictional pressure drop can be expressed as:

$$\Delta p_{f,TP} = \Phi^2 \cdot f_{SP} \cdot \frac{\Delta X G^2}{D_h 2\rho_l} \quad (3.27)$$

The two-phase friction multiplier Φ^2 may be specified with different types of models: the homogeneous model, the Armand model [see 86] or as a polynomial function of flow quality. In the homogeneous model, Φ^2 is simply defined as a ratio of the liquid phase density to that of the two-phase mixture:

$$\Phi^2 = \frac{\rho_l}{\rho_m} \quad (3.28)$$

with the subscript m stands for the physical properties of the two-phase mixture. In the Armand model, Φ^2 is defined as a function of flow quality and void fraction as follows:

$$\Phi^2 = \begin{cases} \frac{(1-x)}{(1-\alpha)^{1.42}} & \text{for } 0.0 < \alpha \leq 0.4 \\ 0.478 \frac{(1-x)^2}{(1-\alpha)^{2.2}} & \text{for } 0.4 < \alpha \leq 0.9 \\ 1.73 \frac{(1-x)^2}{(1-\alpha)^{1.64}} & \text{for } 0.9 < \alpha \leq 1.0 \end{cases} \quad (3.29)$$

The polynomial function uses up to seven input coefficients to express Φ^2 as a function of flow quality as:

$$\Phi^2 = a_0 + a_1 \cdot x + a_2 \cdot x^2 + a_3 \cdot x^3 + a_4 \cdot x^4 + a_5 \cdot x^5 + a_6 \cdot x^6 \quad (3.30)$$

Quality-void relations

Flow quality x defined in Eq. 3.7 can be written as:

$$x = \frac{\rho_g u_g A_g}{\rho_g u_g A_g + \rho_l u_l A_l} \quad (3.31)$$

with u_g and u_l the velocity of gaseous and liquid phase, respectively. A_g and A_l are the subchannel cross section areas occupied by gaseous and liquid phase, respectively. The velocity ratio is defined as slip ratio s :

$$s = \frac{u_g}{u_l} \quad (3.32)$$

Flow quality x is the true mass fraction of vapor in a two-phase system regardless of whether thermodynamic equilibrium is established or not. Hence it is also referred to in COBRA-IV-I and MATRA as the true quality x_t . With the definition of α , x and s , the fundamental quality-void relation yields:

$$\frac{x}{(1-x)} = \frac{\rho_g}{\rho_l} \cdot s \cdot \frac{\alpha}{(1-\alpha)} \quad (3.33)$$

This equation can be used to evaluate the void fraction with the flow quality x , once the slip ratio s is known:

$$\alpha = \frac{x}{x + \frac{\rho_g}{\rho_l} \cdot s \cdot (1-x)} \quad (3.34)$$

Several quality-void relations are available in MATRA: the homogeneous model, the slip model, the modified Armand model [see 86], the Chexal-Lellouche model [17] and the polynomial model. In the homogeneous model, the slip ratio s is assumed equal to unity, so that the void fraction can be directly obtained as:

$$\alpha = \frac{x}{x + \frac{\rho_g}{\rho_l} \cdot (1-x)} \quad (3.35)$$

In the slip model the slip ratio is directly input as a constant by the user. For upward two-phase flow as encountered in nuclear fuel assemblies, s should be larger than unity. In the modified Armand model the void fraction is expressed as:

$$\alpha = \frac{(0.833 + 0.167x) \cdot x}{x + \frac{\rho_g}{\rho_l} \cdot (1-x)} \quad (3.36)$$

Due to its wide applicable range of thermal-hydraulic conditions and geometries of typical BWR and PWR fuel assemblies, the Chexal-Lellouche model, which is not available in COBRA-IV-I, is also implemented in MATRA. The correlation is based on the drift flux model and determines the drift flux parameters, concentration parameter and drift velocity for evaluating void fraction. Detailed description is referred to literature [17]. Finally in the polynomial option, void fraction may be specified as a polynomial function up to six order of flow quality with a_0 to a_6 as input constants:

$$\alpha = a_0 + a_1 \cdot x + a_2 \cdot x^2 + a_3 \cdot x^3 + a_4 \cdot x^4 + a_5 \cdot x^5 + a_6 \cdot x^6 \quad (3.37)$$

In the above quality-void relations, flow quality x is always required to determine void fraction. However, the flow quality is not readily available. By solving the energy equation as described in the implicit solution scheme, enthalpy of the two-phase mixture h_m can be obtained, with which an equilibrium quality x_{eq} can be obtained from:

$$x_{eq} = \frac{h_m - h_{ls}}{h_{lg}} \quad (3.38)$$

h_{ls} and h_{lg} stand for the saturated liquid phase enthalpy and the latent heat at the reference pressure, respectively. Once thermodynamic equilibrium is established in the two-phase system, namely in the saturated boiling range, the flow quality x has the same value as the equilibrium quality x_{eq} . However, in the subcooled boiling range, where the bulk fluid is still subcooled ($x_{eq} < 0$) but near heated solid surface considerable void may have been generated, the flow quality x is clearly larger than zero. For application in the subcooled boiling range, the subcooled boiling model proposed by Levy [52] is applied in MATRA. The flow quality x is correlated in terms of the equilibrium quality x_{eq} and the quality x_{OSV} , at which bubble departure from heated wall begins, i.e. onset of significant void fraction, by the expression:

$$x = x_{eq} - x_{OSV} \cdot e^{x_{eq}/x_{OSV}-1} \quad \text{for } x_{eq} > x_{OSV} \quad (3.39)$$

where x_{OSV} is defined as:

$$x_{OSV} = \frac{-c_p \cdot \Delta T_d}{h_{lg}} \quad (3.40)$$

ΔT_d is the saturation temperature minus the bulk fluid temperature at the point of bubble departure from the heated wall. It is a function of surface heat flux, friction factor, mass flux and surface tension. Detailed formulation is referred to literature [52]. In case of x_{eq} smaller than x_{OSV} , the flow quality x is simply set as zero. Under this condition, the generated void bubbles will be recondensed before they are able to leave the heated wall and void fraction in the entire system is negligibly small.

3.2 Interchannel mixing models in MATRA

The mixing effect due to diversion cross flow is related with the radial pressure gradient of adjacent subchannels by the lateral resistance coefficient K_G as expressed in Eq. 3.21. The proportional factor K_G is by default 0.5 [43] for rod bundle geometry. Diversion cross flow is directly solved in the transverse momentum equations (Eq. 3.11), hence no additional model is required. The interchannel mixing model in MATRA (subroutine "MIX") evaluates only the mixing effect due to turbulent mixing and void drift. Two types of models can be distinguished, depending on whether void drift is considered or not:

- Equal-mass-exchange turbulent mixing (EM) model without void drift
- Equal-volume-exchange turbulent mixing with void drift (EVVD) model

3.2.1 EM model

By introducing the turbulent mixing coefficient β , turbulent mixing mass flow rate per axial (main streamwise) length from an arbitrary subchannel i to its neighboring subchannel j is related to the axial average mass flux of the two interacting subchannels as:

$$w'_{ij} = \beta \cdot S_{ij} \cdot G_{avg} \quad (3.41)$$

with S_{ij} is the gap clearance and the subscript *avg* denotes the average value of the two connecting subchannels. In the EM model, it is assumed that the same amount of fluid mass is exchanged between the two interacting subchannels:

$$w'_{ij} = w'_{ji} = w'_{EM} \quad (3.42)$$

Hence, the time averaged net turbulent mixing mass flow from subchannel i to j , denoted with w'_{itoj} , is zero:

$$w'_{itoj} = w'_{ij} - w'_{ji} = 0 \quad (3.43)$$

Despite the zero net interchannel mass flow, a net enthalpy or momentum interchannel flow exist due to possible differences in enthalpy or velocity filed between the two interacting subchannels. In the EM model, the net enthalpy and momentum interchannel flow are expressed as follows¹:

$$(w'_{ij}h'_i - w'_{ji}h'_j) = w'_{EM} \cdot (\hat{h}_i - \hat{h}_j) \quad (3.44)$$

$$(w'_{ij}u'_i - w'_{ji}u'_j) = w'_{EM} \cdot \left(\frac{m_i}{\hat{\rho}_i A_i} - \frac{m_j}{\hat{\rho}_j A_j} \right) \quad (3.45)$$

The EM model is good applicable under single phase flow conditions. The single phase turbulent mixing coefficient β_{SP} is normally determined from thermal mixing tests under single phase conditions [see 33]. In MATRA β_{SP} can be simply assumed as a constant value. Based on application to various PWR test bundles without mixing vanes, Hwang et al. [see 33] determined β_{SP} as a constant value of 0.005. By evaluating results obtained with rod bundle tests, Lahey et al. [48] found out that the best overall agreement with single phase measurement results could be obtained with β_{SP} of 0.005. Besides direct input as a constant value, the following possibilities of correlating β_{SP} with the Reynolds number or/and geometrical parameters are also available in MATRA:

$$\beta_{SP} = a \cdot Re_{avg}^b \quad (3.46)$$

$$\beta_{SP} = a \cdot Re_{avg}^b \cdot \frac{D_{h,avg}}{S} \quad (3.47)$$

$$\beta_{SP} = a \cdot Re_{avg}^b \cdot \frac{D_{h,avg}}{L_C} \quad (3.48)$$

where a and b are both input constants, Re_{avg} the average Reynolds number, $D_{h,avg}$ the average hydraulic diameter and L_C the centroid-to-centroid distance of the two interacting subchannels.

Under two-phase flow conditions, a two-phase turbulent mixing multiplier θ proposed by Beus [9] is applied, so that the two-phase turbulent mixing mass flow rate per axial length from subchannel i to j is given as:

$$w'_{ijTP} = \theta \cdot w'_{EM,SP} = \theta \cdot \beta_{SP} \cdot S_{ij} \cdot G_{avg} \quad (3.49)$$

The two-phase turbulent mixing multiplier θ is flow regime dependent:

$$\theta = 1 + (\theta_M - 1) \cdot \frac{X_{avg}}{X_C} \quad \text{for bubbly-slug flow regime } X_{avg} < X_C \quad (3.50)$$

$$\theta = 1 + (\theta_M - 1) \cdot \frac{1 - \frac{X_0}{X_C}}{\frac{X}{X_C} - \frac{X_0}{X_C}} \quad \text{for annular flow regime } X_{avg} > X_C \quad (3.51)$$

where the parameters are:

¹The laterally transported h'_k and u'_k simply take the values of the corresponding flow parameters from its origin subchannel with $k = i$ or j .

- $\theta_M = 5$
- x_{avg} : the average flow quality of the two interacting sub channels
- x_C : the slug-annular transition flow quality determined as:

$$x_C = \frac{0.4 \cdot \frac{\sqrt{g \cdot D_h \cdot \rho_l \cdot (\rho_l - \rho_g)}}{G_{avg}} + 0.6}{\sqrt{\frac{\rho_l}{\rho_g}} + 0.6} \quad (3.52)$$

- $\frac{x_0}{x_C}$ is calculated as a function of the Reynolds number:

$$\frac{x_0}{x_C} = 0.57 \cdot Re_{avg}^{0.0417} \quad (3.53)$$

3.2.2 EVVD model

Under two-phase flow conditions, a substantial amount of net mass exchange has been experimentally observed as well as a tendency of two-phase system approaching an equilibrium state of phase distribution [see 29, 85]. The gaseous phase has apparently a strong affinity towards certain types of subchannel, which is referred to as void drift according to Lahey et al. [48]. Based on experimental studies, Lahey and Moody [47] developed a phenomenological model, which incorporates the effect of void drift to turbulent mixing. It hypothesizes that the net two phase interchannel mixing flow rate per axial length due to turbulent mixing and void drift from subchannel i to j is proportional to the non-equilibrium void fraction gradient:

$$(w'_{itoj})^{EVVD} = w'_{ij} - w'_{ji} \propto [(\alpha_j - \alpha_i) - (\alpha_j - \alpha_i)_{EQ}] \quad (3.54)$$

This model implies a tendency towards the equilibrium state of void fraction distribution $(\alpha_j - \alpha_i)_{EQ}$. Once this state is achieved, net exchange due to mixing ceases. This model combines the equal volume (EV) exchange turbulent mixing and the effect of the void drift (VD) phenomena, hence is also known as the EVVD model. By adopting a simple model proposed by Levy [51], the void fraction distribution at equilibrium state is assumed to be linearly proportional to the mass flux distribution in the two interacting subchannels. Since Levy's assumption is not well validated and has been disapproved by the measurement of Sadatomi et al. [72, 73], an empirically determined dimensionless void drift correction factor K_{VD} is introduced in MATRA by Hwang et al. [33] to improve Levy's model:

$$(\alpha_j - \alpha_i)_{EQ} = K_{VD} \frac{(G_j - G_i)}{G_{avg}} \quad (3.55)$$

With Eq. 3.55, $(w'_{itoj})^{EVVD}$ is expressed as:

$$(w'_{itoj})^{EVVD} = (\beta_{SP} \cdot S \cdot G_{avg}) \cdot \theta \cdot \left[(\alpha_j - \alpha_i) - K_{VD} \frac{(G_j - G_i)}{G_{avg}} \right] \quad (3.56)$$

Currently, two different types of model for evaluating the void drift correction factor K_{VD} are available in MATRA [see 34]:

- Type I: K_{VD} is simply taken as constant, for instance $K_{VD} = 1.4$ similar to that introduced in THERMIT-2 code [42].

- Type II: K_{VD} is recalculated as a function dependent on system pressure and flow regime derived from assessment of experimental data obtained in rod bundle benchmarks. Detailed derivation can be found in [33]. Accordingly, K_{VD} is expressed as:

$$K_{VD} = a_1 \left(\frac{x_{avg} - x_{OSV}}{x_C - x_{OSV}} \right) \quad \text{for bubbly-slug flow regime} \quad (3.57)$$

$$K_{VD} = a_1 + a_2 \left(\frac{x_{avg} - x_{OSV}}{x_C - x_{OSV}} - 1 \right) \quad \text{for annular flow regime} \quad (3.58)$$

where the two parameters a_1 and a_2 are:

$$a_1 = 0.72 \left(\frac{1 - p_r}{p_r} \right)^{1.33} \quad (3.59)$$

$$a_2 = 10 \quad (3.60)$$

p_r stands for the reduced pressure, which is defined as system pressure divided by the critical pressure.

The interchannel energy and momentum exchange in the EVVD model are expressed as follows:

$$(w'_{ij} h'_i - w'_{ji} h'_j) = (w'_{itoj})^{EVVD} \cdot \frac{\rho_l h_l - \rho_g h_g}{\rho_l - \rho_g} \quad (3.61)$$

$$(w'_{ij} u'_i - w'_{ji} u'_j) = (w'_{itoj})^{EVVD} \cdot \left(\frac{G_{avg}}{\rho_l - \rho_{avg}} \right) \quad (3.62)$$

3.3 Assessment of the interchannel mixing models in MATRA

Assessment of the interchannel mixing models currently available in MATRA was performed by recalculating selected rod bundle test cases conducted under both BWR and PWR working conditions. Results and conclusions will be discussed in this chapter.

3.3.1 NUPEC BFBT benchmark

The NUPEC BFBT (BWR Full-size fine-mesh Bundle Test) benchmark [59] is a high-resolution and full-scale experimental data base on subchannel wise void fraction distribution under actual BWR operation conditions. “Full-size” refers to the 8×8 square rod bundle used in the benchmark tests, which is the same size as a real BWR fuel rod bundle. The effect of water channels in BWR fuel assembly was simulated by unheated water rods. “Fine-mesh” refers to the measurement resolution of the x-ray CT detectors, which were employed in the void distribution test to measure the void fraction distribution 50 mm above the exit of the heated zones with a spatial resolution as small as 0.3 mm×0.3 mm. The subchannel average exit void fraction was then averaged over more than 400 pixel elements and the bundle average exit void fraction over more than 10⁵ pixel elements. The accuracy of the subchannel void fraction and bundle average void fraction measurement by the x-ray CT scanner was estimated to be 3% and 2% [59], respectively.

The heated length of the rod bundle was 3708 mm, which was supported by seven equally spaced simple grid spacer without mixing vanes. The outer diameter of a simulated fuel rod was 12.3 mm and the pitch distance was 16.2 mm (pitch to diameter ratio 1.317). Different types of fuel assembly geometries and power profiles were used in the void distribution test.

The assembly type 0 had uniform axial and radial power distribution. Three sub-assembly types, 0-1, 0-2 and 0-3 with two unheated water rods and varying number of unheated fuel rods, were used to investigate the effects of inhomogeneous radial power distribution on the subchannel wise void fraction distribution. The assembly types 1, 2 and 3 were of the same geometry as assembly 0 with two unheated water rods but with inhomogeneous axial and radial heat profiles. The assembly 4 with only one water rod in the center of the rod bundle had uniform axial heat profile but the same inhomogeneous radial power profile as the assemblies 1, 2 and 3. Fig. 3.3 summaries the assembly layout and power distribution profiles for the void distribution tests.

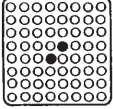
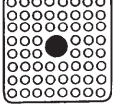
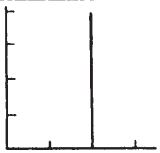
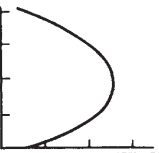
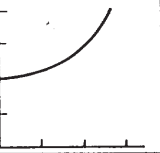

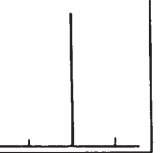
Test assembly No.	0	1	2	3	4
Fuel Type		Current use 8x8 			High burnup 8x8 
Planar power profile	Uniform	Simulated design profile	Simulated design profile	Simulated design profile	Simulated design profile
Axial power profile	Uniform	Cosine	Half-cosine	Inlet peak	Uniform
Heated length	Full	Full	Half	Full	Full
Axial power distribution Axial Power					

Fig. 3.3: Test assemblies and power distribution profiles of void distribution tests in the BFBT benchmark [59].

For the purpose of assessing interchannel models, test cases with the assembly 0, 1 and 4 were selected for recalculation with MATRA. 30 test cases with exit pressure of 70 bar (BWR pressure level), bundle average mass flux of $1500 \text{ kgm}^{-2}\text{s}^{-1}$ and six different bundle average exit qualities x_b^{ex} of 2%, 5%, 8%, 12%, 18% and 25%, were recalculated. The experimental conditions of the selected test cases are summarized in Tab. 3.1 (x_b^{ex} is given as "Exit Quality").

Due to the one-fluid approach used in MATRA, void fraction is not directly solved but correlated with flow quality via empirical quality-void relations. Prior to the assessment of interchannel mixing models, performance of the available quality-void relations in MATRA should be assessed. This was done in the current study by evaluating prediction accuracy of the bundle average void fraction with various quality-void relations. The test cases in Tab. 3.1 were recalculated with MATRA. Relevant constitutive models for this study are summarized in Tab. 3.2. The hydraulic resistance was calculated in the pressure drop models, which take into account the turbulent friction with the solid rod surface and the local form pressure drop due to grid spacers. The spacer pressure loss coefficient was reported to be 1.2 [59]. For diversion cross flow a constant transverse resistance coefficient K_G of 0.5 was used in the current study. For discussing the bundle average flow parameters, the equal-mass-exchange turbulent mixing (EM) model was used exclusively as interchannel mixing model for all the test cases, since interchannel mixing model has negligible small influence on the bundle average values. The single phase turbulent mixing coefficient β_{SP} was set as 0.005, while the Beus two-phase turbulent mixing coefficient multiplier was applied for two-phase cases. Void fraction in the subcooled boiling stage was considered with Levy's model [52], while for the

Tab. 3.1: Experimental conditions of BFBT test cases recalculated with MATRA

Case No.	Assembly	Pressure	Flow Rate	Inlet Sub-cooling	Exit Quality	Power
[–]	[–]	[MPa]	[t/h]	[kJ/kg]	[%]	[MW]
0011-53	0-1	7.18	54.47	51.5	2	1.24
0011-55	0-1	7.18	54.03	52.6	5	1.9
0011-56	0-1	7.168	54.83	51.6	8	2.57
0011-58	0-1	7.172	54.9	51	12	3.51
0011-59	0-1	7.189	54.96	50.2	18	4.87
0011-61	0-1	7.21	54.79	50.9	25	6.44
0021-15	0-2	7.163	54.73	52.3	2	1.23
0021-16	0-2	7.19	54.85	54	5	1.91
0021-17	0-2	7.165	54.83	51.1	8	2.59
0021-18	0-2	7.171	54.9	49.8	12	3.51
0021-19	0-2	7.167	54.9	49.4	18	4.86
0021-21	0-2	7.179	54.9	51.4	25	6.45
0031-15	0-3	7.17	54.97	52.3	2	1.23
0031-16	0-3	7.18	54.96	52.4	5	1.92
0031-17	0-3	7.16	54.78	50.5	8	2.59
0031-18	0-3	7.179	54.79	50	12	3.52
0031-19	0-3	7.168	54.83	50.8	18	4.88
0031-21	0-3	7.171	54.9	49.4	25	6.45
1071-53	1	7.185	54.58	52.2	2	1.23
1071-55	1	7.191	54.61	52.8	5	1.92
1071-56	1	7.203	54.64	54	8	2.6
1071-58	1	7.158	55.07	50.3	12	3.52
1071-59	1	7.177	54.74	51.3	18	4.88
1071-61	1	7.2	54.65	51.8	25	6.48
4101-53	4	7.181	54.65	52.8	2	1.24
4101-55	4	7.195	54.59	52.9	5	1.92
4101-56	4	7.175	54.62	51.8	8	2.59
4101-58	4	7.152	54.58	50.6	12	3.52
4101-59	4	7.19	54.57	52.1	18	4.88
4101-61	4	7.18	54.65	52.5	25	6.48

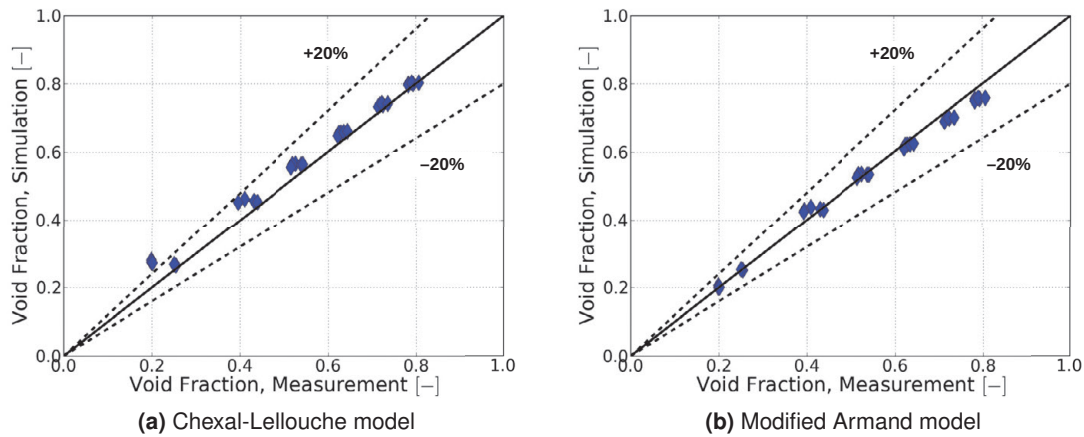
saturated boiling range two variates of models were tested in the current study: the modified Armand model and the Chexal-Lellouche model.

In Fig. 3.4 the calculated bundle exit void fractions are plotted against the corresponding measured values. The two dashed lines in both subfigures indicate +20% and –20% relative deviation, respectively. While the Chexal-Lellouche model tends to give better prediction in the high void fraction range than the modified Armand model, it generally overpredicts the void fraction in the low void fraction range. In contrast, the modified Armand model has a better performance in the low void fraction range. Despite slight underprediction in the high void fraction range, the modified Armand model shows in the whole void fraction range good performance hence was chosen as the standard quality-void correlation henceforth.

Now the prediction of subchannel average void fraction distribution will be discussed. For recalculation of the 30 test cases in Tab. 3.1 all the pressure drop models in Tab. 3.2 applied further. For the saturated boiling void fraction only the modified Armand model was used. In Fig. 3.5 the calculated subchannel average exit void fractions are plotted with two different interchannel mixing models: the EM model and the EVVD model (Type II, K_{VD} is recalculated

Tab. 3.2: MATRA models used for recalculation of BFBT test cases: assessment of the quality-void relations

Pressure drop models	
Single phase turbulent friction factor	$0.184 \cdot Re^{-0.2}$
Two-phase friction multiplier	Armand model [see 86]
Grid spacer pressure lost factor	1.2
Interchannel mixing models	
Diversion cross flow resistance factor	0.5
Single phase turbulent mixing coefficient	0.005
Two-phase turbulent mixing multiplier	Beus model [9]
Two-phase interchannel mixing model	EM model
Quality-void relations	
Subcooled boiling void fraction	Levy model [52]
Saturated boiling void fraction	Modified Armand model [see 86] Chexal-Lellouche model [17]

**Fig. 3.4:** Bundle average exit void fractions calculated with (a) the modified Armand model and (b) the Chexal-Lellouche model.

with Eq. 3.57 and 3.58), are compared with the measured void fractions. Data points of cases with different bundle average exit qualities (in short as “Exit Quality” in both subfigure legends) are distinguished with different colors (about 400 data points per bundle average exit quality, overall about 2400 data points). The two dashed lines in both subfigures indicate the +20% and –20% relative deviation, respectively. According to the criterion proposed by Mishima and Ishii [57], the bubbly to slug flow regime transition void fraction is set at α equals 30%. It is to observe that for the cases with bundle average exit quality higher than 5%, or for subchannel average void fractions larger than 40% (slug-annular flow regime), the consideration of void drift in the EVVD model improves slightly the prediction accuracy of the subchannel void fraction. However, for the cases with bundle average exit quality of 2% or for subchannel average void fractions less than 30% (bubbly flow regime), shown with red cross points in both subfigures, the deviation between prediction and measurement is still large. This reveals, that evaluation of the void drift correction factor K_{VD} with the formulation expressed in Eq. 3.57 for bubbly flow regime is apparently not appropriated. An improvement of the void drift models in the bubbly flow regime is thus required.

For more insight into the performance of the interchannel mixing models in the bubbly flow regime, in addition to the five test cases: 0011-53, 0021-15, 0031-15, 1071-53 and 4101-53

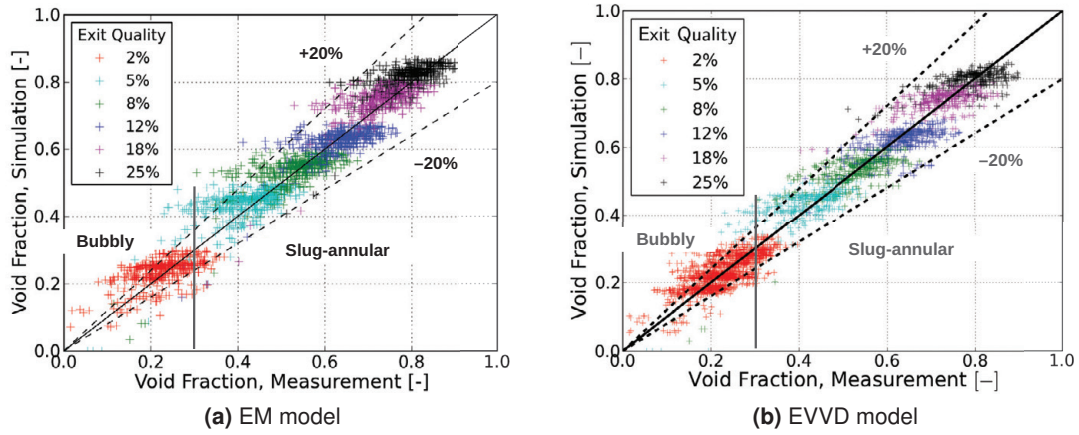


Fig. 3.5: Subchannel average exit void fractions at different bundle average exit qualities with: (a) the equal-mass-exchange turbulent mixing (EM) model and (b) the equal-volume-exchange turbulent mixing with void drift (EVVD) model (Type II).

listed in Tab. 3.1 further 11 test cases of the same exit pressure level of 70 *bar* but varying bundle average mass flux were also selected for recalculation. A sensitivity study of K_{VD} was carried out for the 16 test cases with 2% exit bundle average quality. For evaluating the agreement between calculation and measurement results, two statistic parameters were introduced:

- Root mean square deviation: $RMSD$

$$RMSD = \sqrt{\frac{\sum_{i=1}^{N_C} (\alpha_{p,i} - \alpha_{m,i})^2}{N_C}} \quad (3.63)$$

- Average ratio of calculated void fraction to measured: P/M_{avg}

$$P/M_{avg} = \frac{\sum_{i=1}^{N_C} (\alpha_{p,i}/\alpha_{m,i})}{N_C} \quad (3.64)$$

with $\alpha_{p,i}$, $\alpha_{m,i}$ is the predicted and measured void fraction of subchannel i . N_C stands for the total number of subchannels. Various interchannel mixing models were applied in the sensitivity study: the EM model, the EVVD model type I ($K_{VD} = 1.4$), the EVVD model type II (K_{VD} in the order of 0.3 for 2% bundle average exit quality) and three EVVD models with K_{VD} of 0.1, 0.6 and 1.0, respectively. The statistical results of the assembly 0 with three subtypes 0-1, 0-2 and 0-3 are summarized in Tab. 3.3. For all the subchannels combined, the measured values can be reasonable predicted with all the mixing models. The consideration of void drift has less influence on prediction accuracy of the void fraction in wall and center subchannels. In contrast, the corner subchannel void fraction prediction can be largely influenced by void drift modeling. According to the interchannel mixing mass flow rate expressed in Eq. 3.56, with increasing value of K_{VD} , more net gaseous phase will be transported from corner subchannels with lower mass flux to wall and center subchannels with larger mass flux. This is reflected from the statistical evaluation in Tab. 3.3. With increasing K_{VD} from 0.1 to 0.6, 1.0 and to as high as 1.4 (EVVD, type I), more void is forced to leave the corner subchannels and the

Tab. 3.3: Statistical evaluation of subchannel analysis results of test cases with bundle average exit quality 2%, Assembly type 0

		EM	EVVD Type I	EVVD Type II	EVVD $K_{VD} = 0.1$	EVVD $K_{VD} = 0.6$	EVVD $K_{VD} = 1.0$
All	P/M_{avg}	1.068	1.023	1.058	1.062	1.049	1.038
Channels	$RMSD$	0.036	0.045	0.037	0.037	0.038	0.041
Corner	P/M_{avg}	1.041	0.510	0.936	1.015	0.816	0.655
Channels	$RMSD$	0.036	0.114	0.041	0.036	0.056	0.084
Wall	P/M_{avg}	1.070	0.948	1.038	1.047	1.017	0.990
Channels	$RMSD$	0.040	0.040	0.039	0.039	0.039	0.039
Center	P/M_{avg}	1.068	1.107	1.079	1.075	1.087	1.098
Channels	$RMSD$	0.034	0.037	0.035	0.035	0.036	0.037

P/M_{avg} value of the corner subchannel void fraction decreases. The EVVD model type II with recalculated K_{VD} value about 0.3 gives much better prediction accuracy than the EVVD type I. However, the EVVD model type II still slightly overpredicts the void drift effect. Overall the best prediction accuracy can be achieved with K_{VD} of about 0.1.

The statistical evaluation was further performed for the test cases of assembly type 1 and 4 with non-uniform heat power profile. Results are summarized in Tab. 3.4. It also reveals that

Tab. 3.4: Statistical evaluation of subchannel analysis results of test cases with bundle average exit quality 2%, Assembly type 1 and 4

		EM	EVVD Type I	EVVD Type II	EVVD $K_{VD} = 0.1$	EVVD $K_{VD} = 0.6$	EVVD $K_{VD} = 1.0$
All	P/M_{avg}	1.066	1.001	1.055	1.062	1.044	1.027
Channels	$RMSD$	0.048	0.041	0.044	0.047	0.041	0.039
Corner	P/M_{avg}	1.479	0.832	1.325	1.446	1.226	1.039
Channels	$RMSD$	0.104	0.057	0.076	0.097	0.059	0.040
Wall	P/M_{avg}	1.074	0.964	1.060	1.070	1.042	1.018
Channels	$RMSD$	0.041	0.037	0.039	0.040	0.038	0.037
Center	P/M_{avg}	1.028	1.035	1.029	1.026	1.030	1.032
Channels	$RMSD$	0.045	0.041	0.044	0.045	0.042	0.040

prediction accuracy of the corner subchannel void fraction is largely dependent on void drift modeling. The EM model fails to predict the corner channel void fraction. A better prediction can be obtained with the EVVD model type I and II. The overall best prediction accuracy is achieved with a constant K_{VD} in the order of 1.0, which is 10 times of that for the cases of assembly 0 with uniform power profiles. In the development of the EVVD model type II, all the used experimental results are obtained with uniform axial and radial power profiles [see 33], effect of non-uniformity in power distribution is not considered. This explains perhaps why the EVVD model type II predicts the corner subchannel void fraction for cases with uniform power profiles (assembly type 0) much better than for cases with non-uniform power profiles (assembly type 1 and 4).

In summary for bubbly flow regime under BWR pressure levels (70 bar), the EVVD model type II proposed in [33] can well predict the void fraction distribution in rod bundle with uniform axial and radial power profiles. However, for rod bundle with non-uniform power distribution none of the in MATRA available interchannel mixing models have acceptable prediction accuracy.

3.3.2 ISPRA EUROP benchmark

The flow mixing tests in the ISPRA benchmark [31] were performed with two test sections simulating typical fuel rod bundle of BWR (PELCO-S) and PWR (EUROP), respectively. In the current study, only selected test cases obtained with the EUROP test section under typical PWR pressure levels (160 bar) were recalculated with MATRA. The EUROP test section had an overall heated length of 3660 mm. The axial and radial power distributions for all the test cases were uniform. Seven typical PWR grid spacers without mixing vanes were equally spaced along the heated length to support the rod bundle. The simulated fuel rods with an outer diameter of 10.75 mm were arranged 4×4 square with a pitch of 14.3 mm. The exit enthalpy and mass flow rate distribution in the rod bundle were measured by simultaneously sampling five of the six characteristic subchannels as depicted with shaded areas in Fig. 3.6 using the widely adopted isokinetic techniques and analyzing the exit quality by a calorimetric method. All the measurements was conducted only after several hours of uninterrupted operation of the entire test loop, in order to assure the establishment of steady states with predefined thermal-hydraulic boundary conditions and to minimize the error in the caloric measurements. The maximal error for both subchannel flow and enthalpy measurement was reported to be about 3% [see 31].

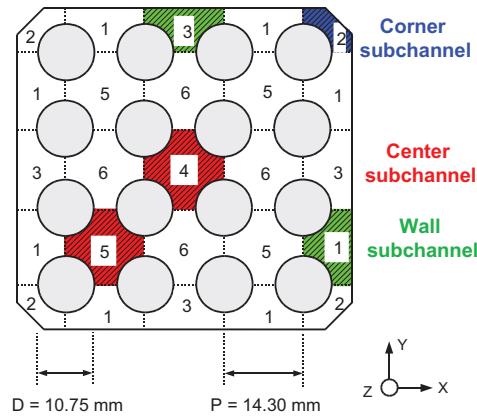


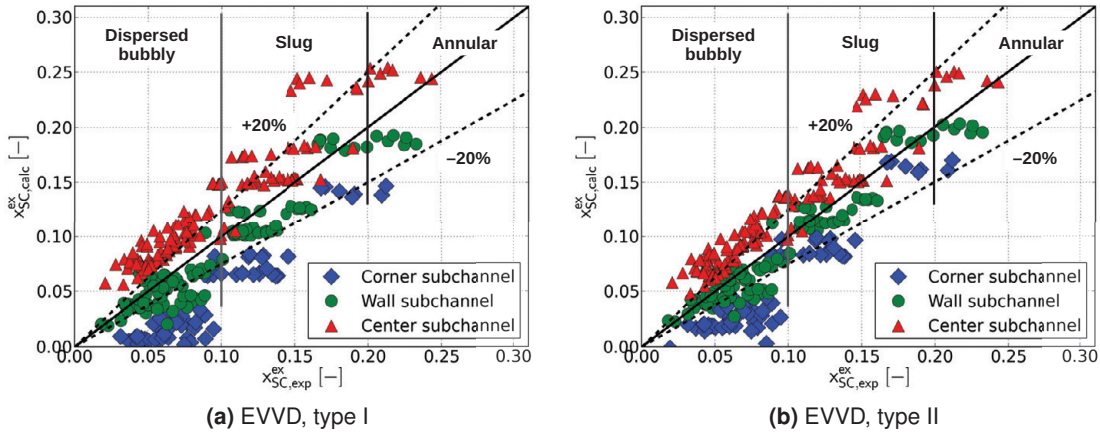
Fig. 3.6: Cross-sectional view of the EUROP test section with shaded areas denoting the sampled five subchannels for flow and enthalpy measurement [31].

70 test cases with exit pressure of 160 bar, bundle average mass flux from $2250 \text{ kgm}^{-2}\text{s}^{-1}$ to $3147 \text{ kgm}^{-2}\text{s}^{-1}$ and varying bundle average exit quality from 3% to 20% were selected for recalculation with MATRA. Relevant models used in the recalculation are summarized in Tab. 3.5. The grid spacer pressure loss coefficient was reported in [31]. Two types of interchannel mixing models were used: the EVVD model type I ($K_{VD} = 1.4$) and the EVVD type II (K_{VD} recalculated). Since the bundle average mass flux and bundle average enthalpy were given as boundary conditions, no comparison of the bundle average flow parameters were made. Comparison of simulation with measurement was performed for the exit equilibrium quality in subchannels. Fig. 3.7 compares the calculated subchannel exit equilibrium qualities of the five sampled subchannels with the corresponding measured values.

According to the transition criteria used in MATRA as expressed with Eq. 3.52, the transition quality to annular flow regime for the selected 70 test cases was calculated at about 0.2. Since no transition from bubbly to slug is specified in MATRA, the flow regime transition criteria proposed by Mishima and Ishii [57] were applied here. Accordingly, under PWR pressure level the flow regime changes from dispersed bubbly flow towards slug flow regime at the transition quality of about 0.1. With these two flow regime transition criteria, namely bubbly to slug at quality of 0.1 and slug to annular at 0.2, the results shown in Fig. 3.7 were discussed. It is

Tab. 3.5: MATRA models used for recalculation of selected ISPRA EUROP test cases: assessment of interchannel mixing models

Pressure drop models	
Single phase turbulent friction factor	$0.184 \cdot Re^{-0.2}$
Two-phase friction multiplier	Armand model
Grid spacer pressure lost factor	0.944
Quality-void relations	
Subcooled boiling void fraction	Levy model
Saturated boiling void fraction	Modified Armand model
Interchannel mixing models	
Diversion cross flow resistance factor	0.5
Single phase turbulent mixing coefficient	0.005
Two-phase turbulent mixing multiplier	Beus model
Two-phase interchannel mixing model	EVVD model type I & II


Fig. 3.7: Calculation of subchannel exit quality of ISPRA EUROP test cases with (a) the EVVD model type I ($K_{VD} = 1.4$) and (b) the EVVD model type II (K_{VD} recalculated with Eq. 3.57 and 3.58).

clearly seen that most of the studied cases locate in the bubbly-slug flow regime. The EVVD model type I with a constant K_{VD} of 1.4 overpredicts the void drift effect, which according to Eq. 3.56 enforces a void migration out of corner subchannel to wall subchannel and further to center subchannel. This is reflected by the general underprediction of quality in the corner subchannel (channel type 2) and the overprediction of quality in the center subchannel (channel type 4 and 5), especially in the dispersed bubbly flow regime with quality lower than 0.1. The EVVD model type II on the other hand shows a better prediction accuracy than the EVVD model type I in the slug and annular flow regime (quality larger than 0.1). The recalculated K_{VD} values according Eq. 3.57 and 3.58 for the qualities 0.10 and 0.20 are 0.10 and 0.18, which are much smaller than 1.4. However, in the bubbly flow regime (quality smaller than 0.1) void drift effect is significantly overpredicted, despite of the fact that the recalculated K_{VD} for bubbly flow regime is already quite small (for quality of 0.05 K_{VD} is about 0.05).

The same trend can also be found with the relative enthalpy increase, which is defined for an arbitrary subchannel i as the ratio of subchannel wise enthalpy increase to the bundle average enthalpy increase:

$$h_{inr} = \frac{h_i^{ex} - h_i^{in}}{h_b^{ex} - h_b^{in}} \quad (3.65)$$

with the subscripts i and b denoting the subchannel and bundle average values, respectively. The superscripts in and ex denote flow parameters at the inlet and outlet of the subchannels. In Fig. 3.8 the prediction to measurement ratio (P/M) of relative channel enthalpy increase is plotted versus the measured bundle average exit quality $x_{b,exp}^{ex}$. The calculated K_{VD} in the

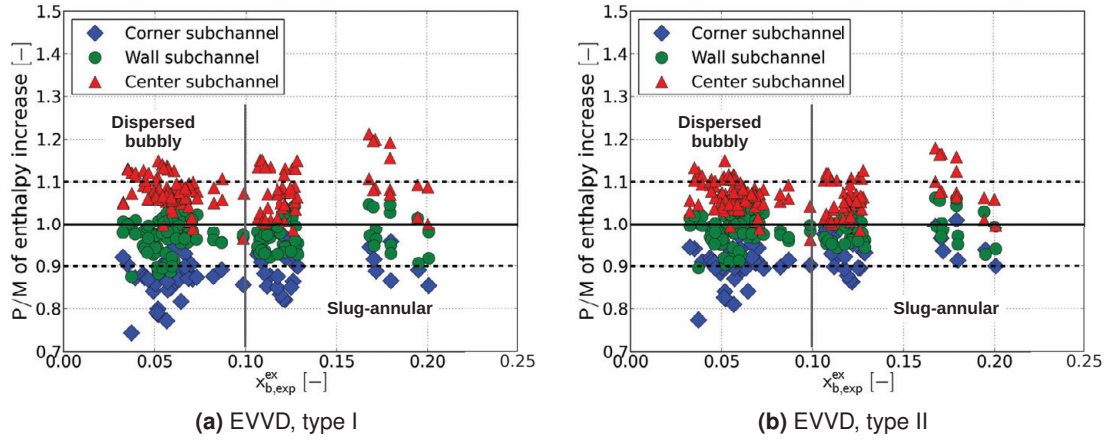


Fig. 3.8: Calculation of subchannel relative enthalpy increase of ISPRA EUROP test cases with (a) the EVVD model type I ($K_{VD} = 1.4$) and (b) the EVVD model type II (K_{VD} recalculated with Eq. 3.57 and 3.58).

EVVD model type II improves the prediction accuracy compared to the EVVD model type I with K_{VD} as a constant of 1.4. However, in dispersed bubbly flow regime the corner subchannel enthalpy increase is underpredicted, while that of the center subchannel is overpredicted.

The discussion above confirms the improvement demand of the void drift model in the bubbly flow regime as observed in the recalculation of the NUPEC BFBT test cases (see Fig. 3.5). Furthermore, the underprediction of quality and enthalpy increase in the corner channel with the simultaneous overprediction of that in the center subchannel implies that the assumed tendency of void migration towards subchannel with larger mass flux due to void drift effect may be not valid for the dispersed bubbly flow regime as encountered in ISPRA EUROP test cases. A sensitivity study was carried out with K_{VD} equal to -2.0 , -4.0 and -6.0 , respectively. Among the three tested values, the best agreement for the dispersed bubbly flow regime was found for K_{VD} equals -4.0 , for which the results are shown in Fig. 3.9. It is demonstrated that

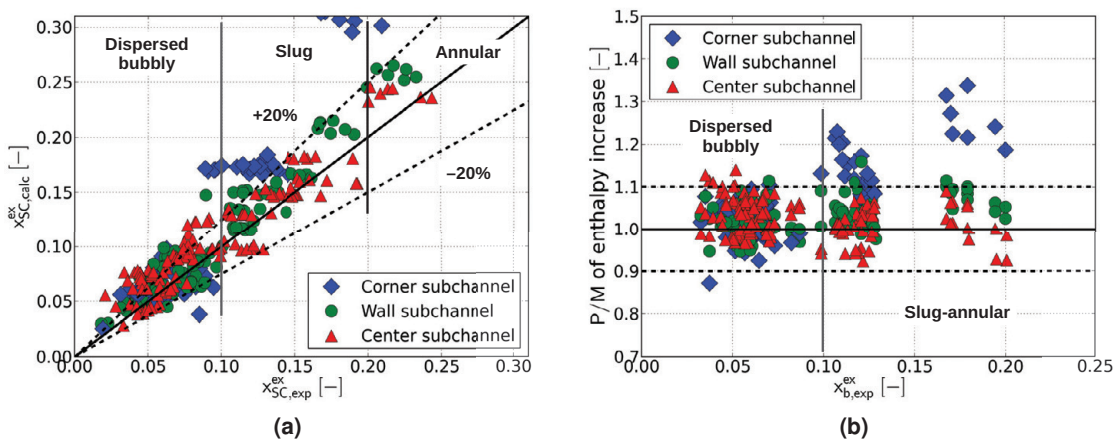


Fig. 3.9: Recalculation of ISPRA EUROP test cases with $K_{VD} = -4.0$.

with negative value of K_{VD} the prediction accuracy of the subchannel exit quality and enthalpy increase is considerably improved. However, for the slug and annular flow regime the corner subchannel exit quality and enthalpy increase are largely overpredicted. This reveals that for the dispersed bubbly flow regime under PWR pressure level, void drift effect enforces apparently a void migration towards the corner subchannel with lower mass flux. The assumption proposed by Lahey and Moody [47] of gaseous phase tend to accumulate in subchannel of higher mass flux is apparently only valid in the slug and annular flow regime.

3.4 Conclusion and discussion

In this chapter the interchannel mixing models currently available in MATRA were assessed by recalculation of selected test cases from both the NUPEC BFBT benchmark and the ISPRA EUROP benchmark. The most important conclusions are summarized here:

- Void drift effect depends on two-phase flow regime for both BWR and PWR pressure levels. The EVVD model type I with a constant K_{VD} for all the flow regimes is not appropriate. A better prediction accuracy can be achieved with the EVVD model type II, which calculates K_{VD} in dependence on system pressure and flow regime.
- In general, the EVVD model type II gives acceptable good prediction of subchannel flow parameters in slug and annular flow regime. However, in bubbly flow regime prediction accuracy with the EVVD model type II is not satisfied. Under BWR pressure levels, this dissatisfaction is observed in the subchannel exit void fraction in the bubbly flow regime. A sensitivity study shows that the best agreement is achieved with K_{VD} about 0.1, which indicates a less importance of void drift in the bubbly flow regime under BWR pressure levels. Furthermore, the positive value of K_{VD} implies that gaseous phase tends to move towards subchannels with larger mass flux in the bubbly flow regime under BWR pressure levels. However, for bubbly flow regime under PWR pressure level, the best agreement is found for K_{VD} equals -4.0 . This means that gaseous phase tends to migrate towards subchannels with lower mass flux in the bubbly flow regime under PWR pressure levels. This is in opposition to the assumption of Lahey and Moody [47], on which the void drift model in MATRA is based. Apparently, the void drift models currently available in MATRA require improvement in the bubbly flow regime under PWR pressure levels.

To sum up, the currently in MATRA available EVVD model needs improvement for application to bubbly flow regime under PWR pressure levels. Improvement should be conducted regarding two aspects:

- The void drift correction factor K_{VD} in MATRA is used in Levy's model [51] to correlate void fraction distribution at equilibrium state with mass flux distribution. In this approach only the influence of the mass flux distribution on void fraction distribution at equilibrium state is considered. For two subchannels of different geometries, for instance a wall subchannel interacting with a center subchannel, geometrical difference may also arise non-uniformity in the equilibrium void fraction distribution. For a more complete and better modeling of void fraction distribution at equilibrium state, both effects of mass flux distribution and geometrical difference between interacting subchannels should be considered.
- In the EVVD model proposed by Lahey and Moody [47], see Eq. 3.54, the mixing effect due to turbulent mixing and void drift is combined modeled. The same effective mixing

velocity, interpreted with the single phase turbulent mixing coefficient β_{SP} and the Beus two-phase turbulent mixing multiplier θ [9], is used In MATRA for both turbulent mixing and void drift. However, these two mixing effects are apparently induced by different physical mechanisms. Due to the irregular nature of turbulent fluctuation, turbulent mixing is regarded as a non-directional mixing effect, while void drift is a directional mixing effect with a prevailing direction. The use of the same effective mixing velocity for two different mixing effects in the EVVD model is rather questionable. Turbulent mixing and void drift should be separately considered in the improved interchannel mixing model.

4. Validation of two-phase CFD model for predicting two-phase interchannel mixing

Based on the above subchannel analysis, the improvement demand of the void drift models in MATRA was identified for the bubbly flow regime. In order to better understand the two phase bubbly flow behavior in rod bundle geometry, CFD approach with the commercial software package Ansys CFX was employed in the present study. Prior to simulations, the employed two-phase CFD model should be validated. In this chapter, the Eulerian two-fluid-approach in Ansys CFX was briefly reviewed. Subsequently, sensitivity study and validation calculation of the Eulerian two-fluid model were carried out regarding its application to predict the two-phase interchannel mixing phenomena.

4.1 Eulerian two-fluid model in Ansys CFX

The following sections present a brief description of two-phase flow modeling with the Eulerian two-fluid model in Ansys CFX. Two-fluid methodology is applicable to all flow regimes, including separated, dispersed or intermediate regimes. However, as described by Janssens-Maenhout [36] all the closure relations for interphase transfers are derived for a single bubble then extended to multiple bubbles with ensemble averaging. Therefore, the Eulerian two-fluid model is strictly speaking only applicable for the bubbly flow regime, which is also the subject flow regime of the current study. The two-phase bubbly flow consisting of a continuous liquid phase and a gaseous phase dispersed inside the continuous phase in form of bubbles. Henceforth the continuous liquid phase is denoted with subscript l , while the dispersed gaseous phase with subscript g .

4.1.1 Governing equations

In the Eulerian two-fluid model, both phases are described using Eulerian conservation equations. Hence, the model is also referred to as the Euler-Euler model. The two phases are considered as continuum, that can interpenetrate each other. Both phases are represented by averaged conservation equations. Through the averaging process, the volume fraction α is introduced into the equation set, which is defined as the probability of a certain phase is present at a certain point in space and time [see 71]. In the averaged aspect, α is then the volume fraction of an individual phase occupying the finite control volume, defined for an arbitrary phase ϕ as:

$$\alpha_\phi = \frac{V_\phi}{V_l + V_g} \quad (4.1)$$

with the subscript ϕ denotes the phase l or g . The conservation equations are established for each phase separately, leading to two continuity equations, six momentum equations and two energy equations. In general, each phase has its own velocity, temperature and physical properties. The pressure in a finite control volume is assumed to be the same for both phases.

In case of bubbly flow, this assumption is justified as long as the bubble diameter is not too small so that surface tension related phenomena have a minor impact on the flow. In the current study, the considered bubble diameter is in mm range, so that the pressure difference between the continuous liquid phase and the dispersed bubbles is negligible. This pressure constraint yields¹:

$$\bar{p}_g = \bar{p}_l \quad (4.2)$$

In the current study, both phases are considered to be incompressible with constant physical properties. The two-phase flow is treated as isothermal, hence no interphase transfer of mass or energy needs to be considered. Therefore, the averaged continuity and momentum equations for an arbitrary phase ϕ are given as:

$$\frac{\partial \alpha_\phi}{\partial t} + \nabla \cdot (\alpha_\phi \bar{\mathbf{U}}_\phi) = 0 \quad (4.3)$$

$$\frac{\partial \alpha_\phi \bar{\mathbf{U}}_\phi}{\partial t} + \nabla \cdot (\alpha_\phi \bar{\mathbf{U}}_\phi \bar{\mathbf{U}}_\phi) = -\frac{\alpha_\phi}{\rho_\phi} \nabla \bar{p} + \frac{1}{\rho_\phi} \nabla \cdot (\alpha_\phi \bar{\mathbf{R}}_\phi^{eff}) + \alpha_\phi \mathbf{g} + \frac{\bar{\mathbf{M}}_\phi}{\rho_\phi} \quad (4.4)$$

where $\bar{\mathbf{R}}_\phi^{eff}$ is the sum of the viscous stress tensor $\bar{\mathbf{R}}_\phi$ and the Reynolds stress tensor \mathbf{R}'_ϕ . $\bar{\mathbf{M}}_\phi$ is the averaged interphase momentum transfer. The Reynolds stress tensor and the interphase momentum transfer arise from the averaging process and require closure relations, which will be discussed in subsequent chapters. Combining Eq. 4.3 for both phases yields the volume conservation equation:

$$\nabla \cdot (\alpha_g \bar{\mathbf{U}}_g + \alpha_l \bar{\mathbf{U}}_l) = 0 \quad (4.5)$$

With the above 2 continuity equations, 6 momentum equations, 1 volume conservation equation and 1 pressure constraint a complete set of 10 hydrodynamic equations is built for solving the 10 unknown flow parameters: namely 6 velocities, two void fractions and two pressures. Closure relations are required for the interphase momentum transfer terms and the Reynolds stress.

4.1.2 Interphase momentum transfer

Conservation of the global momentum dictates that the sum of the interphase momentum transfer terms must be zero, i.e. $\sum \bar{\mathbf{M}}_\phi = 0$. Expression of the interphase momentum transfer of only one phase is sufficient to close the equation system. Its derivation, which will be briefly stated in this chapter, begins from the instantaneous forces acting on this phase. In the first step, the instantaneous interphase momentum transfer is determined by assembling the forces acting on single dispersed bubble. The key parameter in this process is the interphase surface A_{gl} between the two phases. For n bubbles with constant bubble diameter D_g in a finite control volume V , the interphase surface A_{gl} can be expressed as:

$$\frac{A_{gl}}{V} = \frac{n\pi D_g^2}{n\pi D_g^3/6} \cdot \frac{V_g}{V} = \frac{6\alpha}{D_g} \quad (4.6)$$

The interphase forces, most notably, drag force, lift force, virtual mass force and wall lubrication force, acting on bubbles will be accumulated to a volumetric force (dimension $[Nm^{-3}]$) acting on the entire control volume V . The instantaneous interphase momentum transfer term can be decomposed into elemental components depending on their different origins:

$$\bar{\mathbf{M}}_g = \mathbf{F}_D + \mathbf{F}_L + \mathbf{F}_{VM} + \mathbf{F}_{WL} \quad (4.7)$$

¹Overline in the current study denotes Reynolds-average flow parameters.

\mathbf{F}_D , \mathbf{F}_L , \mathbf{F}_{VM} and \mathbf{F}_{WL} stand for the instantaneous drag force, lift force, virtual mass force and wall lubrication force, respectively. In Ansys CFX, the following forms are applied [2]:

$$\mathbf{F}_D = -C_D \frac{3}{4} \frac{\alpha_g}{D_g} \rho_l |\bar{\mathbf{U}}_g - \bar{\mathbf{U}}_l| (\bar{\mathbf{U}}_g - \bar{\mathbf{U}}_l) \quad (4.8)$$

$$\mathbf{F}_L = -C_L \rho_l \alpha_g (\bar{\mathbf{U}}_g - \bar{\mathbf{U}}_l) \times (\nabla \times \bar{\mathbf{U}}_l) \quad (4.9)$$

$$\mathbf{F}_{VM} = -C_{VM} \rho_l \alpha_g \left(\frac{D}{Dt} \bar{\mathbf{U}}_g - \frac{D}{Dt} \bar{\mathbf{U}}_l \right) \quad (4.10)$$

$$\mathbf{F}_{WL} = C_{WL} \rho_l \alpha_g |\bar{\mathbf{U}}_g - \bar{\mathbf{U}}_l|^2 \mathbf{n}_W \quad (4.11)$$

where \mathbf{n}_W is the unit normal vector pointing away from the wall. The dimensionless coefficients C_D , C_L , C_{VM} and C_{WL} are usually determined with empirical correlations consisting of physical properties, form of bubbles (spherical, ellipsoidal etc.) and flow condition around the bubbles.

In the second step the instantaneous interphase momentum terms are averaged. Additional terms are hence produced, most notably, the turbulent drag term, which is expressed as a turbulent dispersion force. The CFX solver implements a model for turbulent dispersion force, based on the Favre averaged interphase drag force combined with the eddy diffusivity hypothesis [12]:

$$\mathbf{F}_{TD} = C_{TD} C_D \frac{3}{4} \frac{\alpha_g}{D_g} \rho_l |\bar{\mathbf{U}}_g - \bar{\mathbf{U}}_l| \frac{\nu_{t,l}}{\sigma_{t,l}} \left(\frac{\nabla \bar{\alpha}_l}{\bar{\alpha}_l} - \frac{\nabla \bar{\alpha}_g}{\bar{\alpha}_g} \right) \quad (4.12)$$

with $\nu_{t,l}$ and $\sigma_{t,l}$ stand for the turbulent kinematic viscosity of the continuous liquid phase and the turbulent Schmidt number of the continuous liquid phase volume fraction (currently taken as 0.9 [2]), respectively. The dimensionless turbulent dispersion force coefficient C_{TD} is by default taken as unity [2]. For the two-phase bubbly flow considered in the current study, it yields:

$$\bar{\alpha}_g + \bar{\alpha}_l = 1 \quad (4.13)$$

hence

$$\nabla \bar{\alpha}_g + \nabla \bar{\alpha}_l = 0 \quad (4.14)$$

The above formulation of the turbulence dispersion force can be further reduced to a simple volume fraction gradient of the bubbly phase:

$$\mathbf{F}_{TD} = -C_{TD} C_D \frac{3}{4} \frac{\alpha_g}{D_g} \rho_l |\bar{\mathbf{U}}_g - \bar{\mathbf{U}}_l| \frac{\nu_{t,l}}{\sigma_{t,l}} \left(\frac{1}{\bar{\alpha}_l} + \frac{1}{\bar{\alpha}_g} \right) \nabla \bar{\alpha}_g \quad (4.15)$$

It is seen that the model of turbulent dispersion force is dependent on the modeling of drag force. Turbulent dispersion force acts in the opposite direction of void fraction gradient and hence causes bubbles to move from regions of high concentration to regions of low concentration. With respect to void fraction distribution, turbulent dispersion force smooths the local void fraction distribution. The averaging process can also be carried out for drag force, lift force and virtual mass force. However, as found in [8], the additional effects are not significant. In the current study, only the turbulent dispersion force due to the Favre averaged drag force is considered.

4.1.3 Turbulence modeling

Eddy-viscosity model

In the averaged momentum equation given in Eq. 4.4, the Reynolds stress term \mathbf{R}'_ϕ needs closure, which requires some approximations usually prescribing the Reynolds stress in terms

of the mean flow quantities. Such approximations are referred to as turbulence models in engineering applications. The most widely used approach assumes that the effect of turbulence can be represented as an increased viscosity, which leads to the eddy-viscosity models [see 23] for Reynolds stress^I:

$$\mathbf{R}'_{\phi} = \mu_t \cdot \left(\frac{\partial \bar{U}_i}{\partial x_j} + \frac{\partial \bar{U}_j}{\partial x_i} \right) - \frac{2}{3} \rho \delta_{ij} k \quad (4.16)$$

with μ_t stands for the turbulent viscosity, which is also called as the eddy viscosity. k is the turbulence kinetic energy defined as^{II}:

$$k = \frac{1}{2} \overline{u'_i u'_i} = \frac{1}{2} \left(\overline{u'_x u'_x} + \overline{u'_y u'_y} + \overline{u'_z u'_z} \right) \quad (4.17)$$

In the simplest manner, turbulence can be characterized by two parameters: the turbulence kinetic energy k and a length scale L_t . With dimension analysis it yields:

$$\mu_t = C_{\mu} \rho \sqrt{k} L_t \quad (4.18)$$

with C_{μ} is a dimensionless constant. \sqrt{k} has the dimension of velocity is hence also referred to as the turbulence velocity scale. Different approaches are available to determine the two characteristic parameters. Depending on the number of additional equations that must be solved, normally one can distinguish between zero-equation, one-equation and two-equation models. It must be mentioned that phase dependent turbulence models are applied in the current study for the bubbly two-phase flow. The eddy-viscosity hypothesis is assumed to hold for each phase individually. Diffusion of the momentum in phase ϕ is hence governed by an effective viscosity of this phase $\mu_{eff,\phi}$:

$$\mu_{eff,\phi} = \mu_{\phi} + \mu_{t,\phi} \quad (4.19)$$

with μ_{ϕ} and $\mu_{t,\phi}$ stand for the molecular and turbulent viscosity of the phase ϕ , respectively. Two variants of the eddy-viscosity models: namely the dispersed phase zero-equation model and the k - ϵ two-equation model will be discussed below, which are applied in the current study for the dispersed gaseous phase and the continuous liquid phase, respectively.

Dispersed phase zero-equation model

Generally in a zero-equation model no additional equation needs to be solved for quantifying turbulence. Rather simple algebraic relations are used for evaluation of the turbulent viscosity. By default in a zero-equation model the turbulent viscosity is modeled as the product of a turbulence velocity scale $U_{t,\phi}$ and a turbulence length scale $L_{t,\phi}$:

$$\mu_{t,\phi} = f_{\mu} \rho_{\phi} U_{t,\phi} L_{t,\phi} \quad (4.20)$$

with f_{μ} is a proportional constant taking the value of 0.01 in Ansys CFX [see 2]. The turbulence velocity scale $U_{t,\phi}$ is calculated to be the maximum velocity in phase ϕ and the turbulence length scale $L_{t,\phi}$ is given as:

$$L_{t,\phi} = \frac{V_D^{1/3}}{7} \quad (4.21)$$

with V_D is the fluid domain volume. The above default formulation of the zero-equation model is correlated for single phase turbulent pipe flow hence not recommended for usage in multi-phase flow. For a dispersed phase, the dispersed phase zero-equation model may be used. A

^IEinstein convention is adopted that whenever the same index appears twice in any term, summation over the range of that index is implied.

^{II}Einstein convention is adopted.

turbulent viscosity Prandtl number σ is specified, which relates the dispersed phase turbulent kinematic viscosity $\nu_{t,g}$ simply with the continuous liquid phase turbulent kinematic viscosity $\nu_{t,l}$ in this manner:

$$\sigma = \frac{\nu_{t,l}}{\nu_{t,g}} \quad (4.22)$$

Hence the dispersed phase turbulent viscosity is given by:

$$\mu_{t,g} = \frac{\rho_g \mu_{t,l}}{\rho_l \sigma} \quad (4.23)$$

For σ the default value of unity is appropriated for dispersed bubbles or very small solid particles. The dispersed phase zero-equation model is recommended in Ansys CFX [see 2] for a dispersed phase and is hence used in the current study for the dispersed bubbly phase. The modeling in Eq. 4.23 implies that the turbulent fluctuation of the dispersed phase is dictated by the continuous phase. The dispersed phase turbulent viscosity is directly proportional to that of the continuous phase and is furthermore much smaller than that of the continuous phase, because the density of the liquid phase ρ_l is much larger than that of the gaseous phase ρ_g . This is somehow justified for bubbly two-phase flow due to the fact that the continuous liquid phase is the dominant phase while the turbulence inside the dispersed bubbles have less impact on the overall flow behavior.

***k*- ϵ two-equation model**

Accurate prescription of turbulence with the zero-equation model is only possible for very simple flows but not for highly turbulent three-dimensional flows. Difficulties arising in quantifying turbulence suggest that partial differential equations might be used for evaluating turbulence. Since two characteristic parameters, a velocity scale and a length scale, are required to describe turbulence, a two-equation models with a separate transport equation for determining each of the characteristic parameter is a logic choice. In the current study the most widely used *k*- ϵ two-equation model [50] with an equation for the turbulence kinetic energy k_l determining the velocity scale and an equation for the dissipation rate of k_l denoted with ϵ_l is applied for the continuous liquid phase. With the observation that in so-called equilibrium turbulent flows the production and destruction of turbulence are in near balance, ϵ_l , k_l and the turbulence length scale $L_{t,l}$ are related with:

$$\epsilon_l \approx \frac{k_l^{3/2}}{L_{t,l}} \quad (4.24)$$

This relation allows that with one equation for the dissipation rate ϵ_l both ϵ_l and $L_{t,l}$ can be obtained. Together with Eq. 4.18 the turbulent viscosity of the continuous liquid phase can be obtained with:

$$\mu_{t,l} = C_{\mu} \rho_l \frac{k_l^2}{\epsilon_l} \quad (4.25)$$

The derivation and detailed formulation of single phase *k* and ϵ equations are not presented here and referred to literature [104]. For application in two-phase flow, the transport equation of *k* and ϵ are assumed to take a similar form to the single phase ones [see 2]. Here is presented for the continuous liquid phase, the *k* equation is given as:

$$\frac{\partial}{\partial t} (\alpha_l \rho_l k_l) + \nabla \cdot (\alpha_l \rho_l \bar{\mathbf{U}}_l k_l) = \nabla \cdot \left[\alpha_l \left(\mu_l + \frac{\mu_{t,l}}{\sigma_k} \right) \nabla k_l \right] + \alpha_l (P_{k,l} - \rho_l \epsilon_l) \quad (4.26)$$

The two terms of the left hand side are the transient and convection of k_l . The first term on the right hand side is the viscous and turbulent diffusion of k_l . $\mu_{t,l}/\sigma_k$ is the eddy diffusivity

of k_l with σ_k as a turbulent Prandtl number, similar to the definition of eddy diffusivity of a scalar such as temperature. The term $P_{k,l}$ represents the production rate of k_l by the mean flow, which is the transfer rate of kinetic energy from the mean flow to the turbulence. Provided eddy-viscosity model is used to evaluate the Reynolds stress, $P_{k,l}$ can be written for incompressible flow as¹:

$$P_{k,l} = -\overline{\rho u'_i u'_j} \frac{\partial \bar{U}_{l,i}}{\partial x_j} \approx \mu_{t,l} \left(\frac{\partial \bar{U}_{l,i}}{\partial x_j} + \frac{\partial \bar{U}_{l,j}}{\partial x_i} \right) \frac{\partial \bar{U}_{l,i}}{\partial x_j} \quad (4.27)$$

For the dissipation rate ϵ , the rate at which turbulent energy is irreversibly converted into internal energy, the following equation is given:

$$\frac{\partial}{\partial t} (\alpha_l \rho_l \epsilon_l) + \nabla \cdot (\alpha_l \rho_l \bar{\mathbf{U}}_l \epsilon_l) = \nabla \cdot \left[\alpha_l \left(\mu_l + \frac{\mu_{t,l}}{\sigma_\epsilon} \right) \nabla \epsilon_l \right] + \alpha_l \frac{\epsilon_l}{k_l} (C_{\epsilon 1} P_{k,l} - C_{\epsilon 2} \rho_l \epsilon_l) \quad (4.28)$$

It has to be mentioned that in the above two-phase k and ϵ equations used in the Ansys CFX solver, the interphase transfer terms of k and ϵ are neglected. For the five constants contained in the two equations, the following values are taken in Ansys CFX [see 2]:

$$C_\mu = 0.09; \quad C_{\epsilon 1} = 1.44; \quad C_{\epsilon 2} = 1.92; \quad \sigma_k = 1.0; \quad \sigma_\epsilon = 1.3 \quad (4.29)$$

The form of the k - ϵ -model presented above is valid only for fully turbulent flows. In the vicinity of a no-slip solid walls the turbulence nature is considerably different from that in the other parts of the flow. Near a no-slip wall strong gradients of flow parameters exist. Additionally the local turbulence Reynolds number Re_t , defined as $(\rho \sqrt{k} L_t / \mu)$ with L_t given by Eq. 4.24, becomes inevitably small so that viscous effects on the transport processes prevail over turbulent effects. Experiments have shown that the near wall region can be divided into two sublayers. In the innermost layer, the so-called viscous sublayer, the flow is almost laminar and the molecular viscosity (viscous effects) dominates the momentum and heat transfer. In the layer further away from the wall, the so-called logarithmic sublayer, the turbulent effects overcome the viscous effects and play a dominant role in the momentum and heat transfer. Finally between the viscous and the logarithmic sublayers, a transition sublayer exist, where the viscous and turbulent effects are of equal importance. To resolve the near wall turbulence, one possibility is to solve the equations completely up to the wall with a fine grid resolution. When this is done, some modifications of the turbulence models must be carried out. This is mainly due to the fact that directly near the wall turbulence is strongly damped and become highly anisotropic (fluctuation is more strongly damped in direction normal to the wall than in other direction). This leads to the so-called low-Reynolds-number^{II}- k - ϵ -model, for instance given in [50]. However difficulties arise at high Reynolds numbers, where the viscous sublayer becomes so thin that it is almost infeasible to use enough grid points to resolve it. Furthermore the cells near the wall will become very flat, which may have negative impacts on the numerical stability and convergence behavior. This problem can be circumvented by using wall functions, which assumes that the logarithmic velocity profile existing in the logarithmic sublayer can also reasonably approximate the velocity distribution up to the wall including the transition and the viscous sublayers. The logarithmic velocity profile is given as:

$$u^+ = \frac{\bar{U}_t}{u_\tau} = \frac{1}{\kappa} \ln y^+ + B \quad (4.30)$$

¹Einstein convention is adopted.

^{II}Not that low-Reynolds number dose not refer to the device Reynolds number, but to the turbulence Reynolds number, which is low in the viscous sublayer. Low-Reynolds-number model is also applicable for cases of high device Reynolds number

with \overline{U}_t the mean velocity parallel to the wall and u_τ is the so-called wall shear velocity given by:

$$u_\tau = \sqrt{\frac{\tau_W}{\rho}} \quad (4.31)$$

with τ_W the shear stress at the wall defined as:

$$\tau_W = \mu \left(\frac{\partial u_t}{\partial y} \right)_{y=0} \quad (4.32)$$

with u_t is the instantaneous flow velocity parallel to the wall and y is the distance to the wall. κ is the von Karman constant taking the value of 0.41 and B is an empirical constant related to the thickness of the viscous sublayer. In Ansys CFX for smooth walls the value of B is assumed as about 5.5. For rough walls, smaller values for B are obtained depending on the wall roughness [see 2]. y^+ is the dimensionless distance from the wall defined as:

$$y^+ = \frac{\rho u_\tau y}{\mu} \quad (4.33)$$

The problem in the usage of wall function is that the derivation of velocity parallel to the wall in the direction normal to the wall directly on the wall $(\partial u_t / \partial y)_{y=0}$ can not be directly calculated, because the viscous sublayer is not fully resolved when using wall function. A simple finite difference using the velocity parallel to the wall at the first grid point above the wall denoted with P (or at the center of the finite control volume nearest to the wall) will strongly underestimate $(\partial u_t / \partial y)_{y=0}$. Hence approximation of the wall shear stress must be carried out. It is often assumed that the flow is in local equilibrium, meaning that production and dissipation of turbulence are nearly equal, u_τ is given with [see 23]:

$$u_\tau = C_\mu^{1/4} \sqrt{k} \quad (4.34)$$

From this equation and the logarithmic velocity profile (Eq. 4.30), an expression connecting the velocity at the first grid point above the wall denoted with P (or at the center of the finite control volume nearest to the wall) and the wall shear stress can be derived [see 23]:

$$\tau_W = \rho C_\mu^{1/4} \sqrt{k} \frac{\kappa \overline{U}_{t,P}}{\ln y_P^+ + B} \quad (4.35)$$

with $\overline{U}_{t,P}$ and y_P^+ stand for the mean velocity parallel to the wall at the grid point P and the dimensionless wall distance of the grid point P , respectively. With this expression the wall shear stress τ_W can be estimated with $\overline{U}_{t,P}$ without resolving the viscous sublayer with very fine grid resolution. τ_W provides the tangential force acting on the wall face of the finite control volume nearest to the wall, which can be further decomposed into elemental components depending on the used coordinate system and used as boundary momentum flux for solving the momentum equation in the first near wall control volume.

Compared to fully resolving up to the wall, the usage of wall function economizes computational time and storage. It also allows the introduction of additional empirical information such as for rough walls [50]. However one major drawback of the wall function approach is that the predictions depend on the location of the first grid point P that is the nearest to the wall. Prediction accuracy is sensitive to the near-wall mesh resolution. Refining the mesh does not necessarily gives a unique solution of increased accuracy [30], if y_P^+ drops below 11.06, which is the intersection between the viscous and the logarithmic sublayer. In this case, the solution of the boundary layer away from the wall (beyond the first element) may drop into the viscous sublayer and the assumption of a logarithmic velocity profile is no longer valid. Despite a finer mesh, the solution accuracy could actually be worse. This problem of inconsistency in the wall

function is overcome in Ansys CFX with the usage of the so-called scalable wall function [see 2], in which a lower limit of 11.06 is applied for the y^+ value used in the logarithmic velocity profile:

$$\tilde{y}^+ = \max(y^+, 11.06) \quad (4.36)$$

In this manner the computed \tilde{y}^+ is not allowed to fall below 11.06, which ensures that all mesh points used in the logarithmic velocity formulation are outside the viscous sublayer. The inconsistency in mesh refinement is hence avoided.

Turbulence enhancement

In a bubbly flow the turbulence of the continuous liquid phase is also affected by the relative movement of the dispersed bubbles. This so-called bubble induced turbulence is accounted in Ansys CFX using Sato's model [76] of enhanced continuous liquid phase turbulent viscosity. Accordingly, the effective viscosity of the liquid phase is decomposed into three terms:

$$\mu_{eff,l} = \mu_l + \mu_{t,l} + \mu_{b,l} \quad (4.37)$$

with μ_l , $\mu_{t,l}$ and $\mu_{b,l}$ stand for the molecular viscosity, the turbulent viscosity obtained via turbulence models and the bubble induced viscosity of the liquid phase, respectively. $\mu_{b,l}$ is evaluated with:

$$\mu_{b,l} = C_{\mu b} \rho_l \alpha_l D_g |\bar{\mathbf{U}}_g - \bar{\mathbf{U}}_l| \quad (4.38)$$

with $C_{\mu b}$ has the value of 0.6.

4.1.4 Solution strategy - the coupled solver

A segregated solver employs a solution strategy where the momentum equations are first solved using a guessed pressure. With substitution of the discretized momentum equation into the continuity equation, an equation for pressure correction is obtained. With the corrected pressure the velocity field is then updated. This so-called pressure-velocity coupling will be repeated till both momentum and continuity equations are converged. Ansys CFX used however a coupled solver, in which the hydraulic equations (for \mathbf{U} and p) are solved as a single system. Hence no pressure-velocity coupling is required, since it is already implicitly considered in solving the hydraulic equation system. A coupled solver takes more time per iteration and uses more memory as the matrix of equation system is larger. But a coupled solver provides the advantage that it usually converges much faster than a segregated solver. Further detailed information of the solution strategy is referred to [2].

4.2 Validation of two-phase CFD model

To validate CFD model an appropriate experimental geometrical domain needs to be selected. For the purpose of validating CFD model for predicting two-phase interchannel mixing, the geometrical domain considered must consist of at least two laterally connected subchannels that can interact with each other. Furthermore, channel inserts such as grid spacers, mixing vanes, etc, should not be considered, in order to avoid additional flow disturbance and extremely high numerical efforts. With respect to these two criteria, two-phase interchannel mixing tests conducted by Gonzalez-Santalo and Griffith [29], van der Ros [101] in simple two-channel systems were chosen in the current study for the validation purpose.

Another essential point of validation is an appropriate definition of target variables, which should be easily available and also representative to the subject of interest. In the two-channel

mixing experiments conducted in [29, 101], the subchannel average phase distribution were measured, which are quite suitable for assessing the interchannel mixing effect. Related to CFD simulation, the subchannel scale flow parameters can be then obtained by averaging the flow parameters over the cross section of the subchannels. The calculated subchannel scale flow parameters, such as void fraction, can be used for comparison with the measured subchannel scale flow parameters.

In the following, an overview on the employed two-phase CFD model will be given, followed by validation process with the above mentioned two experimental tests. Important conclusions obtained from the validation process will be summarized and discussed.

4.2.1 Overview of the employed two-phase CFD model

In order to describe the two-phase bubbly flow behavior in rod bundle geometry, the Eulerian two-fluid model (see chapter 4.1) was chosen. The liquid phase is modeled as continuous fluid, while the gaseous phase as disperse bubbles with constant bubble diameter. In the current study, both gaseous and liquid phase were set at saturation state and wall heat flux was zero, so that interphase mass and energy exchange are not needed. The interphase momentum exchange term was expressed by the interphase forces, for which the following models were chosen in the current study:

- Drag force (see Eq. 4.8): Ishii-Zuber model [35]
- Lift force (see Eq. 4.9): constant lift force coefficient C_L of 0.05 (see chapter 4.2.2 and 4.2.3)
- Wall lubrication force (see Eq. 4.11): Antal model [3]
- Turbulent dispersion force (see Eq. 4.15): Favre averaged drag force [12]

The virtual mass force (see Eq. 4.10) was not needed for the steady state simulations conducted in the current study. Regarding turbulence modeling, the $k-\epsilon$ two-equation turbulence model [50] with scalable wall function [see 2] was chosen for the continuous liquid phase, while the dispersed phase zero-equation model [see 2] was employed for the dispersed gaseous phase. Sato's model [76] was used to account the enhanced eddy viscosity of the continuous liquid phase through bubble movement. In this study, the choice of lift force model played a dominant role, since lift force acts perpendicularly to the main flow direction and is directly related to lateral movement of the gaseous phase. Therefore, interchannel mixing may be largely influenced by lift force. Unfortunately, up to now no generally applicable lift force model is available [see 71]. The widely used lift force model of Tomiyama [95] was established based on experimental studies conducted in pipe geometry. Hence its applicability to subchannels is questionable. In the current study, the lift force coefficient C_L was chosen as a constant based on a sensitivity study. Detail results will be described later in the validation calculation.

4.2.2 Validation calculation with van der Ros two-channel system

Test facility and selected test cases for validation calculation

The first validation calculation was conducted by recalculation of the two-phase interchannel mixing experiments carried out by van der Ros [101]. As depicted in Fig. 4.1, the test section consisted of two identical square subchannels laterally connected by a gap of 2 mm. The channel hydraulic diameter was about 10 mm, which is comparable to the hydraulic diameter

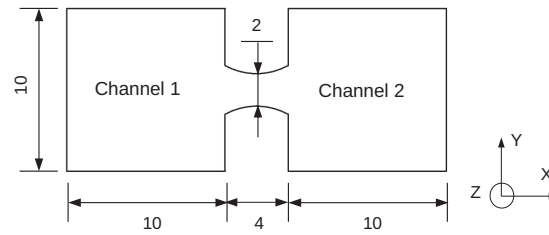


Fig. 4.1: Test section investigated by van der Ros [101] (dimension in *mm*). *Z* direction is the main streamwise direction.

of a typical subchannel in PWR fuel assembly^I. The two subchannels were connected over an axial (main streamwise) length of 1.85 *m* or 185 times of hydraulic diameter. Air-water two-phase system under atmospheric conditions was used as working fluid. Air injection possibility was provided over a streamwise length of 0.3 *m* at the inlet region from $Z = 0$ *m* to 0.3 *m*. Air flow was injected only to the Channel 2 (see Fig. 4.1) through a porous glass perpendicularly to the streamwise direction into the liquid flow in form of small bubbles. The diameter of the air bubbles was observed in the order of 1.0 *mm*. The average void fraction in the two subchannels were measured at five different axial (streamwise) elevations (0.28, 0.603, 0.923, 1.258 and 1.592 *m*) with impedance sensors. Pitot tubes were located at two axial locations (0.4 and 1.12 *m*), in order to detect the local average liquid phase velocity in the two subchannels.

Due to the feeding of air bubbles perpendicularly to the streamwise direction over a length of 300 *mm*, no clearly specified inlet boundary conditions could be defined in this range. Therefore, the inlet boundary for CFD simulation was set at the axial elevation of $Z = 0.4$ *m*, since the liquid phase velocities were measured at this location. With the interpolated average void fractions at the same axial location and the mass flow rate of the injected air bubbles^{II}, the gaseous phase velocities could be obtained at $Z = 0.4$ *m*. In this manner, inlet boundary conditions at the elevation $Z = 0.4$ *m* were clearly defined. A constant static pressure condition was specified at the outlet, which corresponds to the equal pressure discharging of the two-phase flow at the outlet as performed in the experiment. Of the 15 test cases performed with the 2 *mm* gap test section, six cases in the bubbly flow regime^{III} were selected for validation calculation, for which the inlet boundary conditions at $Z = 0.4$ *m* are summarized in Tab. 4.1.

Mesh sensitivity study

Mesh structure should provide an adequate resolution to capture geometrical details and flow phenomena in the computational domain. However, as the number of mesh elements is proportional to requirement of storage space and more importantly to computational time, a compromise between desired accuracy of numerical results and mesh number is inevitable in practical engineering applications.

Due to its good numerical accuracy and stability, block-structured grids was employed in the current study. Irregular blocks were defined on the coarse level, in order to capture the large characteristics of the geometrical domain. On the fine level, i.e. within each block, a

^IActually, a second test section with a gap clearance of 4 *mm* was also used by van der Ros. The choice of 2 *mm* gap test section for validation calculation was based on the fact that the ratio of gap clearance to subchannel hydraulic diameter is well close to that of a typical PWR fuel rod bundle.

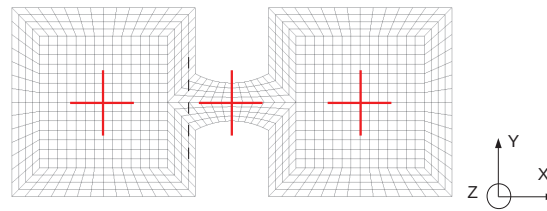
^{II}Based on the measured void fraction profiles in both subchannels, it was concluded that all the injected air flow was still in the injected Channel 2 at the axial elevation $Z = 0.4$ *m*.

^{III}As reported by van der Ros [101] that in his experimental study, bubbly flow regime was fairly established up to a void fraction of about 75%.

Tab. 4.1: Inlet conditions of the selected test cases conducted by van der Ros [101] with test section depicted in Fig. 4.1 for validation calculation

	Case VdR I		Case VdR II	
	Channel 1	Channel 2	Channel 1	Channel 2
Liquid velocity [<i>m/s</i>]	0.690	0.930	0.718	1.124
Void fraction [-]	0.0	0.220	0.0	0.371
Air velocity [<i>m/s</i>]	0.0	1.075	0.0	1.256
	Case VdR III		Case VdR IV	
	Channel 1	Channel 2	Channel 1	Channel 2
Liquid velocity [<i>m/s</i>]	0.805	1.143	0.886	1.385
Void fraction [-]	0.0	0.257	0.0	0.414
Air velocity [<i>m/s</i>]	0.0	1.369	0.0	1.627
	Case VdR V		Case VdR VI	
	Channel 1	Channel 2	Channel 1	Channel 2
Liquid velocity [<i>m/s</i>]	1.571	1.782	1.683	2.098
Void fraction [-]	0.0	0.262	0.0	0.428
Air velocity [<i>m/s</i>]	0.0	1.803	0.0	2.143

structured grid with hexahedral elements was used. A typical mesh structure used in the current study is displayed in Fig. 4.2. Since the $k-\epsilon$ turbulence model with wall function was used in the simulation, a local enhancement of mesh resolution in regions near to solid walls was required for a proper resolution of the wall shear layer, which can be assessed by a sensitivity study of the dimensionless wall distance y^+ with values normally between 30 and 100. Three

**Fig. 4.2:** Block topology and mesh structure approximating the test section investigated by van der Ros [101].

mesh structures with total nodes number (equal to the total number of the finite control volume in the CFX solver) of 23300, 42300 and 80280 were tested. The corresponding average dimensionless wall distance y^+ of the first near wall node were 55, 35 and 25, respectively. For consistency, the same block definition was adopted for all the mesh structures, whereas the mesh refinement was conducted within each block in both axial and radial direction simultaneously. Furthermore, the general recommendations for high quality grids as described in the best practice guideline [56] were adopted in generating all the mesh structures.

In order to ensure a proper convergence of the solutions, both residuals and global balances were monitored against the iteration steps during the simulation process, for which the convergence targets were at least 10^{-4} and 10^{-3} , respectively. Furthermore, characteristic target variables (void fraction and liquid phase velocity) on predefined points were also used to monitor the convergence. Three points, as depicted with red crosses in Fig. 4.2, two in the center of the subchannels and one in the connecting gap, were defined closely upstream of the domain outlet. For reduction of the spatial discretization error, the second order space discretization method (“high resolution” in the CFX solver [see 2]) as recommended in the best practice guideline [56] was used.

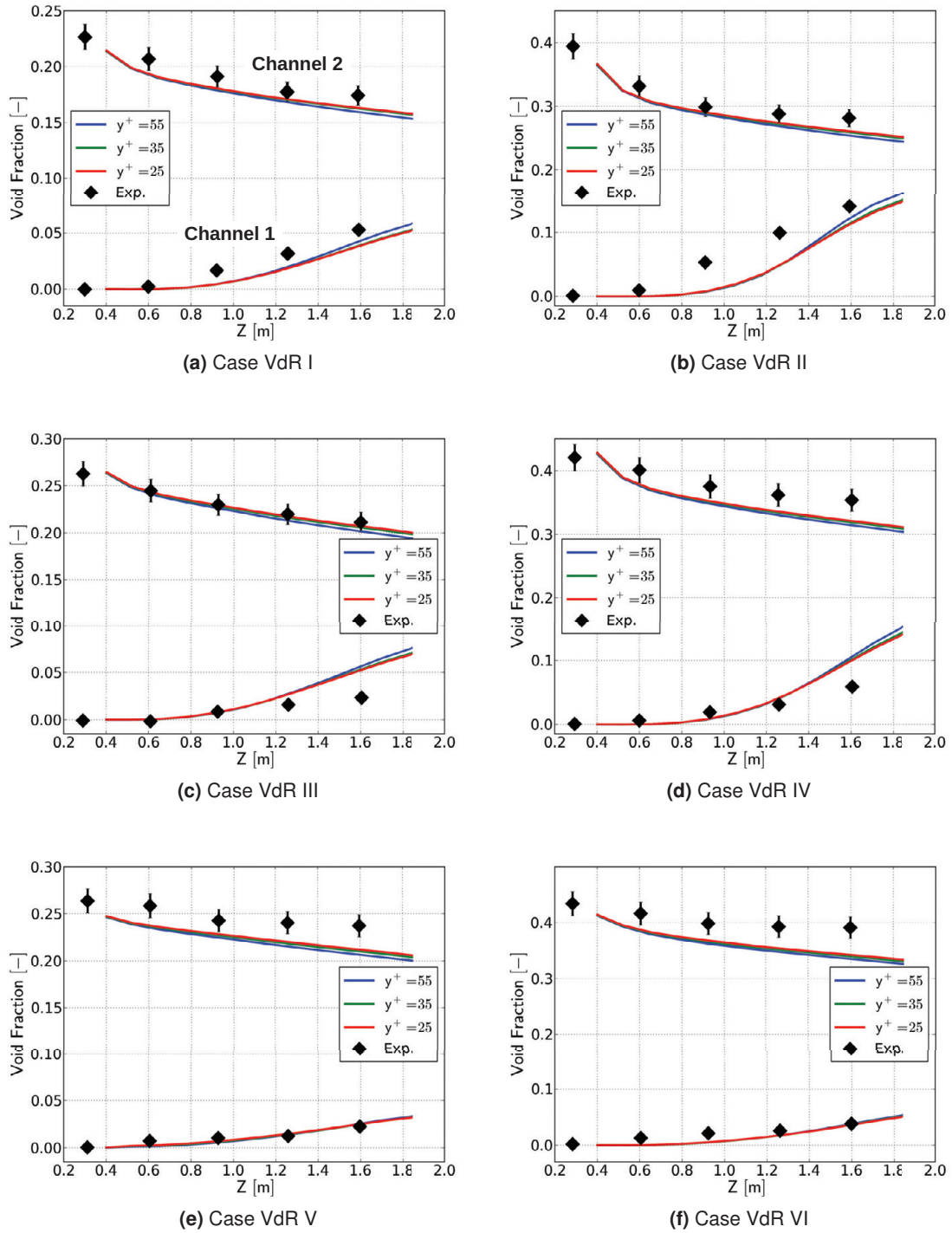


Fig. 4.3: Results of the mesh sensitivity study with the test cases summarized in Tab. 4.1; Z direction is the main streamwise direction.

In Fig. 4.3 the calculated void fractions in both Channel 1 and Channel 2 obtained with the three mesh structures are compared. The measured void fractions in both channels are also displayed for reference. In all the six test cases, Channel 2 was the subchannels with air injection at the inlet. Due to interchannel mixing, void fractions in the two subchannels tended to approach each other. As observed in Fig. 4.3, this interchannel mixing effect was well captured with all the three mesh structures. The average void fractions in both subchannels were predicted with an acceptable accuracy. It also reveals that the mesh structure with y^+

of 35 provided a good balance between numerical accuracy and computational effort. This mesh structure was hence chosen for further simulations.

Drag force study

Three drag force models are available in the CFX solver, namely Schiller Naumann model [78], Ishii Zuber model [35] and Grace model [see 19]. While the Schiller Naumann model is developed for sparsely distributed solid particles, it can also be applied for fluid particles such as bubbles at sufficiently low bubble Reynolds numbers, where bubbles behave in the same manner as spherical solid particles. Bubble Reynolds number Re_B is defined as:

$$Re_B = \frac{\rho_l \cdot |U_r| \cdot D_B}{\mu_l} \quad (4.39)$$

with $|U_r|$ denotes the absolute value of the relative velocity between the (dispersed) gaseous and the (continuous) liquid phase and D_B stands for the bubble diameter. For larger bubble Reynolds numbers, where bubbles become distorted in shape, the Ishii Zuber and the Grace model are recommended in the CFX solver. Nevertheless, in this chapter, all the three drag force models were tested. The mesh structure 2 with y^+ value of 35 was adopted. The same convergence criteria used in the mesh sensitivity study were also adopted, as well as all the models summarized in chapter 4.2.1 except the drag force model. Since drag force has close relation to velocity field, in Fig. 4.4 the calculated liquid phase velocities of both Channel 1 and 2 obtained with the three drag force models are compared with the measured values for cases VdR I and VdR VI. With all the three drag force models, an acceptable agreement between

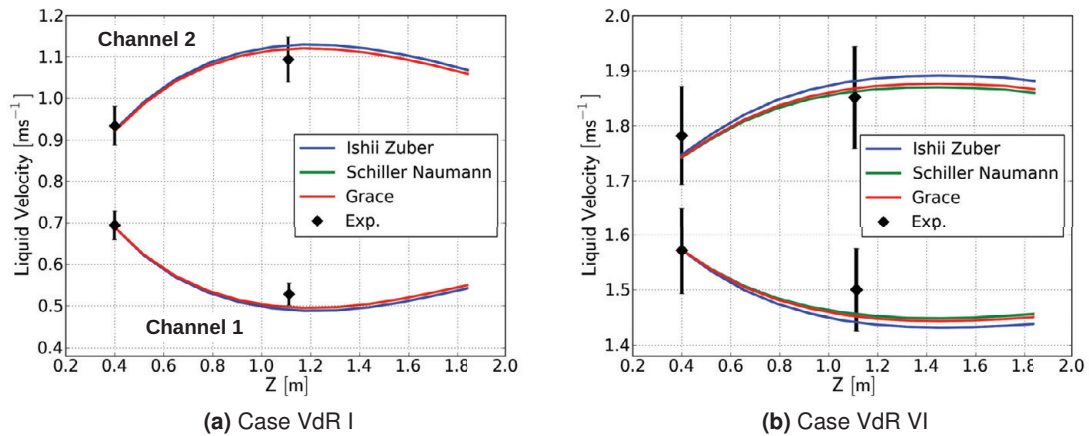


Fig. 4.4: Results of the drag force study with test cases summarized in Tab. 4.1; Z direction is the main streamwise direction.

the simulated and the measured liquid phase velocities was achieved for both subchannels. Furthermore, no large difference existed between simulation results obtained with the three drag force models. It can be concluded that the behavior of small bubbles (about 1 mm as reported by van der Ros [101]) at intermediate bubble Reynolds number range (less than 250 for all the selected six test cases in Tab. 4.1) can be well approximated with the Schiller Naumann model. Nevertheless, in the current study, the Ishii Zuber model was chosen as the standard model for drag force modeling. Compared to the Schiller Naumann model and the Grace model, it provides the largest application range from sparse to dense bubble distribution and considers also the effect of distorted bubble shape.

Lift force coefficient sensitivity study

Lift force acts laterally to the main streamwise direction and hence may relate directly to the lateral movement of bubbles between two interacting subchannels. Unfortunately, a generally applicable lift force model is currently not yet available. According to the widely applied model proposed by Tomiyama et al. [95], lift force can be separated into two regions depending on the bubble diameter. For small bubbles, lift force is induced by an inhomogeneous shear field exerted on bubbles by the surrounding continuous liquid phase. For large deformed bubbles, lift force is related to the presence of a slanted wake behind bubbles. The critical bubble diameter of transition from shear field controlled to slanted wake controlled lift force is found by Tomiyama et al. [95] for air-water system in the order of 4 mm to 6 mm. Since the bubble diameter reported by van der Ros [101] was about 1 mm, the lift force could be categorized as shear field controlled. In this range, Tomiyama et al. [95] found out that the lift force coefficient C_L can be well correlated with the bubble Reynolds number Re_B . The lift force coefficient C_L can be assumed as a constant except for very small bubble Reynolds numbers (smaller than 30 in the measurement conducted in [95]). As summarized by Rusche [71], typical values of C_L between 0.01 and 0.25 can be found in the open literature for small bubbles in shear field controlled range. In the present study, a sensitivity study with C_L varying from 0.01, 0.025, 0.05 to 0.1 was carried out. The mesh structure 2 with y^+ values of 35 was used exclusively. The same convergence criteria as described in the mesh sensitivity study was also adopted, as well as all models summarized in chapter 4.2.1 except the lift force model. In Fig. 4.5, results of the lift force coefficient sensitivity study is illustrated for all the six test cases. Similar to the mesh sensitivity study, the calculated void fraction in both Channel 1 and 2 were compared with the corresponding measured values.

As observed in Fig. 4.5, the predicted void fractions in both channels depend strongly on the lift force coefficient. With rising C_L value, the predicted interchannel mixing of the gaseous phase increases, so that more bubbles move from the injected Channel 2 towards Channel 1. In the test cases VdR I, VdR II, VdR V and VdR VI, the best agreement between measurement and simulation was achieved with C_L of 0.05, whereas in case VdR III and VdR IV the best prediction of void fraction in Channel 1 (with lower void fraction) was obtained with C_L of 0.025. With $C_L = 0.05$ the void fractions of Channel 1 were slightly overpredicted in cases VdR III and VdR IV. To sum up, with a constant lift force coefficient C_L of 0.05, the overall best agreement between measurement and simulation was achieved for all the six test cases. Thus C_L of 0.05 was chosen for simulations in the current study.

4.2.3 Validation calculation with Gonzalez-Santalo two-channel system

Test facility and selected test cases for validation calculation

Gonzalez-Santalo and Griffith [29] measured two-phase interchannel mixing in a two-channel system with air-water two-phase mixture under atmospheric conditions. In their test loop as schematic depicted in Fig. 4.6, inlet flows of air and water into each subchannels could be independently controlled and measured with separate flow meters (4 and 5 in Fig. 4.6). In order to prevent the effect of diversion cross flow, air and water flow rates in both subchannels were adjusted in such way, that the pressure levels along the entire axial length were the same in both channels, when the two channels were completely separated from each other (i.e., no interchannel exchange can occur). Then the separation between the subchannels was removed. Through a communication section of predefined length, typically varying from 57 mm to 387 mm, the gaseous and liquid phase will redistribute in the two subchannels. Since the initial pressure gradients and pressure levels were the same in both subchannels,

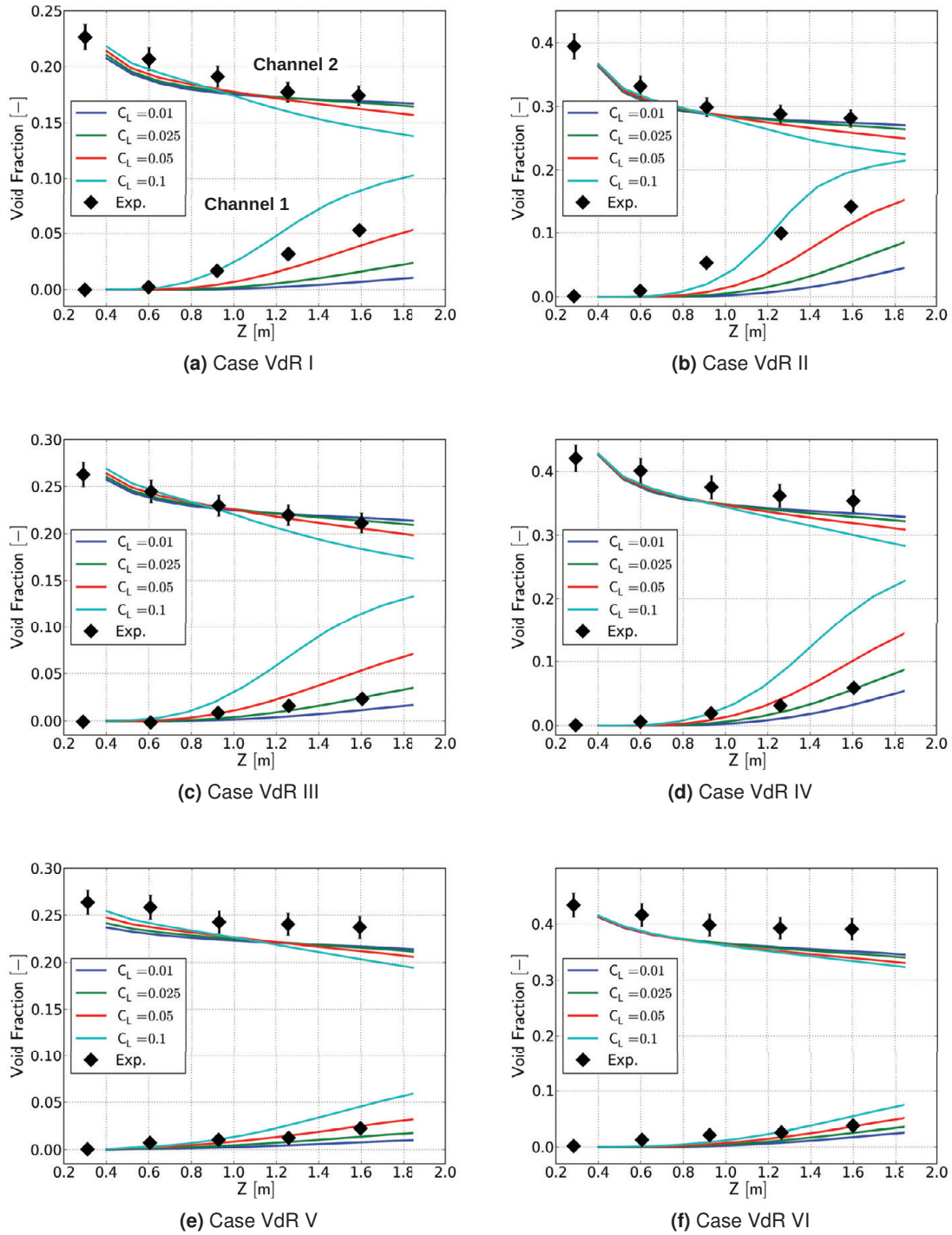


Fig. 4.5: Results of the lift force coefficient (C_L) sensitivity study with test cases in Tab. 4.1; Z direction is the main streamwise direction.

diversion cross flow was assumed to be eliminated by Gonzalez-Santalo and Griffith [29]¹ and

¹In opinion of the present author, a completely elimination of diversion cross flow is not possible, even in case that initial flow condition in both phase is equal pressure based. As flow redistribute in the subchannels, dissimilar flow conditions will be established in individual subchannels, which result in simultaneously a different frictional pressure drop. An equalization of this pressure difference due to diversion cross flow hence can not be prevented. This can also be seen in the data reduction procedure proposed by Gonzalez-Santalo and Griffith [29], where an equal pressure constraint was conducted to determine the liquid phase interchannel mixing flow rate.

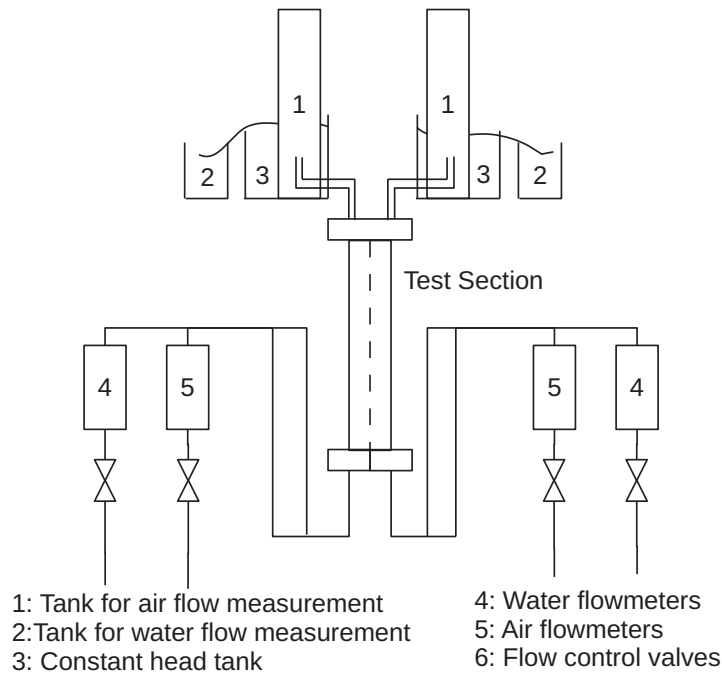


Fig. 4.6: Schematic illustration of the test loop used by Gonzalez-Santalo and Griffith [29].

the flow redistribution between the two subchannels was attributed purely due to turbulent mixing and void drift. At the exit of the test section, flow in both subchannels was split and discharged into two constant head tanks (3 in Fig. 4.6), in order to ensure an equal pressure level at the exit of the two subchannels. The two-phase air water mixture was then separated with help of gravity and collected in separate tanks (1 and 2 in Fig. 4.6). The outlet volumetric flow rates of both phases in individual subchannels were then determined as a function of the communication length by measuring the accumulated fluid volume at a given time interval. The estimated measurement error for air and water volumetric flow rate was reported as 5 and 2%, respectively [29].

Two of the three subchannel configurations used in the experiments are illustrated in Fig. 4.7, for which recalculations were carried out in the current study. Compared to that

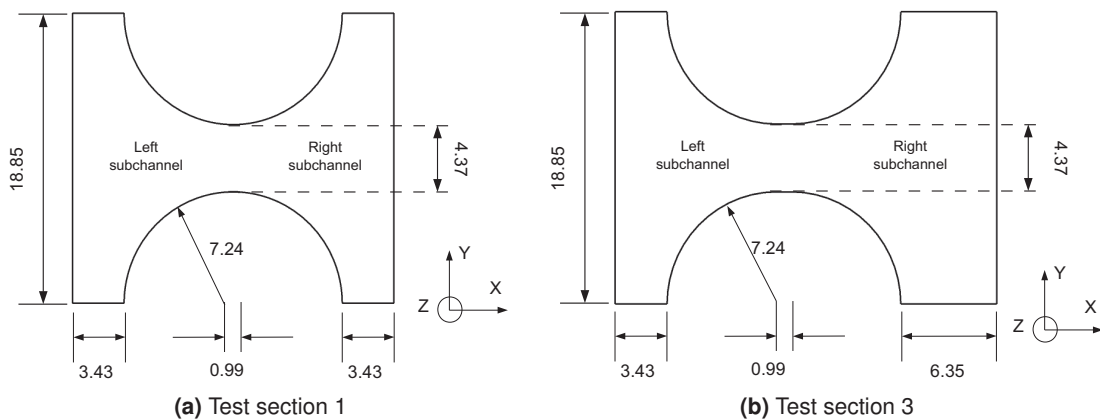


Fig. 4.7: Test section 1 and 3 used by Gonzalez-Santalo and Griffith [29] with dimension in *mm*; Z direction is the main streamwise direction.

of van der Ros [101] (see Fig. 4.1), the shape of the test section chosen by Gonzalez-Santalo and Griffith [29] was much closer to subchannels encountered in a rod bundle. Test section 1

corresponded to a wall-center subchannel combination with a cross-sectional area difference. The average hydraulic diameter of test section 1 was about 11.3 mm. Test section 3 consisted of two subchannels of the same dimension with hydraulic diameter of about 9.8 mm.

From the measured volumetric flow rate, superficial velocities of water and air could be calculated. According to the flow regime map proposed by Mishima and Ishii [57], of all the 39 performed test cases (32 with the test section 1 and seven with the test section 3) three test cases were located in the bubbly flow regime: RUN 5 as well as RUN 19 with the test section 1 and RUN 39 with the test section 3. These three test cases were hence selected for validation purpose. For a proper definition of inlet boundary conditions, phase velocity and void fraction are required in the CFX solver. Unfortunately this information was not provided in [29]. Therefore, they must be estimated in a proper way. This was done in two steps. First with the superficial velocities of both phases j_g and j_l , the flow quality x was calculated as:

$$x = \frac{\rho_g j_g}{\rho_g j_g + \rho_l j_l} \quad (4.40)$$

with ρ_g and ρ_l the density of air and water, respectively. In the second step, empirical quality-void correlations were used to estimate the void fraction α . Finally, the phase velocities u_g and u_l could be obtained with:

$$u_g = \frac{j_g}{\alpha} \quad (4.41)$$

$$u_l = \frac{j_l}{1 - \alpha} \quad (4.42)$$

Three empirical quality-void correlations were used in the current study: Smith model [84], Chisholm model [18] and the modified Armand model [see 86]. For all the three selected test cases, the deviation of the estimated void fractions with the three quality-void correlations was less than 3%. In the current study, the Smith model was used for providing the inlet phase velocities and void fractions in CFD simulation. In Tab. 4.2, the inlet boundary conditions of the three selected test cases are summarized. Similar to the experiments performed by van der Ros [101], air flow was injected only to one subchannel.

Tab. 4.2: Inlet conditions of selected test cases of [29] for validation calculation

RUN 5		
	Left Channel	Right Channel
Void fraction [-]	0.0	0.292
Liquid velocity [m/s]	0.860	1.831
Air velocity [m/s]	0.0	2.418
RUN 19		
	Left Channel	Right Channel
Void fraction [-]	0.0	0.239
Liquid velocity [m/s]	1.085	2.000
Air velocity [m/s]	0.0	2.491
RUN 39		
	Left Channel	Right Channel
Void fraction [-]	0.0	0.323
Liquid velocity [m/s]	0.981	1.655
Air velocity [m/s]	0.0	2.272

Mesh sensitivity study

Mesh sensitivity study was carried out with the test case RUN 39. All CFD models presented in chapter 4.2.1 were adopted here. Since no information of bubble diameter was documented by Gonzalez-Santalo and Griffith [29], a bubble diameter of 2 mm was assumed in the mesh sensitivity study. A detailed bubble diameter sensitivity study will be discussed later on. With experiences of the mesh sensitivity study obtained in chapter 4.2.2, block-structured meshes were employed to approximate the two-channel geometry as illustrated in Fig. 4.7. A typical mesh structure is depicted in Fig. 4.8. For a proper performance of the $k-\epsilon$ turbulence model with wall function, a local enhancement of the mesh resolution in regions near to solid walls was conducted. Three mesh structures with the same block topology but different cell numbers, i.e. 44175, 79821 and 150605, were tested. The corresponding y^+ of the first near wall node were 66, 25 and 16, respectively. In Fig. 4.9, the air and water volumetric flow rates obtained with the three different mesh structures are compared with the measured results. With all the three mesh structures, the gaseous phase distribution in both subchannels was

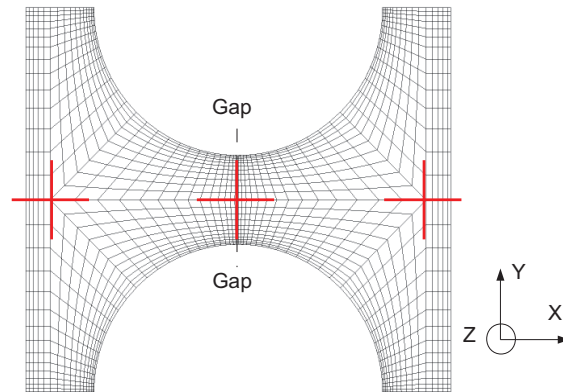


Fig. 4.8: Block topology and mesh structure describing the test section 3 used by Gonzalez-Santalo and Griffith [29]; Z direction is the main streamwise direction.

well predicted. No remarkable difference was observed in results with the different mesh resolutions. However, deviation between simulation and measurement was observed in prediction of the liquid phase volumetric flow rate. The maximum deviation was about 15%. Nevertheless, a good compromise between prediction accuracy and numerical effort was achieved with the mesh structure 2 with y^+ of 25. This mesh structure was used for further validation calculations.

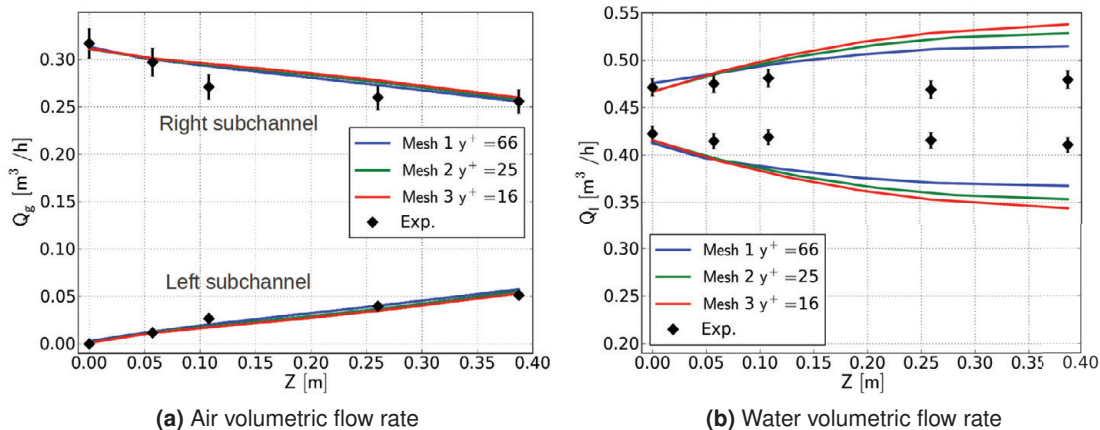


Fig. 4.9: Mesh sensitivity study with RUN 39 in Tab. 4.2; Z direction is the main streamwise direction.

well predicted. No remarkable difference was observed in results with the different mesh resolutions. However, deviation between simulation and measurement was observed in prediction of the liquid phase volumetric flow rate. The maximum deviation was about 15%. Nevertheless, a good compromise between prediction accuracy and numerical effort was achieved with the mesh structure 2 with y^+ of 25. This mesh structure was used for further validation calculations.

Drag force study

Similar to the sensitivity study in chapter 4.2.2, three drag force models, namely the Schiller Naumann model [78], the Ishii Zuber model [35] and the Grace model [see 19], were used for recalculating RUN 39. All the CFD models listed in chapter 4.2.1 were used except the drag force model. Results are depicted in Fig. 4.10. No large deviation between simulation results

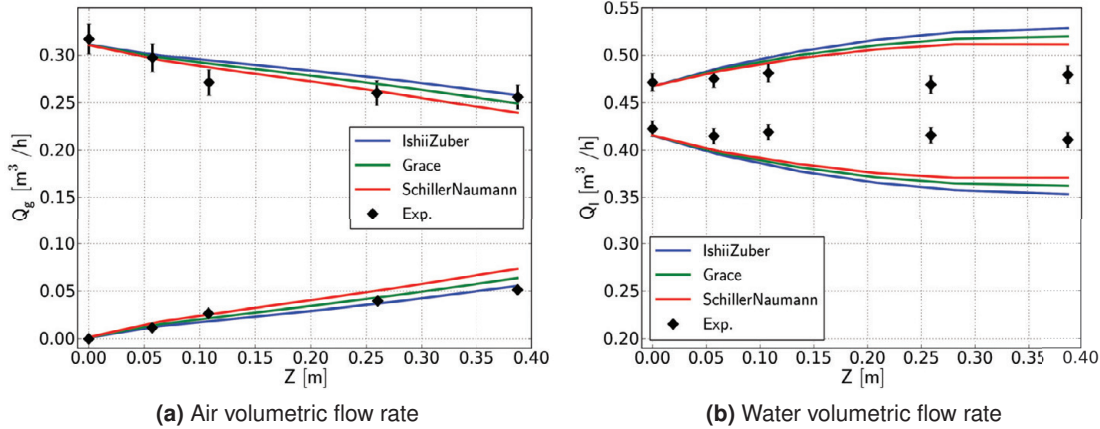


Fig. 4.10: Drag force study with RUN 39 in Tab. 4.2; Z direction is the main streamwise direction.

obtained with the three different drag force models could be observed. Overall, with the Ishii Zuber model the best prediction accuracy of the measured gaseous phase distribution was achieved. This confirms that the choice of the Ishii Zuber model as the standard drag force model in chapter 4.2.1 is appropriate.

Lift force coefficient sensitivity study

A sensitivity study of the lift force coefficient C_L was carried out for the three selected test cases as summarized in Tab. 4.2. All the CFD models in chapter 4.2.1 were employed except the lift force coefficient, which is varied in the current study from 0.01, 0.025, 0.05, 0.1 to 0.2. The results are depicted in Fig. 4.11, where the air and water volumetric flow rates in subchannels are plotted versus the axial (main streamwise) communication length. The same effect of lift force on interchannel mixing can be observed here as that illustrated in Fig. 4.5. With an increasing value of C_L , interchannel mixing of the gaseous phase amplifies. This leads to a larger net air exchange from the injected subchannel towards the non-injected subchannel. Similar to the observation made in Fig. 4.5, with a constant lift force coefficient C_L of 0.05, the overall best prediction of phase distribution in the two subchannels was achieved. This confirms again that the choice of $C_L = 0.05$ in chapter 4.2.1 is reasonable.

Bubble diameter sensitivity study

One essential parameter required in the Eulerian two-fluid model is the bubble diameter. Unfortunately, information of the bubble diameter was not provided by Gonzalez-Santalo and Griffith [29]. Hence, the bubble diameter must be estimated in an appropriate manner. Since the subchannel dimension investigated by Gonzalez-Santalo and Griffith [29] was comparable

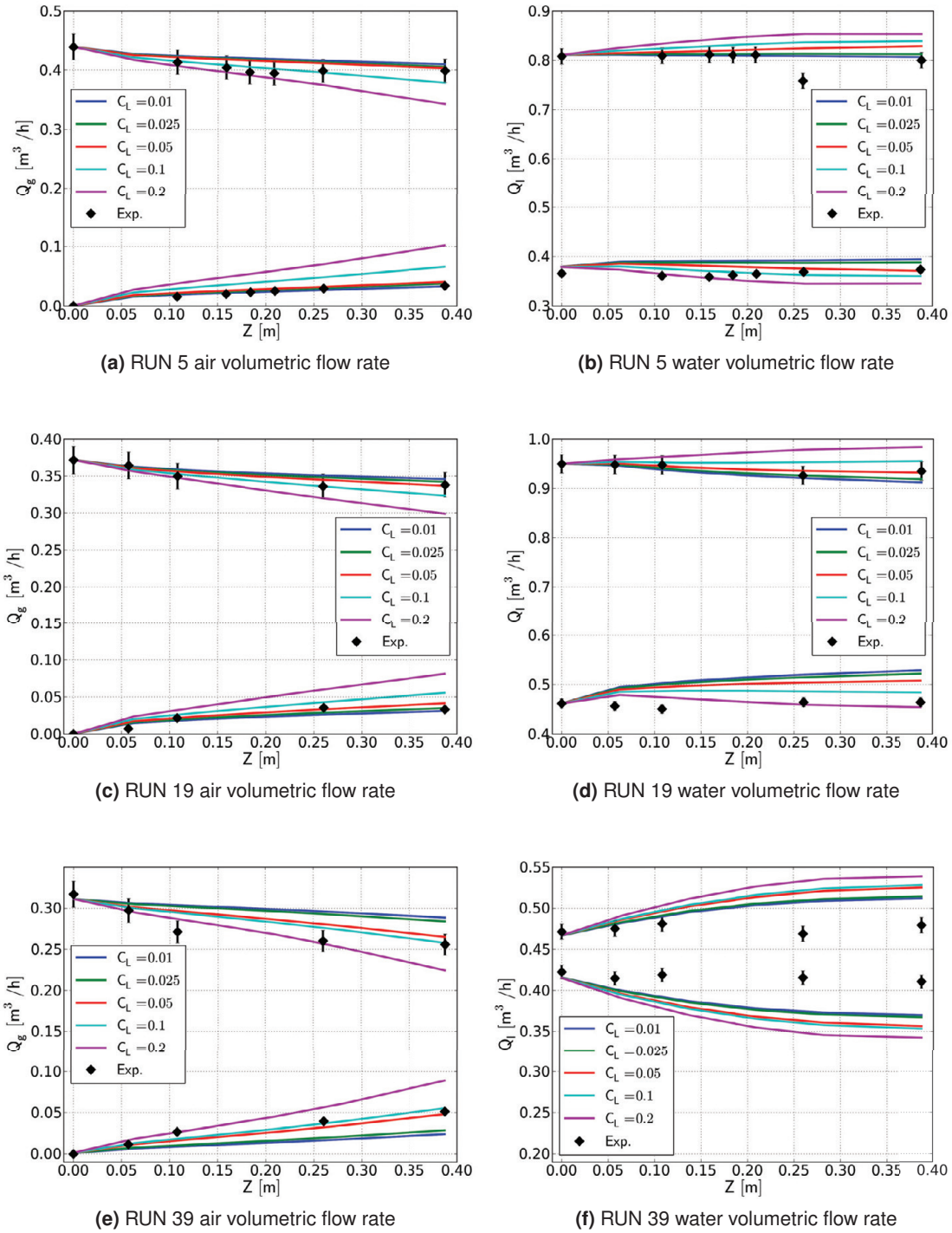


Fig. 4.11: Sensitivity study of the lift force coefficient C_L with test cases in Tab. 4.2; Z direction is the main streamwise direction.

with that of van der Ros [101], the reported bubble diameter of 1 mm by van der Ros was taken as a reference value. As the lift force coefficient has large influence on predicting interchannel mixing, the first simulations were performed with bubble diameter of 1 mm and varying C_L from 0.01, 0.025, 0.05, 0.1, 0.2 towards 0.5. Different to the lift force coefficient sensitivity study, a further C_L value of 0.5 was included in the simulation. At high bubble Reynolds numbers, the choice of 0.5 is classic for the lift force coefficient (see for instance in [36]), which corresponds to the case of a spherical bubble in weakly sheared inviscid flow [see 71]. As also

shown in [71], in shear field controlled range, C_L approaches the constant value of 0.5 and is always smaller than 0.5 except for bubble Reynolds numbers smaller than unity. Therefore, 0.5 was chosen as the upper limit of C_L in the current study. In Fig. 4.12, the results are plotted for the bubble diameter of 1 mm. The same trend of rising interchannel mixing with increasing

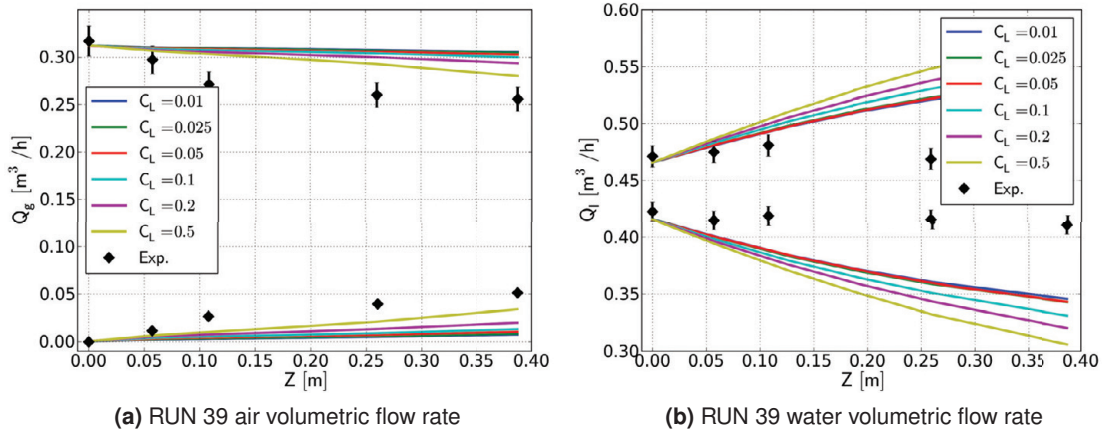


Fig. 4.12: Sensitivity study of the lift force coefficient C_L with bubble diameter of 1 mm for RUN 39 in Tab. 4.2.

C_L can be observed. With larger C_L values, prediction of the gaseous phase distribution in the subchannels was improved. However, even with the largest lift force coefficient of 0.5, no acceptable agreement with the measurement results could be achieved. For predicting the liquid phase distribution C_L of 0.5 gave the worst performance. These observations revealed that probably the choice of bubble diameter of 1 mm is not appropriate.

A sensitivity study of the bubble diameter was therefore performed for three bubble diameters: i.e. 1, 2 and 3 mm. The lift force coefficient C_L was kept constant of 0.05. Results are shown in Fig. 4.13. It reveals that with the bubble diameter of 2 mm, the best agreement with

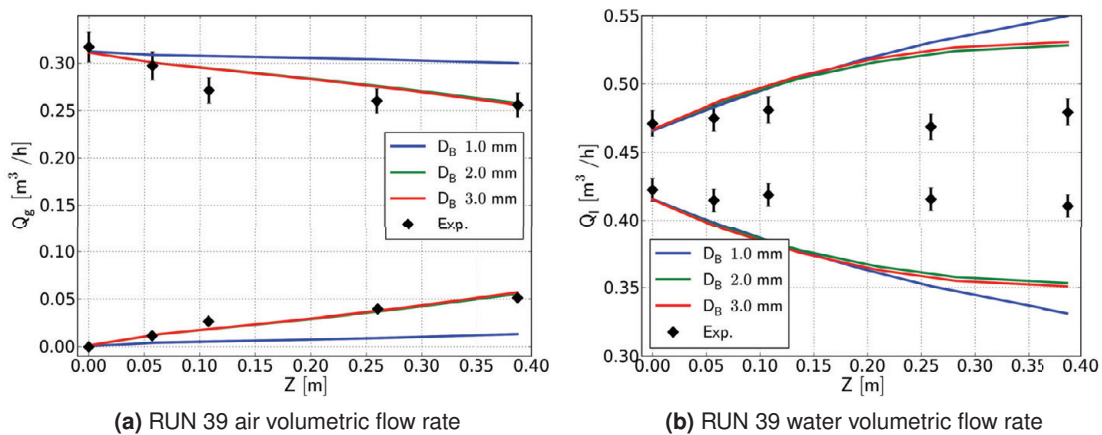


Fig. 4.13: Sensitivity study of bubble diameter with RUN 39 in Tab. 4.2.

the measurement results was achieved. Furthermore, no large difference existed between simulation results obtained with the bubble diameters of 2 and 3 mm. However, due to the narrow subchannel size of about 10 mm, no larger bubble diameters than 3 mm were tested in the current study.

4.2.4 Conclusion and discussion

The validation calculation in this chapter demonstrates the capability of the employed two-phase CFD models in chapter 4.2.1 to predict two-phase interchannel mixing in the bubbly flow regime. Lateral transport of the gaseous phase between two interacting subchannels due to interchannel mixing can be reasonably predicted. This is seen in the validation calculations of the experiments conducted by van der Ros [101] and Gonzalez-Santalo and Griffith [29]. However, interchannel transport of the liquid phase measured by Gonzalez-Santalo and Griffith [29] is failed to be predicted by the CFD simulations conducted in the current study. CFD simulations performed in this chapter indicate an interchannel mixing of the gaseous phase from the injected subchannel to the non-injected subchannel and an simultaneous interchannel mixing of the liquid phase in the opposite direction. This kind of trend was also observed in experiments conducted by van der Ros [101]. However, in the measurement conducted by Gonzalez-Santalo and Griffith [29], despite considerable interchannel mixing of the gaseous phase, negligible interchannel mixing of the liquid phase was measured. As seen in Fig. 4.9 (b), the measured liquid phase volumetric flow rates in both subchannels remain almost constant for all the communication lengths. This trend is failed to be predicted with the conducted simulations. Possible reason may be due to the fact that measurement of the volumetric flow rates in the case of Gonzalez-Santalo and Griffith [29] was performed after an equal pressure discharge at the domain outlet, while in the case of van der Ros [101], measurement of the liquid phase velocity was conducted in the middle of the test section (at $Z = 1.12m$ compared to the test section outlet at $Z = 1.85m$). Perhaps the equal pressure discharge at the outlet has large effects on the interchannel mixing of the liquid phase. Future investigation should be conducted.

Furthermore, due to lacking of three-dimensional measurement results on two-phase interchannel mixing phenomena, validation of CFD models was conducted on the basis of subchannel average parameters, i.e. one-dimensional flow parameters in the main streamwise direction. As three-dimensional measurement results, such as void fraction profile, phase velocity profile as well as bubbly diameter distribution in the lateral direction and turbulence quantities, become available in the future, more validation calculations of the CFD model summarized in chapter 4.2.1 should be carried out.

5. Simulation and analysis of two-phase interchannel mixing with CFD approach

With the validated set of CFD models from the previous chapter, a systematic study of the two-phase interchannel mixing covering typical PWR conditions was carried out. A modified phenomenological two-phase interchannel mixing model was proposed based on Lahey's assumption [47] of two-phase systems approaching an equilibrium state. Based on the CFD simulation results, both the void fraction distribution at equilibrium state and the effective mixing velocity due to void drift were determined.

5.1 Phenomenological description of two-phase interchannel mixing

From CFD simulation flow parameters of each finite control volume are determined. Subchannel scale flow parameters can be obtained by averaging flow parameters of the finite control volumes over the corresponding subchannel geometry. With this approach, the subchannel scale net interchannel mixing mass flow rate between two interacting subchannels can be easily obtained via mass conservation. For studying the void drift effect, which is only a part of the two-phase interchannel mixing, the net mixing mass flow rate must be decomposed into its elemental components, namely turbulent mixing (TM), diversion cross flow (DC) and void drift (VD). In Fig. 5.1, the three elemental interchannel mixing effects are illustrated for a segment of two laterally connected subchannels 1 and 2 with a finite axial height of ΔZ and a gap distance of S (not displayed in the figure). The arrows of the individual components denote that turbulent mixing (TM) has no prevailing direction, whereas diversion cross flow (DC) and void drift (VD) are both directional mixing effects.

The mass conservation¹ of the subchannel 1 is established for the gaseous phase and the liquid phase, respectively.

$$(j_{g,1}^{in} - j_{g,1}^{ex}) \cdot \rho_g \cdot A_1 = w_{1to2,g} \cdot \Delta Z \quad (5.1)$$

$$(j_{l,1}^{in} - j_{l,1}^{ex}) \cdot \rho_l \cdot A_1 = w_{1to2,l} \cdot \Delta Z \quad (5.2)$$

where j , ρ and A stand for the superficial velocity, density and cross-sectional area, respectively. The subscripts g and l denote the physical properties of the single gaseous and liquid phase, respectively. The inlet and outlet flow properties are then denoted with the superscripts in and ex , respectively. In both equations, the sums of the right hand side are the net interchannel mixing mass flow rate of the gaseous and liquid phase, respectively. For studying the interchannel mixing phenomena, it is essential to separate the net mixing mass flow rate in the three individual mixing effects.

¹Since the interphase mass exchange is not considered in the current study, no interphase mass exchange terms are specified in the mass conservation equations.

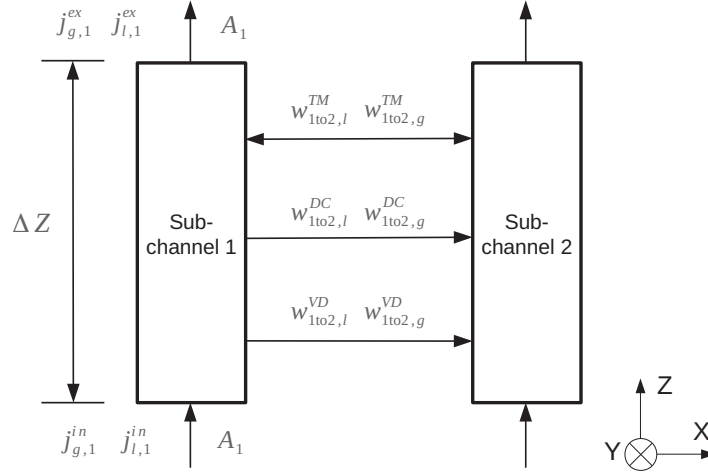


Fig. 5.1: Axial and lateral interchannel mass flows between two interacting subchannels 1 and 2; Z direction is the main streamwise direction.

$$w_{1to2,g} = w_{1to2,g}^{TM} + w_{1to2,g}^{DC} + w_{1to2,g}^{VD} \quad (5.3)$$

$$w_{1to2,l} = w_{1to2,l}^{TM} + w_{1to2,l}^{DC} + w_{1to2,l}^{VD} \quad (5.4)$$

For this purpose, appropriate assumptions must be taken. Imaging the case of the two subchannels 1 and 2 in a non-equilibrium state with differences in mean static pressure, mass flux and void fraction at the inlet boundary, the two-phase flow will mix through the connecting gap downstream to the outlet boundary. Regardless of whether an equilibrium state is established or not, turbulent mixing due to stochastic fluctuations is always present. Due to the static mean pressure difference, diversion cross flow is also induced. Furthermore, for a non-equilibrium void fraction distribution state, void drift should also be considered. In summary, all the three mixing effects coexist. By feeding the outlet flow back to the inlet boundary (similar to a cyclic boundary condition employed in CFD simulations), the streamwise subchannel length can be virtually extended. After a sufficient number of iterations, the void fraction distribution at the outlet will gradually converge to a fully developed, equilibrium state, where the mean pressure difference between the subchannels is canceled out and a constant void fraction distribution state is established. Under this condition the mixing effect due to both diversion cross flow and void drift ceases. Turbulent mixing remains as the only active mixing effect, which introduce neither net mass nor net volume exchanges between the two subchannels.

Based on the above discussion, the following assumptions were taken in the current study regarding the individual mixing effects:

- Turbulent mixing effect is assumed to be equal-mass based, i.e., in a time-averaging aspect no net mass exchange occurs due to turbulent mixing between two interacting subchannels. But a net momentum or energy transfer will be induced by turbulent mixing, if different velocities or temperatures exist in the two interacting subchannels.

$$w_{1to2,g}^{TM} = 0 \quad (5.5)$$

$$w_{1to2,l}^{TM} = 0 \quad (5.6)$$

- Diversion cross flow contributes to an equalization of the mean pressure difference between two interacting subchannels. This directional mixing effect causes a net exchange

of mass, momentum and also energy between two interacting subchannels. Therefore, the effective mixing velocity due to diversion cross flow u_{DC} can be related to the mean pressure difference between the two interacting subchannels (see Eq. 3.21) as:

$$\Delta p = p_1 - p_2 \propto \frac{1}{2} \cdot \rho_{donor} \cdot u_{DC}^2 \quad (5.7)$$

with the density ρ_{donor} is taken as the average density of the donor subchannel [47]. Assuming the subchannel 1 as the donor subchannel leads to (see Eq. 3.1):

$$\rho_{donor} = \rho_1 = \rho_g \cdot \alpha_1 + \rho_l \cdot (1 - \alpha_1)$$

The lateral mass flow due to diversion cross flow is hence a two-phase mixture flow, which can be further split to a gaseous and a liquid part as¹:

$$w_{1to2,g}^{DC} = \alpha_1 \cdot \rho_g \cdot u_{DC} \cdot S \quad (5.8)$$

$$w_{1to2,l}^{DC} = (1 - \alpha_1) \cdot \rho_l \cdot u_{DC} \cdot S \quad (5.9)$$

Therefore, the gaseous and liquid part of the diversion cross flow has a clear relation with each other:

$$\frac{w_{1to2,g}^{DC}}{w_{1to2,l}^{DC}} = \frac{\alpha_1 \cdot \rho_g}{(1 - \alpha_1) \cdot \rho_l} \quad (5.10)$$

- In the bubbly flow regime with relative lower void fractions, void drift can be modeled as a diffusion process of the dispersed bubbles from a non-equilibrium state to an equilibrium state. Hence it is plausible to assume, that in bubbly flow regime, void drift concerns only the movement of the dispersed gaseous bubbles between interacting subchannels. Therefore, the net interchannel liquid phase flow due to void drift is zero.

$$w_{1to2,l}^{VD} = 0 \quad (5.11)$$

With the above assumptions, mass conservation equations of the subchannel 1, i.e. Eq. 5.1 and 5.2, can be simplified to:

$$(j_{g,1}^{in} - j_{g,1}^{ex}) \cdot \rho_g \cdot A_1 = (w_{1to2,g}^{DC} + w_{1to2,g}^{VD}) \cdot \Delta Z \quad (5.12)$$

$$(j_{l,1}^{in} - j_{l,1}^{ex}) \cdot \rho_l \cdot A_1 = w_{1to2,l}^{DC} \cdot \Delta Z \quad (5.13)$$

Eq. 5.10, 5.12 and 5.13 builds up an equation system, with which the void drift mass flow rate per axial length $w_{1to2,g}^{VD}$ can be determined. This yields:

$$w_{1to2,g}^{VD} = \rho_g \cdot \left[(j_{g,1}^{in} - j_{g,1}^{ex}) - \frac{\alpha_1}{(1 - \alpha_1)} \cdot (j_{l,1}^{in} - j_{l,1}^{ex}) \right] \frac{A_1}{\Delta Z} \quad (5.14)$$

This equation will be used later in the present study (chapter 5.3.2) to determine $w_{1to2,g}^{VD}$ from CFD simulation results. In the above proposed interchannel mixing model, the equal-mass turbulent mixing is considered together with the void drift effect, it is henceforth referred to as the equal-mass turbulent mixing and void drift (EMVD) model.

5.2 Description of the modified void drift model

In order to provide a constitutive model of void drift for subchannel analysis, Lahey's proposal [47] of a two-phase system approaching an equilibrium state of void fraction distribution was

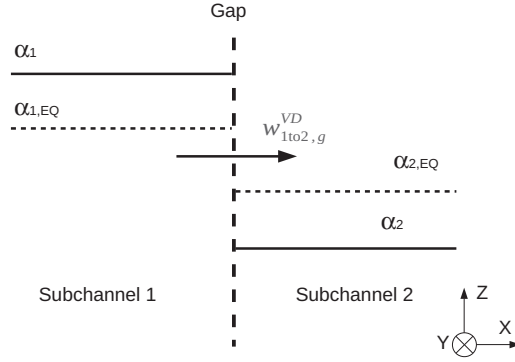


Fig. 5.2: Schematic description of void drift process.

adopted in the current study to describe the effect of void drift in the bubbly flow regime. As depicted in Fig. 5.2, the existing void fractions and the void fractions at the equilibrium state in two laterally connected subchannels are denoted with α_1 , α_2 and $\alpha_{1,EQ}$, $\alpha_{2,EQ}$, respectively. Similar to a diffusion process, the void drift mass flow rate per axial length $w_{1to2,g}^{VD}$ is proportional to the non-equilibrium void fraction gradient. This yields:

$$w_{1to2,g}^{VD} = \tilde{D}_{VD} \cdot \rho_g \cdot S \cdot \frac{(\alpha_1 - \alpha_2) - (\alpha_1 - \alpha_2)_{EQ}}{\Delta X} \quad (5.15)$$

with \tilde{D}_{VD} similar to a diffusion coefficient characterizing the velocity of the process and ΔX has the similar meaning of a mixing length. Instead of providing correlations for \tilde{D}_{VD} and ΔX , the two unknown terms were combined in the current study to a velocity term, which was further correlated with the average main streamwise velocity of the two interacting subchannels U_{avg} , by introducing a dimensionless factor. This yields:

$$\frac{\tilde{D}_{VD}}{\Delta X} = \beta_{VD} \cdot U_{avg} \quad (5.16)$$

β_{VD} is henceforth referred to as the void drift coefficient, with which $w_{1to2,g}^{VD}$ is finally expressed as:

$$w_{1to2,g}^{VD} = \beta_{VD} \cdot U_{avg} \cdot \rho_g \cdot S \cdot [(\alpha_1 - \alpha_2) - (\alpha_1 - \alpha_2)_{EQ}] \quad (5.17)$$

Two key parameters are required to describe the void drift phenomena in bubbly flow regime, namely the void drift coefficient β_{VD} characterizing the effective void drift velocity and the void fraction difference at equilibrium state $(\alpha_1 - \alpha_2)_{EQ}$. For subchannel analysis, both parameters must be modeled with constitutive equations. In subsequent chapters, CFD analysis will be employed to determine these two key parameters.

5.3 Simulation and analysis of void drift with two-phase CFD approach

In the current study, CFD simulation and analysis were performed to investigate the two-phase interchannel mixing in a PWR rod bundle. Since improvement demands of the void drift models currently available in MATRA were found in the bubbly flow regime under PWR pressure levels (see chapter 3.3), only bubbly two-phase flow behaviors will be considered in the CFD simulations. For describing a bubbly two-phase flow, the validated Eulerian two-fluid models

¹The splitting implies that the gaseous and liquid part of the diversion cross flow have the same effective mixing velocity. Since the two parts have the same driving force and the same direction, this assumption is plausible.

as summarized in chapter 4.2.1 were employed in the current study. Steam-water two-phase system under the typical PWR pressure level (157 bar) and the corresponding saturation temperature (345.82 °C) was used as working fluid. Water was modeled as continuous liquid phase, while steam as dispersed bubbly phase with a constant bubble diameter of 2 mm¹. All the physical properties of the steam-water two-phase mixture summarized in Tab. 5.1 were taken from the NIST Chemistry web book [53].

Tab. 5.1: Physical properties of the investigated water-steam two-phase system under 157 bar and 345.82 °C

	Water	Steam
Density [kgm^{-3}]	590.66	104.09
Viscosity [$kgm^{-1}s^{-1}$]	$6.7856 \cdot 10^{-5}$	$2.3239 \cdot 10^{-5}$
Surface tension [Nm^{-1}]	0.004467	

In order to reduce numerical efforts, two adjacent subchannels of a square rod bundle were chosen as the geometrical model representing a PWR rod bundle. In a square rod bundle, the dominant subchannel combinations are: (1) a center subchannel interacting with a center subchannel and (2) a center subchannel interacting with a wall subchannel. The case of a wall subchannel interacting with a corner subchannel plays a less important role due to the relative smaller numbers of corner subchannels. Therefore, in the current study only the two major subchannel combinations were investigated: namely center-center and wall-center subchannel combinations as depicted in Fig. 5.3. The rod outer diameter D was set as 9.5 mm

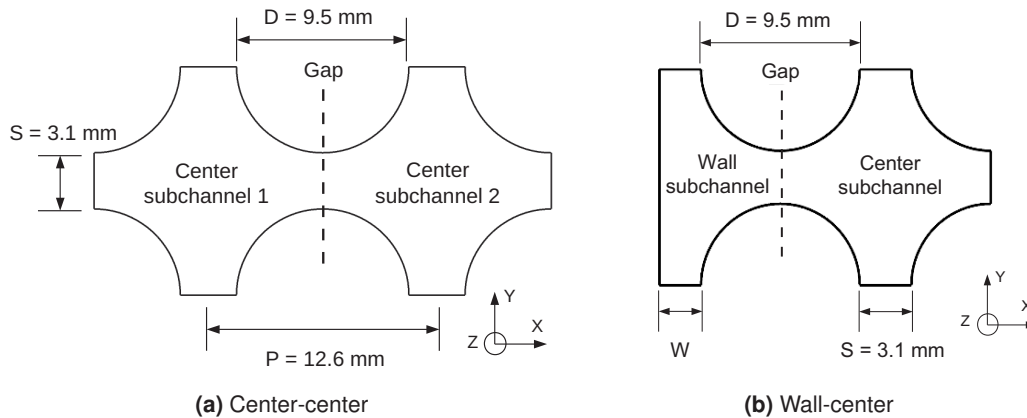


Fig. 5.3: Cross-sectional view of the two investigated subchannel combinations: (a) center-center subchannel combination and (b) wall-center subchannel combination.

and the pitch distance P as 12.6 mm, so that the gap clearance S is 3.1 mm. The choice of D and P was made coinciding with fuel assembly designs of typical PWRs [see 81, 94]. The rod to wall distance W will be discussed later in chapter 5.3.1.

¹The choice of the bubble diameter was based on an estimation, since no measurement results of the bubble diameter under PWR conditions are available in the open literature. Difficulties arise due to the very narrow channels of about 10 mm, where the size of the bubbles is expected in the range between 0.5 and 2 mm [see 44]. For typical nuclear engineering applications, Kurul et al. [46] and Anglart et al. [1] proposed reference bubble diameters under two reference subcooling conditions: $D_B = 0.1$ mm at $T_{sub} = 13.5$ K and $D_B = 2$ mm at $T_{sub} = 5$ K. As the working fluid was set under the saturation condition in the present study, i.e. $T_{sub} = 0$ K, the choice of 2 mm bubble diameter is reasonable.

5.3.1 Void fraction distribution at equilibrium state

As discussed in chapter 2, void fraction distribution at equilibrium state could be dependent both on mass flux distribution and geometrical difference of two interacting subchannels. Therefore, two set of simulations were conducted to study the mass flux effect and the geometrical effect, respectively. In this chapter, both effects will be at first separately investigated. Then the superposition of the two effects will be discussed.

Mass flux effect

In this set of simulation, the influence of mass flux distribution on the void fraction distribution at equilibrium state was investigated. In order to eliminate possible effects of the geometrical difference, the two adjacent center subchannels as depicted in Fig. 5.3 (a) with the same geometrical dimension were chosen as geometrical domain. Establishment of an fully developed, equilibrium state requires theoretically a calculation domain with an infinite length in the main streamwise direction, which is numerically not feasible. Instead of that the axial (main streamwise) length of the calculation domain was set at ten times of the hydraulic diameter of a center subchannel. Cyclic boundary condition was employed, in order to achieve the fully developed, equilibrium state. The boundary conditions are depicted in Fig. 5.4. To study the

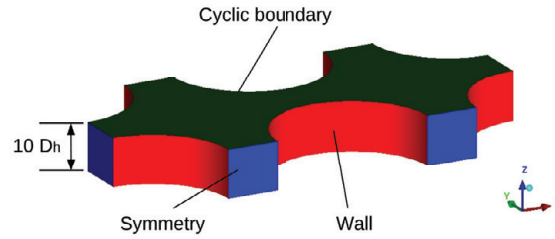


Fig. 5.4: Boundary conditions for determination of the mass flux effect on void fraction distribution at equilibrium state.

influence of mass flux distribution on the void fraction distribution at equilibrium state, different mass flux levels should be established in the two interacting subchannels. This was realized by increasing the solid wall roughness of the center subchannel 1 (see Fig. 5.3 (a)), while the same initial conditions (void fraction, phase velocity) were set in the two subchannels. The difference in wall roughness led to different frictional pressure drops, different velocity fields and hence different mass flux distributions in the two subchannels. For a mathematical description of the mass flux effect, a simple relation similar to that used in MATRA (see Eq. 3.55) was adopted in the current study:

$$\frac{(\alpha_1 - \alpha_2)_{EQ}}{\alpha_{avg}} = K_1 \cdot \frac{(G_1 - G_2)_{EQ}}{G_{avg}} \quad (5.18)$$

This relation correlates the void fraction difference with the mass flux difference with a proportional factor K_1 . It implies that for two identical subchannels with the same mass flux, the void fraction at equilibrium state must be the same in the two subchannels.

In order to cover a wide parameter range, simulations were conducted with three average mass flux levels of 2250, 3375 and 4500 $kgm^{-2}s^{-1}$ and five average void fraction levels of 5, 10, 15, 20 and 25%. For each combination of G_{avg} and α_{avg} , three different wall roughness levels of the subchannel 1 were used, so that three relative mass flux differences of 5, 10 and as large as 20% between the two subchannels were achieved. In all, 45 cases were simulated to determine the proportional factor K_1 with dependence on the average void fraction α_{avg} and

the average mass flux G_{avg} of the two interacting subchannels:

$$K_1 = K_1(\alpha_{avg}, G_{avg}) \quad (5.19)$$

The validated two-phase CFD models as described in chapter 4.2.1 were used in this set of simulations. In Fig. 5.5 a typical mesh structure used in the simulation is depicted. For

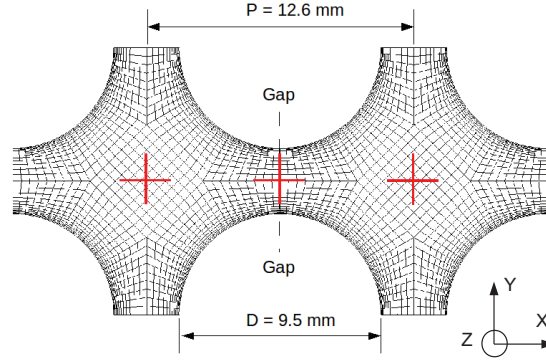


Fig. 5.5: Block topology and mesh structure of the investigated two-channel system consisting of two interacting center subchannels; Z direction is the main streamwise direction.

estimation of the spatial discretization error, a mesh sensitivity study was performed for the case of average mass flux of $4500 \text{ kgm}^{-2}\text{s}^{-1}$ and average void fraction of 10%. The enhanced wall roughness was kept constant for all the tested meshes. Three meshes with total cell number of 25164, 89376 and 215475 were tested. The corresponding average dimensionless wall distance y^+ of the first near wall node were 120, 60 and 30, respectively. The mesh sensitivity study revealed the mesh structure of total node number 89376 and the average y^+ of 60 provides a good compromise between numerical accuracy and effort. This mesh was hence used for further simulations studying the mass flux effect.

In Fig. 5.6, the void fraction difference at equilibrium state is plotted against the mass flux difference between the two subchannels for two average mass flux levels of $2250 \text{ kgm}^{-2}\text{s}^{-1}$, $4500 \text{ kgm}^{-2}\text{s}^{-1}$ and two average void fractions of 10%, 20%. As shown in Fig. 5.6, a fairly

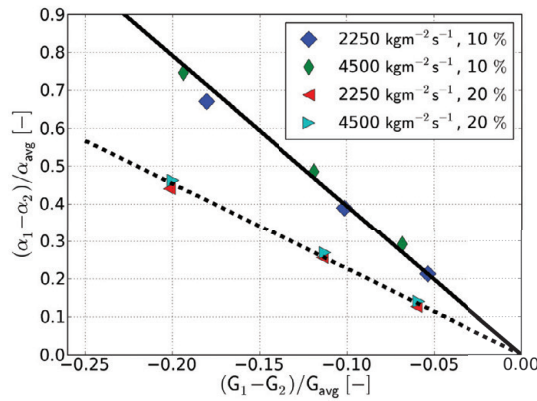


Fig. 5.6: Dependence of void fraction distribution at equilibrium state on mass flux distribution in two interacting subchannels.

good linear relationship crossing the origin point between the void fraction difference at equilibrium state and the mass flux difference can be obtained. Furthermore, the average mass flux level shows a negligible influence on the proportion factor K_1 , while K_1 depends strongly on the average void fraction in the two subchannels. Based on the above discussion, K_1 was

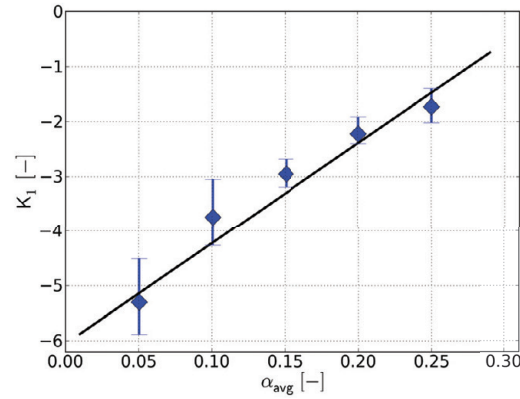


Fig. 5.7: Factor K_1 correlated with the average void fraction of two interacting subchannels.

correlated with the average void fraction α_{avg} as depicted in Fig. 5.7. The data points denoted the average values of K_1 at each average void fractions, while the bars gave the then the range of K_1 . A good linear dependence of K_1 on α_{avg} could be established. This yields:

$$K_1 = 18.323 \cdot \alpha_{avg} - 6.061 \quad (5.20)$$

Geometrical effect

The effect of geometrical difference refers to the influence of different geometrical configurations of two interacting subchannels on the void fraction difference at equilibrium state. In a rod bundle this effect occurs in a wall-center or a corner-wall subchannel combination. Since the total number of wall subchannels is normally much larger than that of corner subchannels, in the current study only the combination of a wall subchannel interacting with a center subchannel as depicted in Fig. 5.3 (b) was studied. The rod to wall distance W was varied from 0.6, 0.8, 1.1 to 1.3 times of the gap distance S . The hydraulic diameter of the center subchannel was 11.8 mm, while the hydraulic diameter of the wall subchannel varied from 6.95, 8.09, 9.79 to 10.9 mm. The corresponding relative hydraulic diameter difference was 51.0, 36.7, 18.4 and 7.5%, respectively. Similar to the study of mass flux effect, the axial length of the calculation domain was set at ten times of the hydraulic diameter of the center subchannel. Cyclic boundary condition was employed, in order to achieve the fully developed, equilibrium state. In Fig. 5.8, the boundary conditions are shown for the case of W equals 0.6 times of the gap distance S ¹.

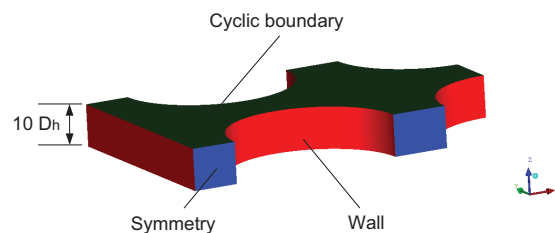


Fig. 5.8: Boundary conditions for determination of the geometrical effect on void fraction distribution at equilibrium state.

¹The same setting of boundary conditions were adopted for other wall distances.

Mathematically the geometrical effect was expressed with the following simple relation:

$$\frac{(\alpha_1 - \alpha_2)_{EQ}}{\alpha_{avg}} = K_2 \cdot \frac{(D_{h,1} - D_{h,2})_{EQ}}{D_{h,avg}} + K_3 \quad (5.21)$$

In the above equation, the hydraulic diameter difference was chosen as the main characteristic parameter to express the geometrical difference between the two subchannels. The same choice can be also found in the literature [see 13, 32, 70]. The physical meaning of the factor K_3 will be explained later in this chapter. Target of this set of simulations was to study the dependence of the factor K_2 and K_3 on the average mass flux G_{avg} and the average void fraction α_{avg} of the two interacting subchannels:

$$K_2 = K_2(\alpha_{avg}, G_{avg}) \quad (5.22)$$

$$K_3 = K_3(\alpha_{avg}, G_{avg}) \quad (5.23)$$

To eliminate the effect of mass flux, friction factor needs to be adjusted. Frictional pressure drop Δp_f , see Eq. 3.19, is expressed as:

$$\Delta p_f = f \cdot \frac{\Delta Z}{D_h} \cdot \frac{G^2}{2\rho}$$

with f the friction factor and ΔZ the axial (streamwise) domain length. In order to equalize the mass flux between the two subchannels, the wall roughness, i.e. the friction factor f , of the larger center subchannel was increased. With increasing wall roughness, mass flux of the center subchannel will decrease, while that in the wall subchannel will increase. The condition of the equalized mass flux was found by an interpolation of several cases. Taken a wall-center subchannel system with rod to wall distance W of $0.8S$ as example, the interpolation process is shown in Fig. 5.9 for the case of average mass flux $3375 \text{ kgm}^{-2}\text{s}^{-1}$ and average void fraction 20%. Through a simple linear interpolation, the void fraction difference at equilibrium

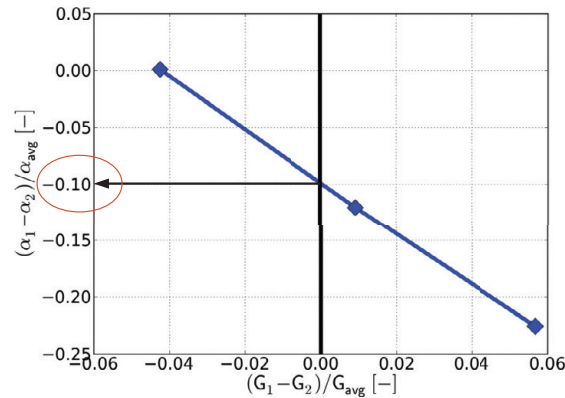


Fig. 5.9: Interpolation to equalize the mass flux in a wall subchannel (denoted with the subscript 1) and a center subchannel (denoted with the subscript 2).

state for the case of equal mass flux in the two subchannels could be obtained. As indicated in Fig. 5.9, the void fraction difference at equilibrium state is about -0.10 .

With the methodology described above, the current set of simulations was performed also for three average mass flux levels of 2250 , 3375 and $4500 \text{ kgm}^{-2}\text{s}^{-1}$ and five average void fractions of 5 , 10 , 15 , 20 and 25% . As depicted in Fig. 5.10, a block-structured mesh was also used. Mesh sensitivity study was carried out with the geometry of $W = 0.8S$, the average mass flux $3375 \text{ kgm}^{-2}\text{s}^{-1}$ and the average void fraction 20% . Three mesh structures of the

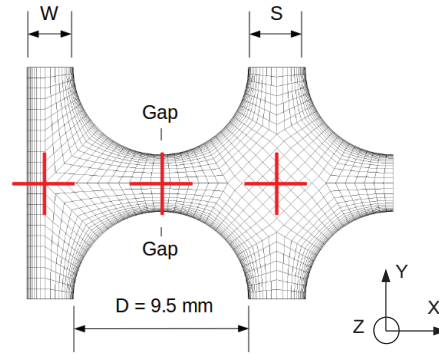


Fig. 5.10: Block topology and mesh structure of the investigated two-channel system consisting of a wall subchannel interacting with a center subchannel; Z direction is the main streamwise direction.

same block topology as shown in Fig. 5.10 but different total cell number of 32181, 77055 and 182000 were tested. In the mesh sensitivity study the wall roughnesses of both wall and center subchannel were not modified. The corresponding y^+ values of the three studied mesh structures were 90, 45 and 20, respectively. Mesh sensitivity study shows that the mesh structure with total node number of 77055 is a good compromise between numerical accuracy and numerical effort. This mesh was hence used for further simulations to study the geometrical effect.

For two average mass flux levels of $2250, 3375 \text{ kgm}^{-2}\text{s}^{-1}$ and two average void fractions of 10, 20%, the void fraction difference at equilibrium state versus the geometrical difference (represented with the hydraulic diameter difference) is shown in Fig. 5.11¹. A good linear

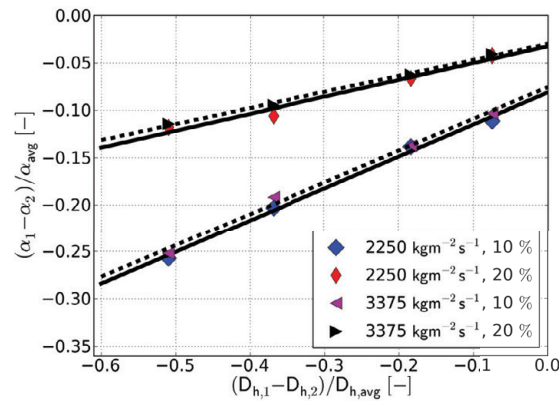


Fig. 5.11: Dependence of the factors K_2 and K_3 on the average mass flux in two interacting subchannels.

relationship between the void fraction difference at equilibrium state and the hydraulic diameter difference can be observed. The slope and the intersection point with the y-axis correspond to the factor K_2 and K_3 in Eq. 5.21, respectively. Two important conclusions can be drawn from Fig. 5.11:

1. The factor K_3 is not equal to zero, for which reason it was included in Eq. 5.21 as proposed previously. The physical meaning of K_3 can now also be easily explained. It stands for void fraction difference at equilibrium state between a wall and a center subchannel, in the case of equalized mass flux and identical hydraulic diameter. This

¹Since the subchannel number 1 refers to the wall subchannel (with smaller hydraulic diameter for the investigated wall to rod distances), the hydraulic diameter difference in Fig. 5.11 has minus values.

void fraction difference is induced by the structure deviation between a wall and a center subchannel, which can not be properly expressed along with the hydraulic diameter difference.

2. For a given set of average void fraction and hydraulic diameter difference, the void fraction difference at equilibrium state is almost independent of the average mass flux. However, the dependence of K_2 and K_3 on the average void fraction is significant.

Based on the above discussion, a series of simulations was performed for a constant average mass flux of $3375 \text{ kgm}^{-2}\text{s}^{-1}$ but varying average void fractions from 5 to 25%. The results are shown in Fig. 5.12. For the considered range of average void fraction, a good

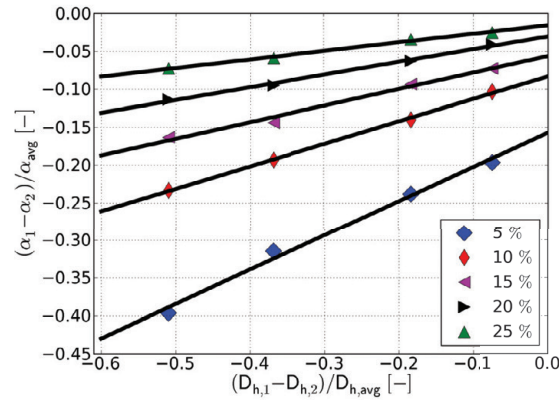


Fig. 5.12: Geometrical effect on void fraction distribution at equilibrium state for a wall-center subchannel combination with various hydraulic diameter differences.

linear relationship between the void fraction difference at equilibrium state and the hydraulic diameter difference can be observed. As discussed above, both factors K_2 and K_3 can be obtained from the slop and the intersection point with the y-axis, respectively. As depicted in

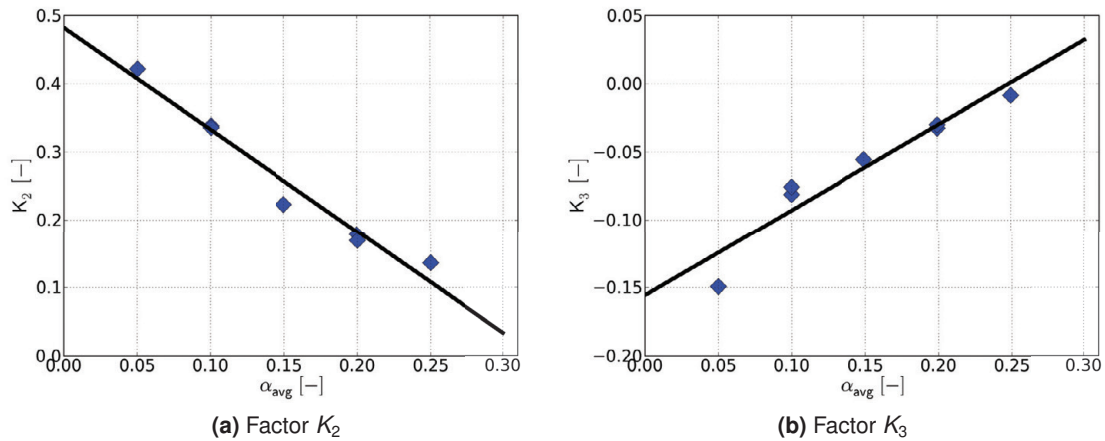


Fig. 5.13: Factor K_2 and K_3 correlated with the average void fraction of two interacting subchannels.

Fig. 5.13, with all the available simulation results, a good linear relationship with the average void fraction can be established for both K_2 and K_3 . This yields:

$$K_2 = -1.496 \cdot \alpha_{avg} + 0.482 \quad (5.24)$$

$$K_3 = 0.627 \cdot \alpha_{avg} - 0.156 \quad (5.25)$$

Summary of the void fraction distribution at equilibrium state

At this point, the effect of mass flux distribution and the effect of geometrical difference on the void fraction difference at equilibrium state has been separately determined. Generally, both effects coexist and need to be combined. In Fig. 5.14 the void fraction difference at equilibrium state is plotted against the mass flux difference for the wall-center subchannel combination and center-center subchannel combination, respectively. The average mass flux of $3375 \text{ kgm}^{-2}\text{s}^{-1}$ and the average void fraction of 20% were taken for both subchannel combinations. As shown in Fig. 5.14, linear relationships between the void fraction difference

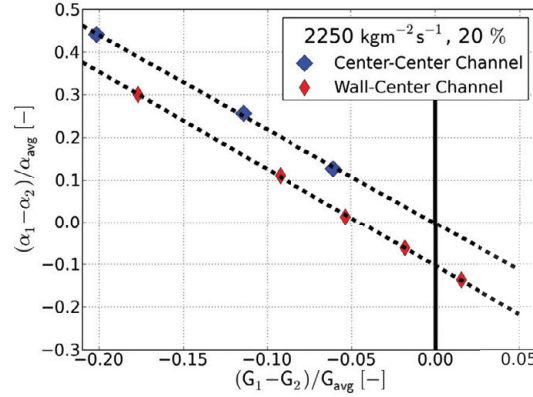


Fig. 5.14: Superposition of the mass flux effect and the geometrical effect on void fraction distribution at equilibrium state.

at equilibrium state and the mass flux difference can be observed for both center-center and wall-center subchannel combinations. Furthermore, these two linear relationships are well parallel to each other. For a certain mass flux difference, the distance between these two linear relationships represents the effect of the geometrical difference. Since this distance was constant for all the cases investigated in the current study, it is concluded that a superposition of the mass flux effect with the geometrical effect is reasonable.

In summary, for a wall subchannel interacting with a center subchannel of different geometry and mass flux, the void fraction difference at equilibrium state can be expressed with the following equation:

$$\frac{(\alpha_1 - \alpha_2)_{EQ}}{\alpha_{avg}} = K_1 \cdot \frac{(G_1 - G_2)_{EQ}}{G_{avg}} + K_2 \cdot \frac{(D_{h,1} - D_{h,2})_{EQ}}{D_{h,avg}} + K_3 \quad (5.26)$$

The factor K_1 , K_2 and K_3 are correlated with the average void fraction of the two interacting subchannels with Eq. 5.20, Eq. 5.24 and Eq. 5.25, respectively. For two center subchannel of the same geometry interacting with each other, the void fraction difference at equilibrium state is given with Eq. 5.18.

5.3.2 Void drift coefficient

As discussed in chapter 5.2, the characteristic void drift velocity is correlated with the average axial (streamwise) velocity with a dimensionless factor β_{VD} , the so-called void drift coefficient. Furthermore, it should be once more mentioned that a direct calculation of the characteristic void drift velocity from the CFD simulation results is not possible. The three elemental interchannel mixing effects, namely turbulent mixing, diversion cross flow and void drift, coexist under two-phase flow conditions. From CFD simulations, only the combined net interchannel mixing can be obtained. With the EMVD model proposed in chapter 5.1, the void drift

mass flow rate per axial length $w_{1to2,g}^{VD}$ can be determined from the CFD simulation results with Eq. 5.14. Together with the constitutive equation for void drift, i.e. Eq. 5.17, β_{VD} can be then obtained with:

$$\beta_{VD} = \frac{w_{1to2,g}^{VD}}{U_{avg} \cdot \rho_g \cdot S \cdot [(\alpha_1 - \alpha_2) - (\alpha_1 - \alpha_2)_{EQ}]} \quad (5.27)$$

It is clearly to see, that the models developed in chapter 5.3.1 for the void fraction distribution at equilibrium state should be applied, in order to obtain β_{VD} from CFD simulation results. The two types of subchannel combination depicted in Fig. 5.3, namely the center-center subchannel and the wall-center subchannel combinations, were considered in the current study.

Center-center subchannel combination

The employed boundary conditions are shown in Fig. 5.15. The calculation domain length was set 100 times of the hydraulic diameter of the center subchannel, in order to enable the two-phase flow to develop. On the solid rod surfaces, no slip condition was applied to both continuous liquid phase and dispersed gaseous phase. A symmetric boundary condition was specified for the six gaps located at the boundary of the computational domain. With this simplification of boundary conditions, the two interacting subchannels can communicate only through the connecting gap, on which the interchannel mixing can be determined. At the

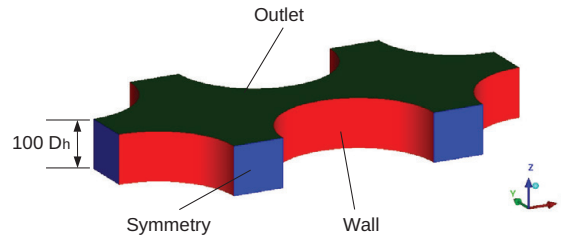


Fig. 5.15: Boundary conditions for determination of void drift coefficient in the center-center subchannel combination.

inlet of the two center subchannels, different steam concentrations were specified hence a non-equilibrium inlet condition was realized. Two-phase flow mixing occurs then through the connecting gap downstream towards the domain outlet, for which a constant static pressure condition was applied.

For investigating the influence of the average mass flux on the void drift coefficient β_{VD} , the inlet streamwise (Z direction in Fig. 5.15) velocity, which was the same for both phases in the two subchannels, was varied systematically from 2, 3, 4, 5 to 6 ms^{-1} . The corresponding average mass flux of the two subchannels varied from 1140 to 3800 $kgm^{-2}s^{-1}$. In order to study the influence of average void fraction on the void drift coefficient β_{VD} , the average void fraction of the two subchannels was varied systematically from 5% to 25%. Constant but different inlet void fractions were given to the two subchannels in such way, that the ratio of the gaseous phase superficial velocity of the high void channel (HVC) to that of the low void channel (LVC) was kept constant, which is defined as the gaseous phase feeding factor F_g :

$$F_g = \frac{j_{g,HVC}}{j_{g,LVC}} \quad (5.28)$$

In current study, three feeding factors F_g of 2, 3 and 4 were selected. In Tab. 5.2, the inlet void

fractions of the two subchannels under different feeding factors are summarized¹. α_{LVC} and α_{HVC} denote the inlet void fraction of the low void channel and that of the high void channel, respectively. α_{avg} stands for the average void fraction of the two interacting subchannels. Due to poor convergence, the simulation results with average void fractions of 5%, 10% and feeding factors F_g of 4 were not taken into account. In all, results of 65 simulations were obtained to determine β_{VD} .

Tab. 5.2: Summary of inlet void fractions with center-center subchannel combination (see Fig. 5.15)

	α_{LVC} [%]	α_{HVC} [%]	α_{avg} [%]
$F_g = 2$	3.3	6.7	5
	6.7	13.3	10
	10.0	20.0	15
	13.4	26.6	20
	16.7	33.4	25
$F_g = 3$	2.5	7.5	5
	5.0	15.0	10
	7.5	22.5	15
	10.0	30.0	20
	12.5	37.5	25
$F_g = 4$	6.0	24.0	15
	8.0	32.0	20
	10.0	40.0	25

The same mesh topology (block-structured grid) as used in chapter 5.3.1 was employed. Two-phase CFD models described in chapter 4.2.1 were further adopted. Mesh sensitivity study was carried out with the case of inlet velocity of 3 ms^{-1} , average inlet void fraction of 15% and feeding factor of 3. Four mesh structures with total cell number of 192300, 230670, 391200, and 654750 were investigated. The corresponding average y^+ values of the first near wall node were 80, 60, 40 and 30, respectively. In Fig. 5.16 the interchannel void drift mass flow rate per length w_{VD} is plotted against the average mesh cell size, which was obtained by dividing the total domain volume by the cell number. The difference between the results

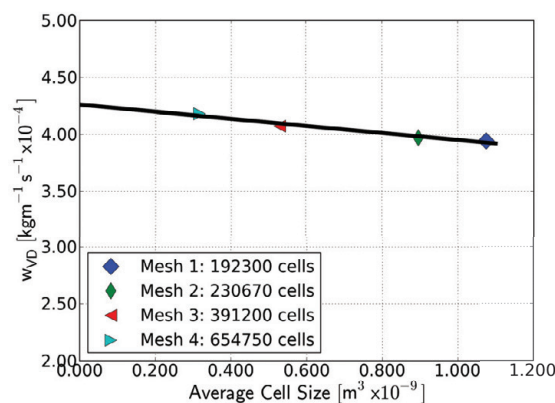


Fig. 5.16: Results of the mesh sensitivity study for determination of void drift coefficient in the center-center subchannel combination.

obtained with the four different mesh structures is small. With a simple graphic extrapolation, the interchannel void drift mass flow rate per length w_{VD} for an infinitely refined mesh structure

¹Noted that simulations with the summarized inlet void fractions were conducted for the five different inlet velocities from 2 to 6 ms^{-1} .

with the average cell size approaching zero can be approximated as $4.26 \times 10^{-4} \text{ kgm}^{-1} \text{ s}^{-1}$. Based a compromise between solution accuracy and limitation on computational resource, the second mesh structure with total cell number of 230670 was chosen for further simulations. Compared to the case with infinitely refined mesh structure, with the chosen mesh structure the relative error is about 6.8%.

The void drift coefficient was determined from the CFD simulations results with Eq. 5.27. On the right hand side of this equation, all the terms, except the void fraction difference at equilibrium state $(\alpha_1 - \alpha_2)_{EQ}$, are available from the CFD results. $(\alpha_1 - \alpha_2)_{EQ}$ can be determined with the correlation developed in chapter 5.3.1. For the center-center subchannel combination, Eq. 5.18 and Eq. 5.20 are sufficient. In Fig. 5.17 the void drift coefficient β_{VD} is plotted against the average void fraction of the two center subchannels for the feeding factors 2 and 3¹. A similar dependence of the void drift coefficient β_{VD} on the average void fraction

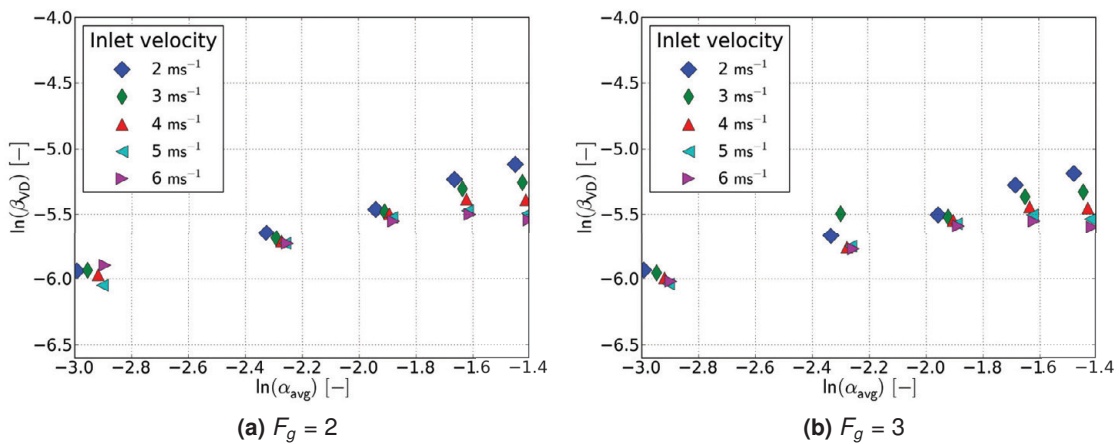


Fig. 5.17: Summary of the void drift coefficient β_{VD} with feeding factors of 2 and 3.

and velocity is observed for the two studied feeding factors. β_{VD} increases with the average void fraction and a linear relationship exists between the logarithm of β_{VD} and the logarithm of α_{avg} for all the studied velocity levels. Furthermore, a slight decrease in β_{VD} with increasing velocities can be found, especially in the high void fraction range. However, this dependence of β_{VD} on velocity is not as large as that on α_{avg} . Despite of different feeding factors, for a given combination of α_{avg} and inlet velocity, the difference between the calculated β_{VD} is negligible, i.e., the dependence of β_{VD} on the feeding factor F_g can be neglected.

The basic approach to develop a correlation for β_{VD} consists of three steps:

1. Definition of characteristic dependent variables of β_{VD} .
2. Proposal of a basic formula describing the relation between β_{VD} and only one of the characteristic variables as the major variable that has apparently the greatest influence.
3. Correlating the parameters in the basic formula proposed in step 2 with the remaining characteristic variables.

Based on the observations from Fig. 5.17, the average void fraction and velocity were defined as the characteristic variables affecting β_{VD} . The effect of velocity was expressed with a

¹Due to limited number of data points (only available for the average void fraction f 15, 20 and 25%), simulation results with the feeding factor F_g of 4 were not considered in developing a correlation for β_{VD} . But they will be used later for assessment of the accuracy of the proposed correlation.

dimensionless liquid phase Reynolds number Re_l defined as:

$$Re_l = \frac{w_{l,avg} \cdot D_{h,avg} \cdot \rho_l}{\mu_l} \quad (5.29)$$

with $w_{l,avg}$ as the average liquid phase velocity and $D_{h,avg}$ the average hydraulic diameter of the two subchannels. ρ_l and μ_l stand for the density and the dynamic viscosity of the single liquid phase, respectively. The average void fraction was chosen as the major parameter owing to its larger influence on β_{VD} than velocity. Due to the observed linear relationship between $\ln\beta_{VD}$ and $\ln\alpha_{avg}$, the following basic formula was proposed:

$$\ln\beta_{VD} = C_1 \cdot \ln\alpha_{avg} + C_2 \quad (5.30)$$

Both coefficients C_1 and C_2 were then correlated with the average liquid Reynolds number $Re_{l,avg}$. As illustrated in Fig. 5.18, both C_1 and C_2 can be well correlated with $Re_{l,avg}$ in form

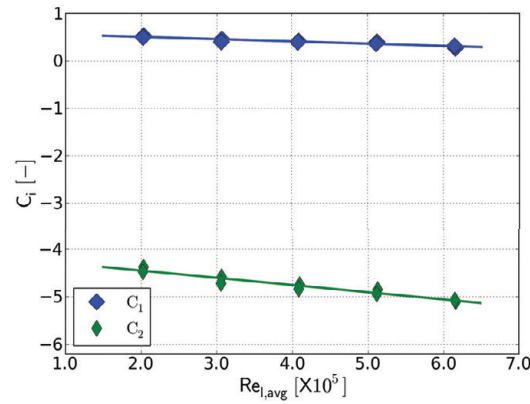


Fig. 5.18: Dependence of the factors C_1 and C_2 on the average liquid Reynolds number $Re_{l,avg}$ of two interacting center subchannels.

of a linear function, which are expressed with the following equations:

$$C_1 = -0.477 \cdot 10^{-6} \cdot Re_{l,avg} + 0.600 \quad (5.31)$$

$$C_2 = -1.520 \cdot 10^{-6} \cdot Re_{l,avg} - 4.149 \quad (5.32)$$

Assessment of the developed correlations was performed by comparing the void drift coefficient obtained from CFD simulation (β_{VD}^{CFD}) with the void drift coefficient calculated with the correlations (β_{VD}^{Corr}). The average relative deviation E_{rel} , defined for n simulations cases as:

$$E_{rel} = \frac{1}{n} \cdot \sum_{i=1}^n \frac{|\beta_{VD}^{CFD} - \beta_{VD}^{Corr}|}{\beta_{VD}^{CFD}} \quad (5.33)$$

was used to quantify the accuracy of the developed correlations. In Fig. 5.19 the comparison between β_{VD}^{CFD} and β_{VD}^{Corr} is shown for the feeding factors F_g 2 and 3. The two dashed lines in both figures denote +10% and -10% relative deviation, respectively. With the proposed correlations as expressed with Eq. 5.30, 5.31 and 5.32, the void drift coefficient β_{VD}^{CFD} can be well recalculated. The average relative deviation E_{rel} is less than 5.0% for both feeding factors F_g of 2 and 3. β_{VD}^{CFD} obtained with feeding factor F_g of 4, which was not considered in developing the correlation due to the limited number of data points, was used to assess the proposed correlations. Results are shown in Fig. 5.20. A slight overprediction of β_{VD}^{CFD} can be observed, however an overall good agreement is still obtained. The average relative deviation E_{rel} has a value of 7.3%.

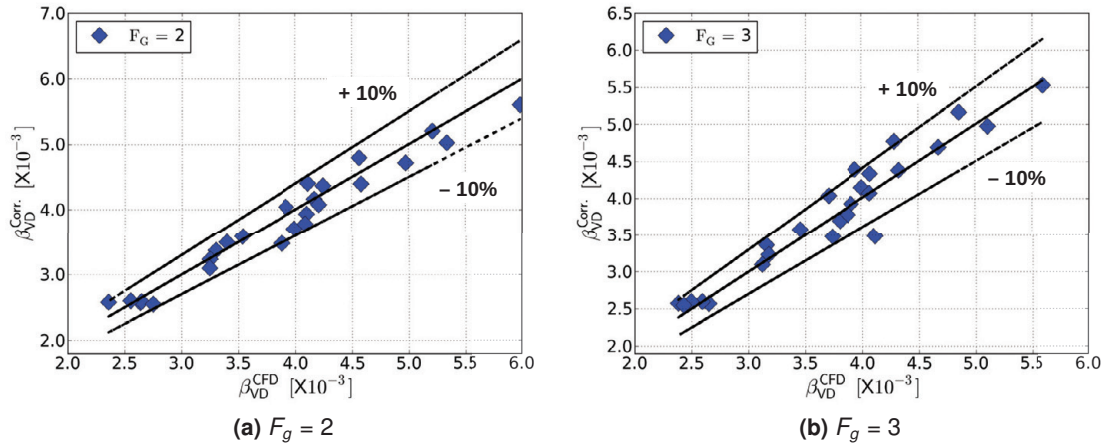


Fig. 5.19: Assessment of the proposed correlation of void drift coefficient in the center-center subchannel combination (feeding factor F_g equals 2 and 3).

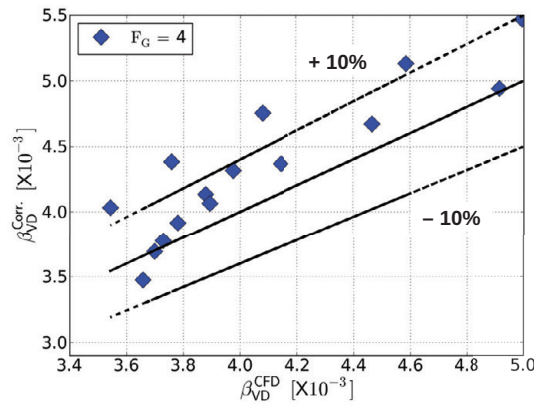


Fig. 5.20: Assessment of the proposed correlation of void drift coefficient in the center-center subchannel combination (feeding factor F_g equals 4).

Wall-center subchannel combination

Four wall-center subchannel geometries with different wall distance W (see Fig. 5.3 (b)) were investigated. The wall distance W to the gap clearance S ratio W/S was varying from 0.6, 0.8, 1.1 towards 1.3. At the inlet boundary, the same phase velocity and void fraction were set for both wall and center subchannel. Due to the geometrical difference between the wall and the center subchannel, different velocity fields were established, which led to net interchannel mixing between the two subchannels. Similar to the study of void drift coefficient in the center-center subchannel combination, the calculation domain length was set 100 times of the hydraulic diameter of the center subchannel. The employed boundary conditions are shown in Fig. 5.21 for the case of W equals $0.8 S$ ¹.

The same mesh topology used in chapter 5.3.1 was employed. A mesh sensitivity study was carried out for the case with W/S of $0.8 S$, inlet velocity of 3 m/s and average void fraction of 15%. Six mesh structures with total cell number from 170190 to 580650 were tested. The corresponding y^+ values were varying from 90 to 25. The mesh structure with cell number of 257620 and y^+ of 60 provided a good balance between numerical accuracy and numerical effort and was hence chosen for further simulations.

¹The same setting of boundary conditions were adopted for other wall distances.

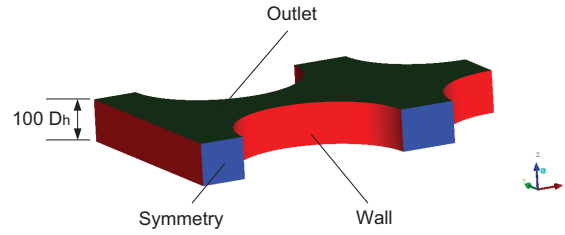


Fig. 5.21: Boundary conditions for determination of void drift coefficient in the wall-center subchannel combination.

The inlet velocity was varied from 2, 3, 4, 5 to 6 m/s with the average void fraction from 5, 10, 15, 20 to 25%. With the four different W/S values, in total 100 simulations were performed. In order to calculate the void drift coefficient β_{VD} , Eq. 5.27 was also used. The required void fraction difference at equilibrium state $(\alpha_1 - \alpha_2)_{EQ}$ between a wall subchannel and a center subchannel was obtained with Eq. 5.26. The coefficients K_1 , K_2 and K_3 were calculated with Eq. 5.20, 5.24 and 5.25, respectively. In Fig. 5.22 the calculated β_{VD} is plotted against the average void fraction α_{avg} for all the four studied W/S values. Except for W/S of 1.3, all the

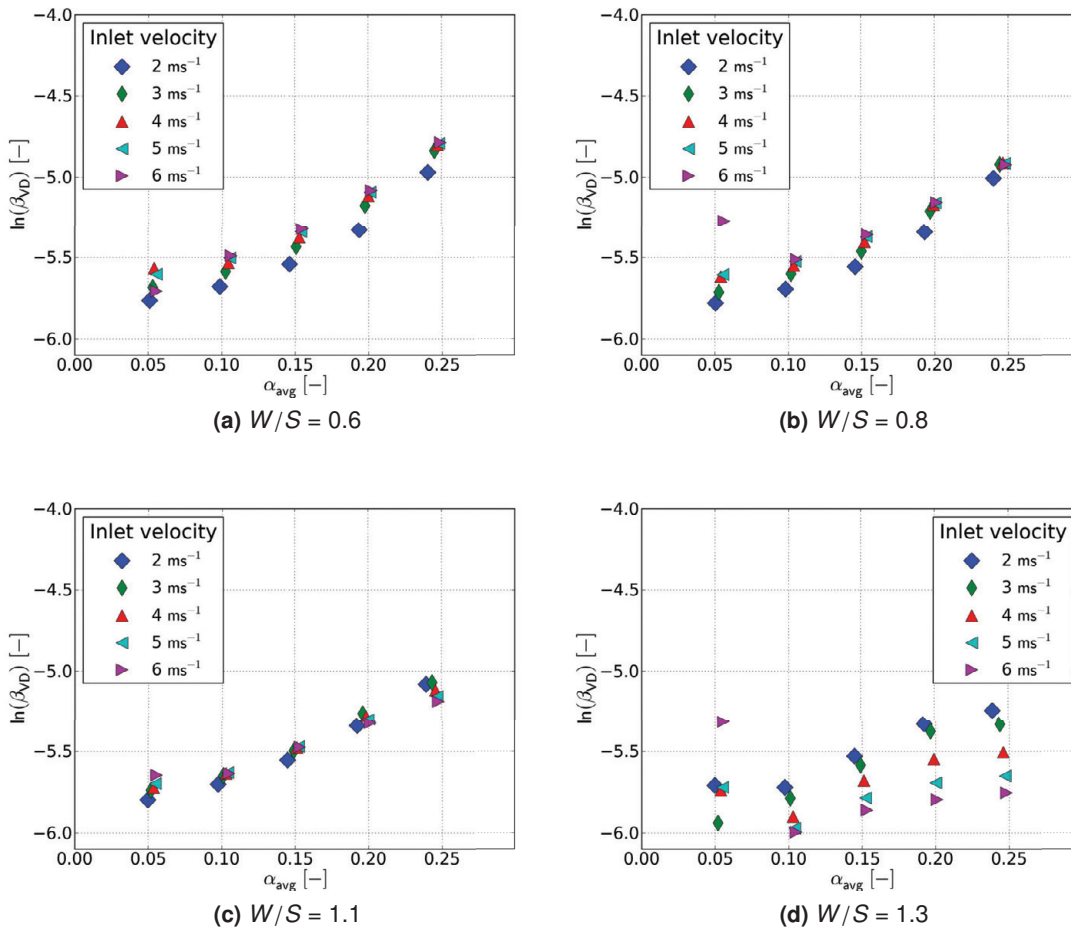


Fig. 5.22: Dependence of the void drift coefficient β_{VD} on the average void fraction with varying W/S from 0.6, 0.8, 1.1 to 1.3.

data points show similar trend, which can be summarized as follows:

1. The average void fraction exerts a dominant influence on the void drift coefficient also

in the case of wall-center subchannel combination. β_{VD} increases with the average void fraction.

2. The velocity plays only a subordinated role. Despite an increasing in velocity from 2 to 6 ms^{-1} , no large difference of β_{VD} can be observed.
3. With W/S increasing from 0.6 to 1.1, the void drift coefficient β_{VD} decreases slightly. This indicates an influence of the geometrical difference, which may be neglected in developing a correlation for β_{VD} .

In typical PWR fuel assemblies or in rod bundle benchmarks available in the open literature, the value of W/S is normally in the order of 0.8 and always smaller than unity. Therefore, the data points obtained with W/S of 1.3 were not considered in developing a correlation for β_{VD} . The same three-step approach as used in the case of center-center subchannel combination was further adopted. As characteristic dependent variables, except the average void fraction α_{avg} and the average liquid Reynolds number $Re_{l,avg}$, a geometrical parameter must be selected to describe the influence of the geometrical difference between a wall and a center subchannel. In the current study, the relative hydraulic diameter difference $\Delta D_{h,rel}$ was chosen:

$$\Delta D_{h,rel} = \frac{|D_{h,wall} - D_{h,center}|}{D_{h,avg}} \quad (5.34)$$

As seen in Fig. 5.22, the average void fraction was set as the dominant parameter. The basic formula for β_{VD} of the wall-center subchannel combination was proposed as:

$$\ln \beta_{VD} = C_3 \cdot \alpha_{avg} + C_4 \quad (5.35)$$

The dependence of both coefficients C_3 and C_4 on the other two characteristic dependent variables, i.e. $Re_{l,avg}$ and $\Delta D_{h,rel}$, is illustrated in Fig. 5.23. It reveals that C_4 is hardly

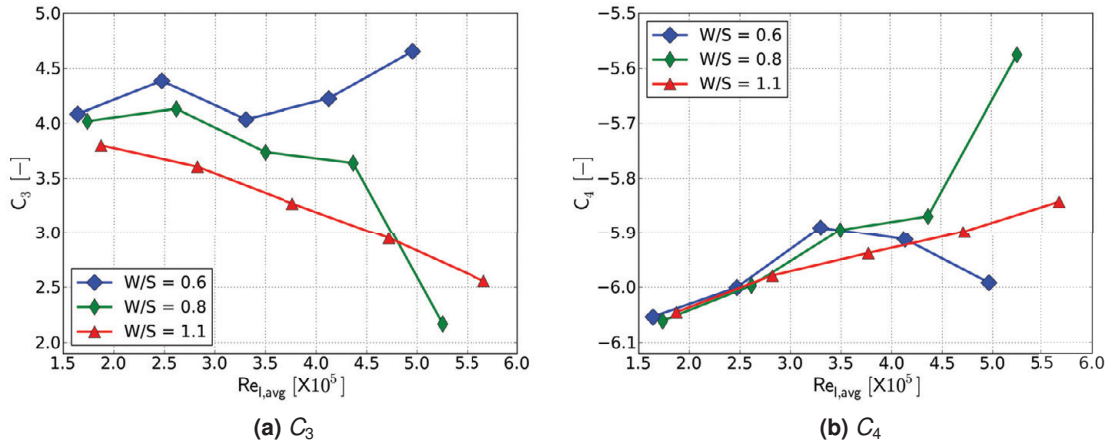


Fig. 5.23: Dependence of the factors C_3 and C_4 on $Re_{l,avg}$ with varying W/S from 0.6, 0.8 to 1.1 (the corresponding $\Delta D_{h,rel}$ varying from 51.0, 36.7 to 18.4%).

dependent on W/S (i.e. $\Delta D_{h,rel}$) at $Re_{l,avg}$ smaller than 400000. Deviation of C_4 at different W/S values becomes larger at higher $Re_{l,avg}$, is however less than 10%. In the current study, C_4 was thus taken as a constant value, which is equal to the average value of all the data points in Fig. 5.23 (b).

$$C_4 = -5.916 \quad (5.36)$$

Some difficulties arise for correlating the coefficient C_3 . As depicted in Fig. 5.23 (a), C_3 depends not only on the liquid Reynolds number $Re_{l,avg}$ but also on the W/S . For W/S of

0.6 C_3 increases slightly with rising $Re_{l,avg}$, while it decreases with rising $Re_{l,avg}$ for W/S of 0.8 and 1.1. Furthermore, for the entire liquid Reynolds number range, C_3 tends to decrease with increasing W/S values. In order to model C_3 with an acceptable effort, the dependence of C_3 on $Re_{l,avg}$ was neglected in the current study. C_3 obtained with each W/S values were averaged and then correlated with the hydraulic diameter difference $\Delta D_{h,rel}$ as defined in Eq. 5.34. The result is plotted in Fig. 5.24. C_3 can be correlated with $\Delta D_{h,rel}$ with a linear

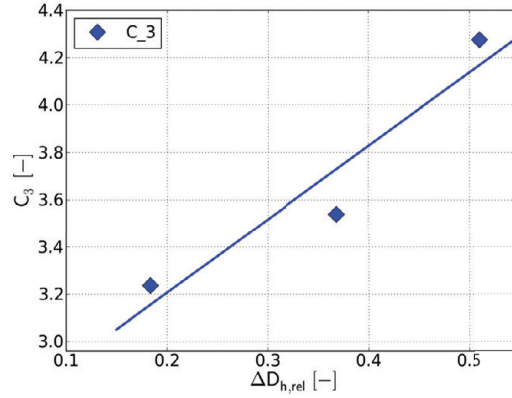


Fig. 5.24: Dependence of the factors C_3 on the absolute relative hydraulic diameter difference $\Delta D_{h,rel}$ defined in Eq. 5.34.

relationship as:

$$C_3 = 3.106 \cdot \Delta D_{h,rel} + 2.584 \quad (5.37)$$

The assessment of the above proposed correlations for β_{VD} in the wall-center subchannel combination, expressed with Eq. 5.35, 5.37 and 5.36, was performed by recalculating the void drift coefficients obtained from CFD simulation β_{VD}^{CFD} and the corresponding ones calculated with proposed correlations β_{VD}^{Corr} . In Fig. 5.25 β_{VD}^{Corr} is compared with β_{VD}^{CFD} for all the four W/S from 0.6 to 1.3. The two dashed lines in each subfigures denote the +10% and -10% relative deviation, respectively. For W/S of 0.6, 0.8 and 1.1, β_{VD}^{CFD} can be well recalculated with the proposed correlation, despite the negligence of the dependence of C_3 on the liquid Reynolds number. The average deviations E_{rel} between β_{VD}^{CFD} and β_{VD}^{Corr} are 7.4%, 6.6% and 4.1%, respectively. However, for W/S of 1.3, the proposed correlation fails to recalculate β_{VD}^{CFD} with acceptable accuracy. For most of the cases, the proposed correlations overpredict β_{VD}^{CFD} . The average relative deviation E_{rel} is over 30%.

Summary of the developed correlations for void drift coefficient

The proposed correlations for void drift coefficient β_{VD} based on the CFD simulations conducted in the current study are summarized in Tab. 5.3.

Tab. 5.3: Proposed correlations of void drift coefficient β_{VD} based on CFD simulations conducted in the current study

Center-center subchannel combination	Wall-center subchannel combination
$\ln \beta_{VD} = C_1 \cdot \ln \alpha_{avg} + C_2$	$\ln \beta_{VD} = C_3 \cdot \alpha_{avg} + C_4$
$C_1 = -0.477 \cdot 10^{-6} \cdot Re_{l,avg} + 0.600$	$C_3 = 3.106 \cdot \Delta D_{h,rel} + 2.584$
$C_2 = -1.520 \cdot 10^{-6} \cdot Re_{l,avg} - 4.149$	$C_4 = -5.916$

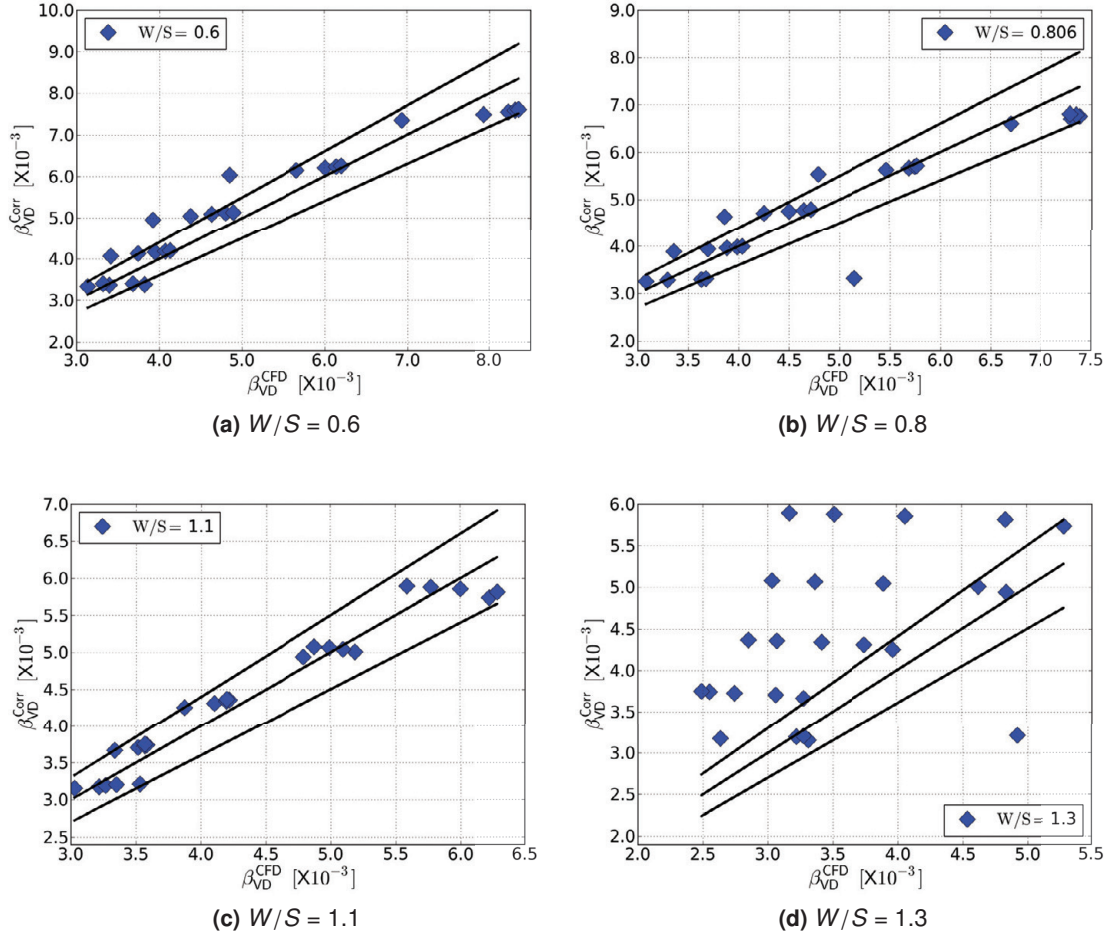


Fig. 5.25: Assessment of the proposed void drift coefficient correlation in the wall-center subchannel combination with varying W/S from 0.6, 0.8, 1.1 to 1.3.

These correlations will be implemented into the subchannel code MATRA for validation calculation in the next chapter. It should be emphasized again that the correlations for the wall-center subchannel combination are only applicable for W/S not larger than 1.1.

5.4 Discussion about void drift and lift force

As found in the validation calculations in chapter 4.2, lift force has a considerable influence on the predicted interchannel mixing effect. Therefore, it is necessary to investigate the lift force more closely. As discussed in chapter 2.1.2, the lift force acting on dispersed bubbles in a subchannel flow with Z as the main streamwise direction is given in a simplified way with Eq. 2.3:

$$\mathbf{F}_L = C_L \cdot \rho_l \cdot \alpha \cdot \begin{pmatrix} -w_r \frac{\partial w_l}{\partial X} \\ -w_r \frac{\partial w_l}{\partial Y} \\ 0 \end{pmatrix}$$

With a positive lift force coefficient C_L as used in the current study (C_L equal to 0.05), lift force acting on bubbles is opposite to liquid phase velocity gradient. Therefore, lift force will push bubbles laterally towards regions with relative lower liquid phase velocities, i.e., towards solid rod surfaces and also towards gap regions. A higher void fraction near the solid wall and also in

the gap region than in the subchannel bulk will be expected. For two subchannels interacting via a connecting gap, the bubbles coming from the individual subchannel bulk regions will meet somewhere in the gap region. This can lead further to an interchannel mixing of the gaseous phase, if the lift force acting on bubbles is not the same between the two interacting subchannels.

According to the proposed EMVD interchannel mixing model in chapter 5.1, diversion cross flow and void drift are the two interchannel mixing effects, which may induce net mass exchange between interacting subchannels. Considering the case of two interacting subchannels without any lateral pressure difference but with a difference in velocity field, void drift is then the only driving factor for interchannel mixing inducing net mass exchange. In this case, the difference in velocity field leads to a discrepancy of the lift force acting on bubbles in the two subchannels, which may result in net interchannel mass exchange. Based on the above brief discussion, it is plausible to assume that void drift is closely related to the lift force acting on bubbles. The direction of a net gaseous phase flow due to void drift can be deduced from comparing the lift force acting on bubbles in the two interacting subchannels. A net lateral gaseous phase flow due to void drift is expected from the subchannel with a larger lift force to the subchannel with a smaller lift force acting on bubbles.

To verify the proposed assumption, simulation results conducted with the center-center subchannel combination in chapter 5.3.2 were reviewed in the current study. The chosen simulation case has inlet velocity 5 m s^{-1} , average void fraction 20% and gaseous phase feeding factor 2. On the cross-sectional plane with Z equal to 0.9 m (about 30 times of hydraulic diameter upstream of the outlet boundary), flow parameters in the two interacting subchannels were investigated. Fig. 5.26 shows the distribution of void fraction and liquid phase velocity. Due to the different gaseous phase feeding at the inlet boundary, i.e. higher gaseous phase feeding in the right subchannel, both void fraction and liquid phase velocity are higher in the right subchannel.

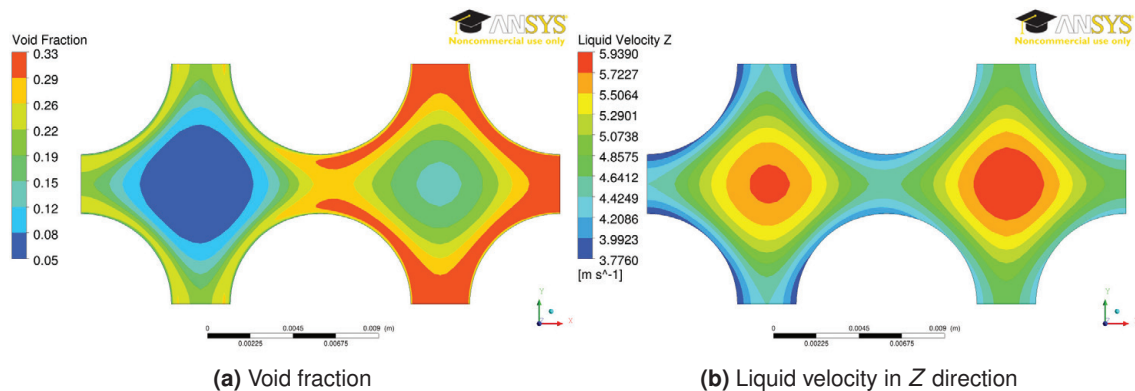


Fig. 5.26: Void fraction and liquid velocity on a cross-sectional plane at Z elevation of 0.9 m .

Due to the existing lateral pressure difference between the two interacting subchannels, diversion cross flow coexists with void drift. According to the EMVD two-phase interchannel mixing model proposed in chapter 5.1, diversion cross flow induces net interchannel mass flows for both liquid and gaseous phase. Turbulent mixing does not cause net interchannel mass exchange and void drift considers only the interchannel exchange of the gaseous phase. This implies that the net liquid phase interchannel mixing can be solely attributed to diversion cross flow. The direction of diversion cross flow can hence be revealed by examining the direction of the net liquid phase interchannel mass exchange. In Fig. 5.27 (a), the liquid phase velocity in X direction, corresponding to the direction normal to the connecting gap, is illustrated for both subchannels. A liquid phase velocity in the positive X direction is

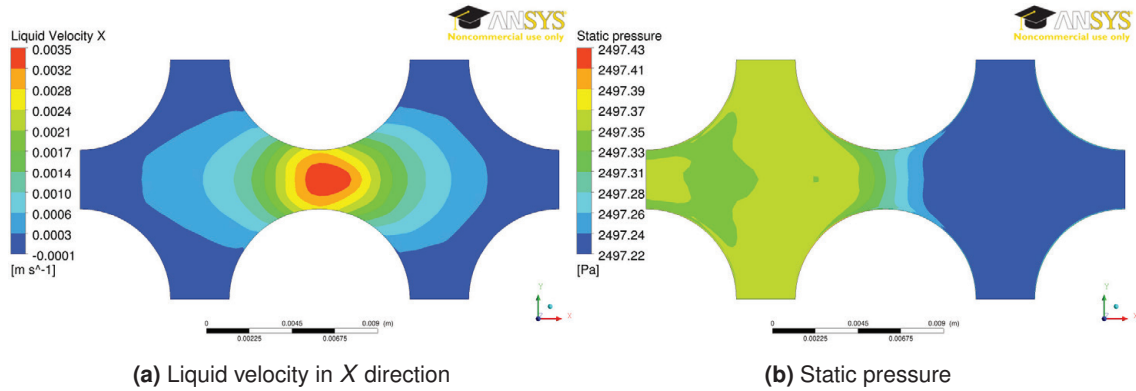


Fig. 5.27: Diversion cross flow mechanism interpreted with the static pressure difference in two interacting subchannels.

clearly observed, which indicates a net liquid phase flow from the left subchannel to the right subchannel, i.e., diversion cross flow is from the left to the right subchannel. As depicted in Fig. 5.27 (b), static pressure in the left subchannel is higher than that in the right subchannel. The direction of the pressure gradient in the gap region is opposite to the liquid phase velocity in X direction. This observation confirms the classical definition of diversion cross flow induced by the lateral pressure difference between two interacting subchannels¹.

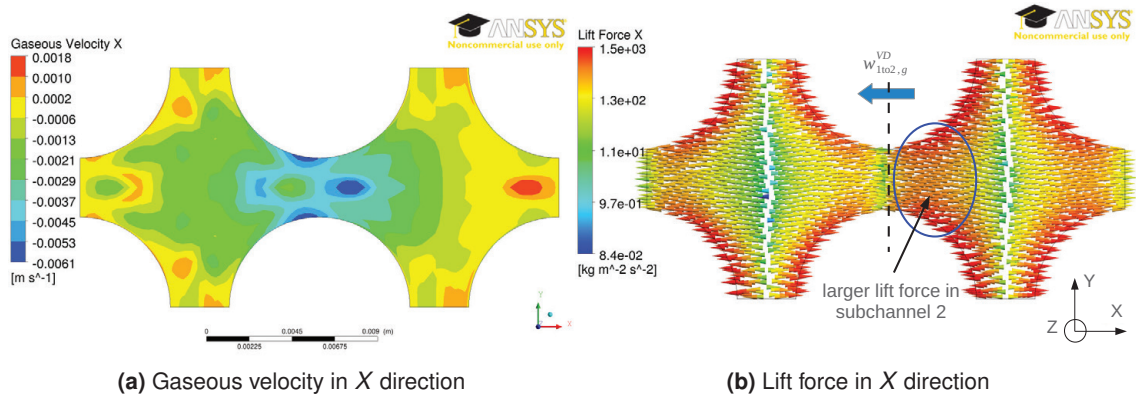


Fig. 5.28: Gaseous phase velocity and lift force acting on dispersed bubbles.

In Fig. 5.28 (a), the gaseous phase velocity in X direction is shown for both subchannels. In the connecting gap region, the gaseous phase velocity is in the negative X direction, which indicates a net gaseous phase mass flow from the right to the left subchannel. As discussed above, diversion cross flow causes a lateral gaseous flow from left subchannel to right subchannel, the net gaseous flow as observed in Fig. 5.28 (a) should be attributed to void drift, which yields a larger net gaseous interchannel mixing than diversion cross flow in the opposite direction. To verify the assumed close relation between lift force to void drift, Fig. 5.28 (b) illustrates the lift force acting on bubbles in X direction. Due to the fact, that the largest liquid velocity locates in the center of each subchannels (see Fig. 5.26 (b)), lift force in each subchannels can be divided into two parts with opposite directions. Regarding interchannel mixing, the lift force near the connecting gap region should be examined closely. It is seen that lift force in the right subchannel is larger than that in the left subchannel. This is also to

¹In fact the small magnitude of the lateral pressure difference is a consequence of diversion cross flow, because the net mass flow rate from subchannel of higher pressure to subchannel of lower pressure leads simultaneously to an equalization of the pressure level in the two interacting subchannels.

be expected. The liquid phase velocity w_l in the right subchannel, as shown in Fig. 5.26 (b), is larger than that in the left subchannel, so that the average value of the velocity gradient ($\partial w_l / \partial X$) is larger in the right subchannel, i.e., lift force in the right subchannel should also be larger than that in the left subchannel. According to the assumed close relation between lift force and void drift, it is concluded that a net lateral gaseous mass flow from the right subchannel to the left subchannel occurs due to void drift. This conclusion is consistent with the observation made in Fig. 5.28 (a). To sum up, the discussion above verifies that void drift has a close relation with lift force. Void drift yields a net gaseous mixing flow from subchannel of larger lift force to subchannel of smaller lift force acting on dispersed bubbles.

To investigate the relation between lift force and void drift more systematically, a set of simulations was performed with the center-center subchannel combination as used in chapter 5.3.2. For convenience, the two interacting center subchannels are depicted again in Fig. 5.29. The same setting of boundary conditions as shown in Fig. 5.15 was adopted. At the

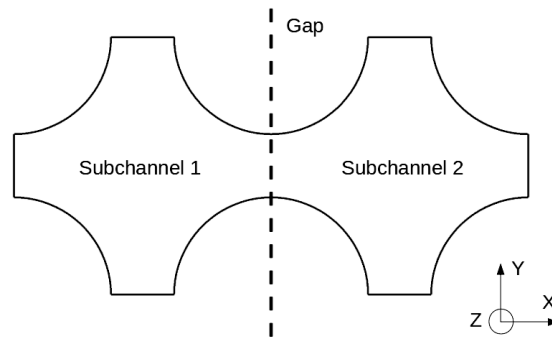


Fig. 5.29: Study of the relation between void drift and lift force with two interacting center subchannels; Z direction is the main streamwise direction.

inlet boundary, a constant void fraction of 20% and a constant phase velocity of 5 ms^{-1} were given to both subchannels. Wall roughness of the subchannel 1 was artificially increased, in order to enforce different velocity fields in the two subchannels. Six simulations were conducted by stepwise increasing the wall roughness of subchannel 1, as summarized in Tab. 5.4.

Tab. 5.4: Summary of boundary conditions for study of the relation between void drift and lift force

	Subchannel 1	Subchannel 2
Inlet velocity	5 ms^{-1}	
Inlet void fraction	20%	
Outlet boundary	constant static pressure	
Wall roughness	RUN 1	$1 \cdot 10^{-6} \text{ m}$
	RUN 2	$2 \cdot 10^{-6} \text{ m}$
	RUN 3	$3 \cdot 10^{-6} \text{ m}$
	RUN 4	$5 \cdot 10^{-6} \text{ m}$
	RUN 5	$8 \cdot 10^{-6} \text{ m}$
	RUN 6	$10 \cdot 10^{-6} \text{ m}$

Due to the enhanced wall roughness, static pressure in subchannel 1 is larger than that in subchannel 2. Diversion cross flow is hence expected in the direction from subchannel 1 to subchannel 2. In Fig. 5.30 the gaseous and liquid part of diversion cross flow, i.e. $w_{1to2,l}^{DC}$ and $w_{1to2,g}^{DC}$, are plotted against the pressure difference between the two subchannels, which is defined as $\Delta p_{12} = p_1 - p_2$ with p_1 and p_2 denoting the average static pressure of subchannel 1 and 2, respectively. From RUN 1 to RUN 6 with rising wall roughness of subchannel 1,

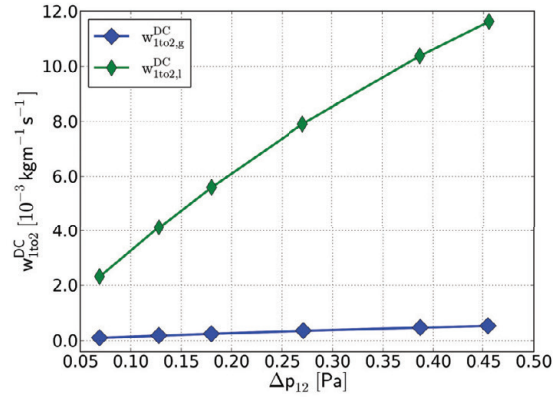


Fig. 5.30: Diversion cross flow due to lateral pressure difference between two interacting subchannels.

pressure difference between the two subchannels also increases. As observed in Fig. 5.30 that both $w_{1to2,l}^{DC}$ and $w_{1to2,g}^{DC}$ increase with the rising pressure difference Δp_{12} from RUN 1 to RUN 6. This confirms the close relation between diversion cross flow and the lateral pressure difference. The positive values of $w_{1to2,l}^{DC}$ and $w_{1to2,g}^{DC}$ indicating a net mass flow rate from subchannel 1 to subchannel 2 confirm also the expectation of diversion cross flow from subchannel 1 of higher pressure level to subchannel 2 with lower pressure level.

To discuss the relation between lift force and void drift, lift force along a line connecting the centroid points of both subchannels at Z of 0.9 m will be discussed, as shown in Fig. 5.31 (a) for RUN 6. In Fig. 5.31 (b) the lift force in X direction on the defined line are plotted for

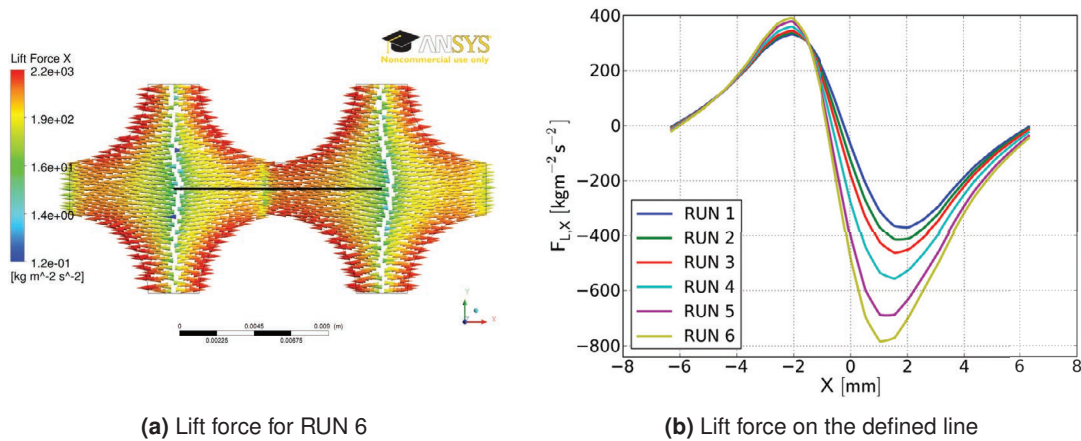


Fig. 5.31: Lift force in the X direction on the defined line for test cases in Tab. 5.4.

all the studied six simulation runs as summarized in Tab. 5.4. As expected, with rising wall roughness of subchannel 1 from RUN 1 to RUN 6, the liquid phase velocity difference between the two subchannels also increases, which leads to an increase in lift force difference in the two subchannels. From RUN 1 to 6, lift force acting in the negative X direction increases more intensively than that acting in the positive X direction. This yields an increase in net void drift mass flow from subchannel 2 to 1. Fig. 5.32 shows the average value of lift force along the defined line against the void drift mass flow from subchannel 1 to 2. The negative values of w_{1to2}^{VD} denote that net void drift flow is from subchannel 2 to subchannel 1. The magnitude of net void drift mass flow increases with the magnitude of lift force, which confirms also the close relation between lift force and void drift.

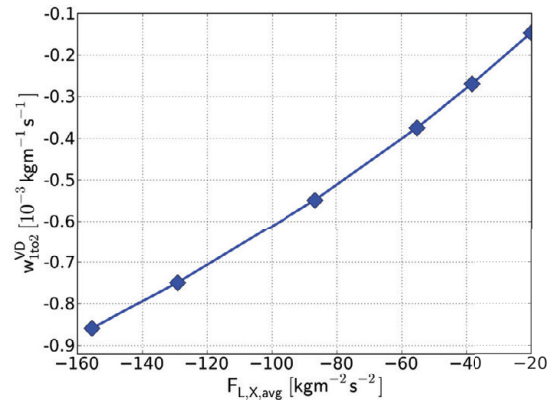


Fig. 5.32: The relation between void drift and lift force acting on dispersed bubbles.

In summary, based on the discussion made in this chapter, a close relation between void drift and lift force acting on the dispersed bubbles can be concluded. However, in the current study, lift force is modeled with a constant lift force coefficient due to the lacking of reliable lift force models. For more insight into void drift, some fundamental investigations of lift force are necessary in the future.

6. Validation and application of the proposed void drift model

In this chapter the proposed two-phase interchannel mixing model will be implemented in MATRA and validated. Subsequently, selected empirical CHF correlations will be assessed based on the improved MATRA code.

6.1 Validation of the proposed void drift model

The interchannel mixing terms of mass, momentum and energy between two interacting subchannels i and j according to the EMVD model proposed in chapter 5.1 are summarized in Tab. 6.1¹.

Tab. 6.1: Summary of the interchannel mixing terms of mass, momentum and energy between two interacting subchannels i and j

	Mass	0
TM	Momentum	$\theta \cdot \beta_{SP} \cdot G_{avg} \cdot S \cdot \left(\frac{m_i}{\hat{\rho}_i A_i} - \frac{m_j}{\hat{\rho}_j A_j} \right)$
	Energy	$\theta \cdot \beta_{SP} \cdot G_{avg} \cdot S \cdot (\hat{h}_i - \hat{h}_j)$
	Mass	$\rho_i \cdot u_{DC} \cdot S$
DC	Momentum	$\rho_i \cdot u_{DC} \cdot S \cdot \frac{m_i}{\hat{\rho}_i A_i}$
	Energy	$\rho_i \cdot u_{DC} \cdot S \cdot \hat{h}_i$
	Mass	$\beta_{VD} \cdot U_{avg} \cdot \rho_g \cdot S \cdot [(\alpha_i - \alpha_j) - (\alpha_i - \alpha_j)_{EQ}]$
VD	Momentum	$\beta_{VD} \cdot U_{avg} \cdot \rho_g \cdot S \cdot [(\alpha_i - \alpha_j) - (\alpha_i - \alpha_j)_{EQ}] \cdot \frac{m_i \cdot x_i}{\rho_g \cdot A_i \cdot \alpha_i}$
	Energy	$\beta_{VD} \cdot U_{avg} \cdot \rho_g \cdot S \cdot [(\alpha_i - \alpha_j) - (\alpha_i - \alpha_j)_{EQ}] \cdot h_g$

Diversion cross flow is solved directly in MATRA with the transverse momentum equation (see Eq. 3.11). Regarding turbulent mixing, the equal-mass-exchange assumption (see chapter 3.2.1) is adopted, so that the net mass exchange due to turbulent mixing is zero. To describe the effective mixing velocity due to turbulent mixing, the single phase turbulent mixing coefficient β_{SP} and the Beus two-phase turbulent mixing multiplier θ [9] are adopted. According to the EMVD model, void drift is described as a diffusion process of the dispersed bubbles, so that the void drift terms given in Tab. 6.1 contain only thermal-hydraulic properties of the gaseous phase. The void drift coefficient β_{VD} and the void fraction difference at equilibrium

¹Regarding diversion cross flow, the subchannels i is assumed to be the donor subchannel. The direction of void drift is also assumed from the subchannel i to j .

state $(\alpha_i - \alpha_j)_{EQ}$ are evaluated with the models proposed in chapter 5.3.2 and chapter 5.3.1, respectively.

Selected test cases of the ISPRA EUROP rod bundle benchmark [31] were used in the current chapter for validation calculation. Since the EMVD model was developed under PWR pressure levels in the bubbly flow regime, only test cases under PWR system pressure level (about 160 *bar*) and in the bubbly flow regime were selected for recalculation with MATRA. 35 test cases with various inlet subcooling and bundle average mass flux were suitable for the validation purpose. The same setting of MATRA models given in Tab. 3.5 was adopted except the two-phase interchannel mixing model. For comparison with measurement results, the subchannel enthalpy increase h_{inr} defined in Eq. 3.65 and the relative subchannel exit mass flux were used, which is defined as:

$$q_{mr} = \frac{G_i^{ex}}{G_b} \quad (6.1)$$

with G_i^{ex} and G_b denoting the exit mass flux of subchannel i and the bundle average mass flux, respectively. In Fig. 6.1, the prediction to measurement ratio (P/M) of h_{inr} and q_{mr} is plotted for the wall subchannel (see Fig. 3.6). For reference, the prediction to measurement ratios (P/M) obtained with the two types of EVVD model available in MATRA (see chapter 3.2.2) are also plotted. Regarding the subchannel exit mass flux, negligible difference between the

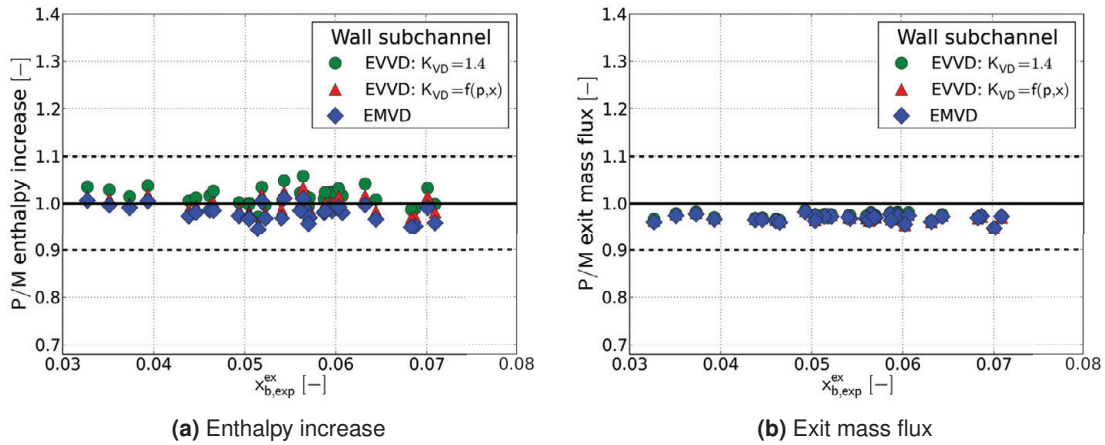


Fig. 6.1: Validation of the EMVD model with prediction to measurement ratio of subchannel enthalpy increase and exit mass flux of the wall subchannel.

prediction of different interchannel mixing models is observed. Related to the subchannel enthalpy increase, the proposed EMVD model shows overall good agreement, however slightly underpredicts the enthalpy increase of the wall subchannel.

Fig. 6.2 shows the prediction to measurement ratio (P/M) of enthalpy rise and exit mass flux for the corner subchannel (see Fig. 3.6). The proposed EMVD model provides a better prediction performance of the corner subchannel exit mass flux than the EVVD model with K_{VD} as a constant value of 1.4. However, with the EMVD model enthalpy rise of the corner subchannel is underpredicted. This is perhaps due to the fact, that the proposed EMVD model was developed in the current study with CFD simulation results obtained with the center-center and wall-center subchannel combinations. No corner subchannel was considered in the CFD simulations. This indicates that the corner-wall subchannel combination should be investigated in the future for studying the interchannel mixing effect.

Fig. 6.3 presents the prediction to measurement ratio (P/M) of enthalpy rise and exit mass flux in the center subchannel (see Fig. 3.6). All the three mixing models provide similar predic-

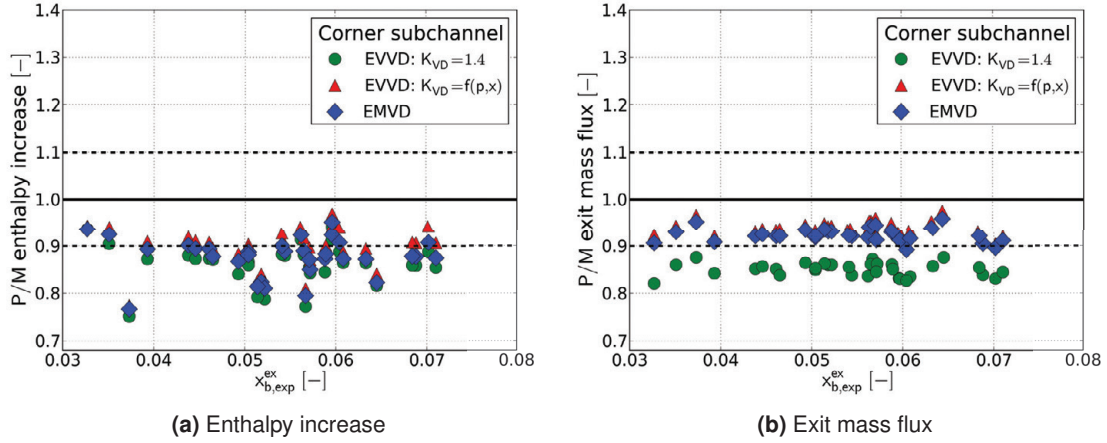


Fig. 6.2: Validation of the EMVD model with prediction to measurement ratio of subchannel enthalpy increase and exit mass flux of the corner subchannel.

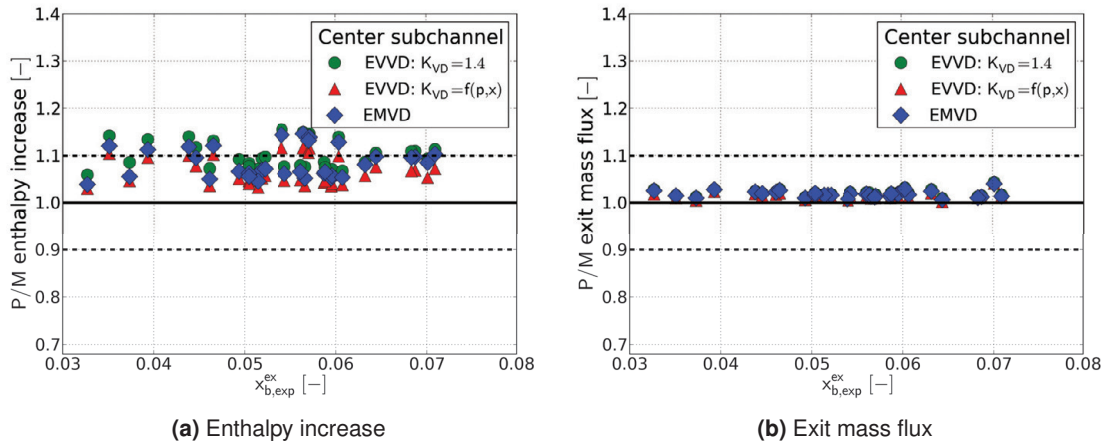


Fig. 6.3: Validation of the EMVD model with prediction to measurement ratio of subchannel enthalpy increase and exit mass flux of the center subchannel.

tion accuracy of the center subchannel exit mass flux. However, the proposed EMVD model overpredicts enthalpy rise of the center subchannel. The simultaneous overprediction of enthalpy increase in the center subchannel and underprediction of that in the corner subchannel indicate that an energy flow from center subchannel through wall subchannel towards corner subchannel is not properly considered by the EMVD model proposed in the current study. This confirms again that investigation of the corner-wall subchannel combination should be performed in the future.

To sum up, for application to the bubbly flow regime under PWR pressure levels, the proposed EMVD model provides a similar prediction accuracy of the subchannel flow parameters compared with the EVVD models available in MATRA. However, with the EMVD model a better physical interpretation of the individual mixing effects is established. The two different mixing effects, i.e. turbulent mixing and void drift, are separated in the EMVD model. With consideration of the interchannel mixing in the corner-wall subchannel combination, further improvement of the proposed EMVD model is expected.

6.2 Assessment of selected empirical critical heat flux (CHF) correlations

In the current version of MATRA, two empirical CHF correlations: W-3 [96] and B&W-2 [27, 105], are available. In the current study, four additional empirical correlations were implemented in MATRA, namely WSC-2 [10], EPRI-1 [62], GSM.6 [20] and KfK-3 [21]. Validity range of the selected CHF correlations are summarized in Tab. 6.2.

W-3 correlation proposed by Tong [96] is one of the first well-known empirical CHF correlations applicable to rod bundle geometry. It was originally developed on the basis of experiments with single heated channel. For application to rod bundle geometry, correction factors were introduced to account the following effects [66, 97]:

- Non-uniform axial heat flux profiles
- Grid spacer
- Unheated boundary wall

The effect of a non-uniform axial heat flux distribution on the predicted CHF in a rod bundle is evaluated with a heat flux shape factor F_c . Effects of radial heat flux distribution and interchannel flow mixing must be considered with a subchannel analysis, for instance with the THINC code [16], since local subchannel flow conditions required in the W-3 correlation depend strongly on the interchannel mixing between laterally interconnected subchannels as well as on the radial heat power gradient. Grid spacer usually serves as a turbulence and interchannel mixing promoter. Its effect on CHF in rod bundle is a function of the axial span between two spacers and is considered with a spacer factor F_S . Finally, unheated boundary walls influence flow conditions inside the peripheral subchannels, since a portion of liquid adhering to the unheated walls does not contribute to heat transfer. The predicted CHF inside the peripheral subchannels should be corrected with an unheated-wall factor.

Based on measured CHF data in a 3×3 square rod bundle with uniform axial and radial heat flux profiles, Gellerstedt et al. [27] proposed the B&W-2 correlation. Subchannel flow parameters were calculated with an internal interchannel mixing code, which considers only the effect of turbulent mixing between adjacent subchannels with a mixing coefficient of 0.06. Diversion cross flow is neglected. Correction factor of the non-uniform axial heat flux distribution was proposed by Wilson et al. [105] based on Tong's proposal [96] as applied in the W-3 correlation. Due to its relative narrow pressure range of validity (140 to 160 bar), the B&W-2 correlation should be mainly applied to the PWR conditions.

Bowring [10] developed the WSC-2 correlation based on CHF data obtained with various rod clusters simulating fuel assemblies of both BWR and PWR. The subchannel flow conditions were calculated with the subchannel analysis code HAMBO [11]. The non-uniformity of radial power profile is considered with a radial power factor F_P . For the considered subchannel at a given axial position, F_P is defined as the ratio of the local heat flux from the most highly heated rod defining the subchannel to the local radial-average heat flux of the subchannel. A factor Y is used to consider the effect of non-uniform axial heat flux profile. At a given axial position, Y is defined as the ratio of the average heat flux from inlet to the considered axial position to the radial-average heat flux directly at the considered axial position. An further subchannel imbalance factor Y' considering the effect of interchannel mixing is also introduced, which is defined as the ratio of the enthalpy increase in the considered subchannel to the heat released to the subchannel (due to heated rods defining the subchannel). Y' is a measure of the subchannel imbalance relative to its neighbors. For subchannels losing flow $Y' < 1$ and

Tab. 6.2: Validity range of selected empirical critical heat flux (CHF) correlations

	W-3	B&W-2	WSC-2	EPRI-1	GSM.6	KfK-3
Fluid	Water	Water	Water	Water	Water & Freon-12	Water
Pressure [MPa]	6.9 to 15.8	13.8 to 16.5	3.4 to 15.9	1.4 to 16.9	7.6 to 16 & 1.2 to 2.9	2.8 to 160
Mass flux [$kgm^{-2}s^{-1}$]	1356 to 6780	1329 to 5424	271 to 5017	271 to 5560	2000 to 8000 & 2000 to 9000	678 to 5966
Local equilibrium quality [-]	-0.15 to 0.15	-0.03 to 0.20	-0.2 to 0.86	-0.25 to 0.75	-0.2 to 0.4	-0.52 to 0.96
Hydraulic diameter [mm]	5.08 to 17.78	5.08 to 12.70	5.08 to 30.48	8.89 to 13.97	4.54	2.30 to 6.60
Geometries	Single channel	Bundle	Bundle	Bundle	Bundle	Bundle
Spacer	None	Gird spacer	Gird spacer	Gird spacer	Gird spacer	Gird spacer & wire wrap
Subchannel analysis code	THINC	Internal code	HAMBO	COBRA-IIIC	FLICA	None

for subchannels gaining flow $Y' > 1$. The effect of spacers on CHF is taken into account with a spacer factor V . In the WSC-2 correlation, the factor V is assumed to be constant. A value of 1.0 is recommended for normal BWR and PWR grid spacers without mixing vanes.

Based on the WSC-2 correlation, Dalle Donne [21] refitted the factors F_P and Y by using measured CHF data obtained with a tight lattice and proposed the KfK-3 correlation. The KfK-3 correlation was developed for boiling crisis occurring in central subchannels of relative larger rod bundles. No subchannel analysis was carried out in the development of the KfK-3 correlation. In order to obtain mass flux of the considered center subchannels, a correction factor F_G was proposed to correlate the mass flux in the center subchannel with the given bundle average mass flux. When applying the KfK-3 correlation to small rod bundles, it is recommended by the authors [21] that a subchannel analysis should be performed to obtain subchannel mass flux. Furthermore, the subchannel imbalance factor Y' proposed in the WSC-2 correlation should also be used. Similar to the WSC-2 correlation, a correction factor of the grid spacer effect is considered in the KfK-3 correlation. Rather than a constant value for the grid spacer factor V , a new relation taking into account the mass flux influence on the grid spacer effect was developed. Furthermore, the relation of factor V was extended to application in rod bundles with wire wrap.

The EPRI-1 correlation proposed by Reddy and Fighetti [62] was developed with test data obtained with 65 test sections simulating both PWR and BWR fuel assemblies. The COBRA-IIC subchannel analysis code [68] was employed to determine subchannel flow parameters. Regarding interchannel mixing, a simple equal-mass (EM) model (see chapter 3.2.1) was used with a constant turbulent mixing coefficient β of 0.02. The EPRI-1 correlation is applicable to a wide range of flow parameters covering not only BWR and PWR normal working conditions but also accident conditions.

The GSM.6 correlation [20] was developed in the framework of French thermal-hydraulic program addressing future PWR designs using test data obtained with a tight 19-rod bundle in triangular arrangement. The axial heat profile was uniform and the 7 central rods were overheated by 30%, so that boiling crisis was forced to occur at the central rods. Subchannel analysis code FLICA [60] was used to calculate local subchannel flow parameters. Single phase measurement was used to determine pressure drop coefficient of grid spacer and interchannel mixing coefficient. These coefficients were then used to determine the subchannel flow parameters under two-phase conditions. The CHF tests were carried out with Freon-12 to reduce the experimental costs. For application to water, the scaling laws established by Stevens et al. [see 20] was used. Due to the limited range of investigated rod bundle geometries, the GSM.6 correlation is mainly applicable to tight triangular lattices. Furthermore, the effect of non-uniform axial heat flux distribution as well as the effect of unheated cold wall were not considered in the GSM.6 correlation.

For assessment of the selected empirical CHF correlations, the high pressure rod bundle DNB (departure from nucleate boiling) benchmark conducted by Rosal et al. [66] was chosen in the current study as the experimental data base. The 2.44 m long test rod bundle consisted of 16 rods with a 10.72 mm outer diameter arranged in a 4×4 square array on a pitch distance of 14.10 mm. The pitch to diameter ratio was 1.315. Rod spacing was maintained by grid spacers with mixing vanes and simple support grids without mixing vanes. Sheathed thermocouples inside the rods were employed to detect DNB occurrence. The maximal measurement error of CHF was assumed to be 6.6% [66]. Due to the fact that forced interchannel mixing induced by mixing vanes is not considered in the current study, only the test sections IV, V and VI of [66] without mixing vanes were selected for recalculation in the current study. In all 76 test cases were recalculated, for which the covered flow parameter ranges are summarized in Tab. 6.3.

Tab. 6.3: Summary of flow parameters of selected test cases from [66]

system exit pressure	100 <i>bar</i> to 170 <i>bar</i>
inlet temperature	246.7° <i>C</i> to 328.9° <i>C</i>
bundle average mass flux	2034 $kgm^{-2}s^{-1}$ to 5357 $kgm^{-2}s^{-1}$
local equilibrium quality at CHF occurrence	-12.7% to 9.4%

In the current study, local flow conditions at the position where boiling crisis was detected in the experiments were directly substituted into the selected empirical correlations to calculate the predicted CHF q_{CHF}^{calc} . The local flow conditions were obtained with subchannel analysis using MATRA. Relevant models used in the subchannel analysis are summarized in Tab. 6.4. Regarding two-phase interchannel mixing, the proposed EMVD model and the two types of

Tab. 6.4: MATRA models for recalculation of the high pressure rod bundle DNB benchmark [66]

Pressure drop models	
Single phase turbulent friction factor	$0.184 \cdot Re^{-0.2}$
Two phase friction multiplier	Armand model
Grid spacer pressure lost factor	1.0
Quality-void relations	
Subcooled boiling void fraction	Levy model
Saturated boiling void fraction	Modified Armand model
Interchannel mixing models	
Diversion cross flow resistance factor	0.5
Single phase turbulent mixing coefficient	0.005
Two-phase turbulent mixing coefficient	Beus model
Two-phase interchannel mixing models	EMVD EVVD, $K_{VD} = 1.4$ EVVD, $K_{VD} = f(p, x)$

EVVD models available in MATRA were used. Fig. 6.4 presents the predicted CHF q_{CHF}^{calc} obtained with the six selected empirical CHF correlations, versus the measured CHF q_{CHF}^{exp} . In the figure, both q_{CHF}^{calc} and q_{CHF}^{exp} were normalized with the maximal measured CHF of the 76 selected test cases. The two dashes lines denote +20% and -20% relative deviation, respectively.

The B&W-2 correlation fails to predict the measured CHF values reasonably. Relative large scattering of the data points are also observed. This is perhaps due to the relative narrow application range of pressure. The WSC-2 correlation and the KfK-3 correlation show a much better prediction performance than the B&W-2 correlation. However, an large overprediction of the measured CHF values, especially at high heat flux range, is still to be observed. A better prediction can be achieved with the W-3 correlation. The best prediction performance is provided by the EPRI-1 and the GSM.6 correlation. Compared to the W-3 correlation, scattering of data points obtained with these two correlations are much smaller. Since the GSM.6 correlation was developed for tight triangular lattices and the effect of non-uniform axial heat flux distribution was not considered, it is not recommended for application with PWR assemblies. For application to PWR working conditions, the EPRI-1 CHF correlation is hence recommended. Furthermore, Fig. 6.4 reveals that with the three different interchannel mixing models, no large difference in the predicted critical heat flux is observed. Apparently, in bubbly flow regime under PWR pressure level, the effect of interchannel mixing on CHF prediction is of less importance.

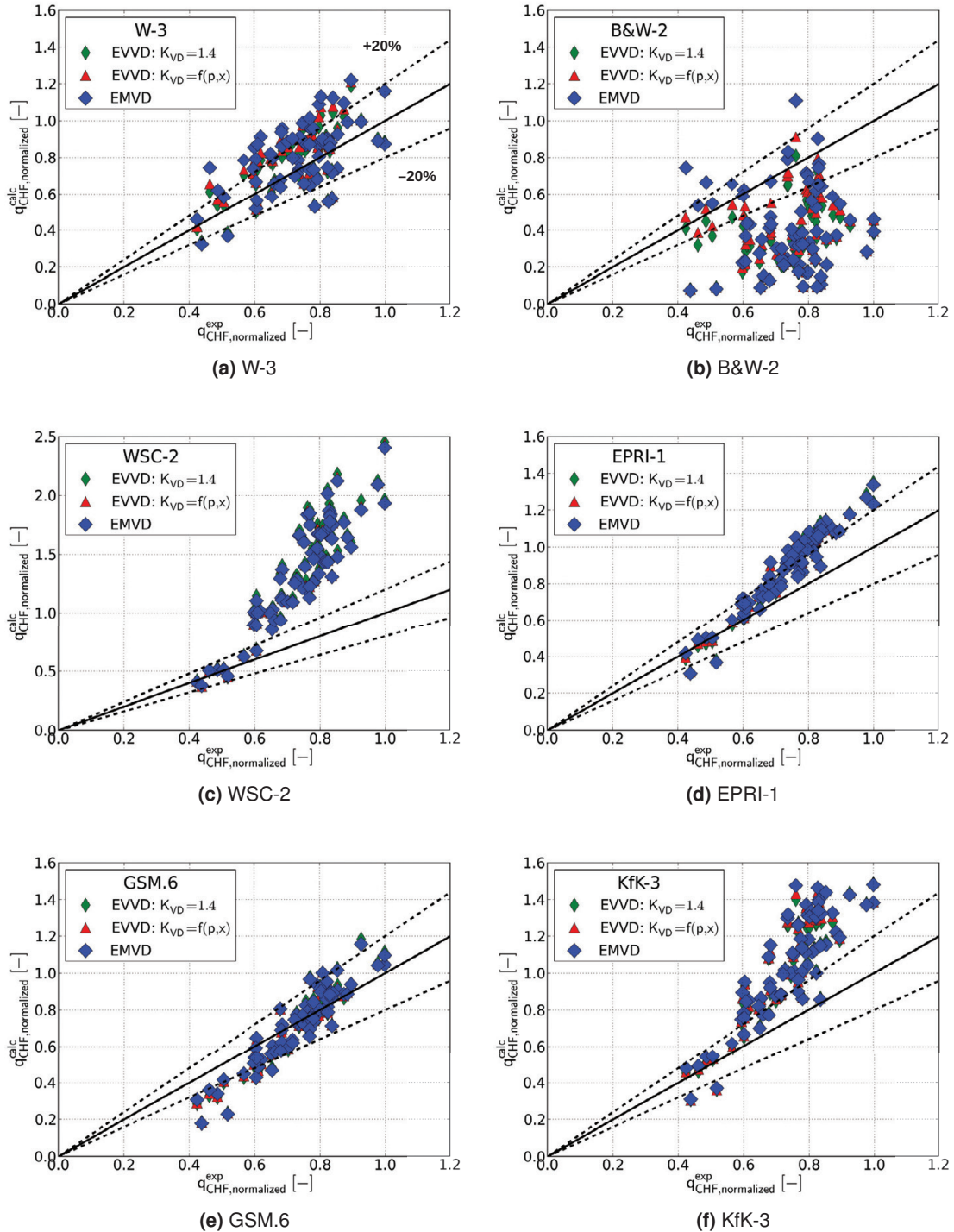


Fig. 6.4: Assessment of the selected empirical CHF correlations.

7. Conclusion and outlook

Prediction of CHF in rod bundle requires local subchannel flow conditions, which depend strongly on modeling of interchannel mixing. Subject of the present study is the natural two-phase interchannel mixing in rod bundle, which can be decomposed into three elemental components [47, 72]: namely turbulent mixing (TM), diversion cross flow (DC) and void drift (VD). Of the three elemental mixing effects, the physical mechanism of void drift is not yet well understood. In the present study, a systematic numerical simulation and analysis of the two-phase interchannel mixing phenomena was performed using the subchannel analysis code MATRA [107] and the CFD code Ansys CFX [2]. A modified interchannel mixing model was proposed and validated with available rod bundle benchmark results. Finally, six selected empirical CHF correlations were assessed by recalculating a high pressure rod bundle DNB benchmark. The most important conclusions obtained are summarized as follows:

- An intensive literature review on experimental investigations conducted for two-phase interchannel mixing phenomena in the past several decades indicated that the key parameters affecting two-phase interchannel mixing are mass flux, void fraction and geometry of interacting subchannels.
- Based on a recalculation of selected test cases from rod bundle benchmarks under both BWR and PWR pressure levels with MATRA, an improvement demand of the interchannel mixing model currently available in MATRA (the EVVD model) was identified for application to bubbly flow regime under PWR pressure level. The improvement should be performed with respect to two aspects:
 - First aspect regards the model used in the EVVD model for evaluating the void fraction difference at equilibrium state between two interacting subchannel. The assumption that void moves towards subchannel with larger mass flux is apparently not valid for bubbly flow regime under PWR pressure level. A better prediction accuracy of the subchannel flow parameters was achieved, if an opposite trend of void migration from subchannel of larger mass flux towards subchannel of lower mass flux is specified. This observation indicated that the modeling of the void fraction distribution at equilibrium state needs improvement for the bubbly flow regime under PWR pressure level. Furthermore, geometrical effect on the void fraction distribution at equilibrium state should also be considered.
 - The combined modeling of turbulent mixing and void drift with the same effective mixing velocity in the EVVD model is also questionable, since turbulent mixing is a non-directional mixing effect, while void drift induces interchannel mixing with a defined direction. In the improved model, the two mixing effects should be separately considered and modeled.
- Simulations of the two-phase interchannel mixing in the bubbly flow regime were conducted with CFD approach using the Eulerian two-fluid model. The liquid phase was

modeled as a continuous phase, while the gaseous phase was assumed to be dispersed bubbles with a constant bubble diameter. Validation of the employed CFD models revealed that the modeling of lift force has a strong impact on the predicted interchannel mixing. By recalculating selected test cases conducted by van der Ros [101] and Gonzalez-Santalo and Griffith [29], a constant lift force coefficient of 0.05 was recommended in the present study for the usage in bubbly flow regime. However, it must be mentioned that more fundamental investigations on lift force should be conducted in the future for more physical understandings of the lift force.

- The void fraction distribution at equilibrium state was investigated with the validated Eulerian two-fluid model. Based on a systematic CFD analysis covering PWR working conditions, a new model based on Levy's proposal [51] was developed for evaluating the void fraction distribution at equilibrium state in the bubbly flow regime under PWR pressure level. It revealed that both mass flux difference and geometrical difference between two interacting subchannels have influence on the void fraction distribution at equilibrium state.
- A new type of interchannel mixing model was proposed for bubbly flow regime under PWR pressure level. Since turbulent mixing was assumed to be equal-mass based, this new type of interchannel mixing model is referred to as the equal-mass-exchange turbulent mixing and void drift (EMVD) model. Compared to the EVVD model currently available in MATRA, one important feature of the EMVD model is the separate consideration of the three elemental mixing effects. With the EMVD approach, a more physical interpretation of the two-phase interchannel mixing is established. Validation of the proposed EMVD model was carried out by recalculating selected test cases in the bubbly flow regime from the ISPRA benchmark [31].
- Six empirical CHF correlations were selected and assessed with both EVVD and EMVD interchannel mixing models by recalculating the high pressure DNB benchmark conducted by Rosal et al. [66]. The EPRI-1 [62] correlation showed overall the best performance and is hence recommended for application under PWR working conditions.

As outlook for future works, the following points should be mentioned:

- In the current study, validation of the Eulerian two-fluid model was carried out based on subchannel average flow parameters. Three-dimensional measurement data, such as lateral void fraction distribution, individual phase velocity profile, two-phase turbulent quantities and bubble diameter distribution, are still desired for validation of the Eulerian two-fluid model regarding its application to predict two-phase interchannel mixing phenomena.
- As identified in the validation calculation of the EMVD model, interchannel mixing between the corner and wall subchannel should also be considered, in order to further improve the proposed void drift model.
- As mentioned above, more experimental and numerical investigations on lift force should be carried out in the future, for as found in the current study that modeling of the lift force has strong impacts on the predicted interchannel mixing.

Bibliography

- [1] H. Anglart, O. Nylund, N. Kurul, and M. Z. Podowski. CFD prediction of flow and phase distribution in fuel assemblies with spacers. *Nuclear Engineering and Design*, 177:215–228, 1997.
- [2] *ANSYS CFX - Solver Theory Guide*. Ansys Inc., 2009.
- [3] S. P. Antal, R. T. Lahey, Jr, and J. E. Flaherty. Analysis of phase distribution in fully developed laminar bubbly two-phase flow. *International Journal of Multiphase Flow*, 7: 635–652, 1991.
- [4] T. R. Auton, J. C. R. Hunt, and M. Prud'homme. The force exerted on a body in inviscid unsteady non-uniform rotational flow. *Journal of Fluid Mechanics*, 197:241–257, 1988.
- [5] Maria Avramova. *Development of an innovative spacer grid model utilizing computational fluid dynamics within a subchannel analysis code*. PhD thesis, The Pennsylvania State University, The Graduate School, College of Engineering, 2007.
- [6] E. Baglietto. Anisotropic turbulence modelling for accurate rod bundle simulations. In *ICONE13*, Miami, Florida, USA, 2006.
- [7] E. Baglietto and H. Ninokata. CFD modelling of secondary flows in fuel rod bundles. In *NUTHOS-6*, 2004.
- [8] A. Behzadi, R. I. Issa, and H. Rusche. Effects of turbulence on inter-phase forces in dispersed flow. In *Proceedings of the 4th International Conference on Multiphase Flow (ICMF 2001)*, New Orleans, LA, USA, 2001.
- [9] S. G. Beus. A two-phase turbulent mixing model for flow in rod-bundle. Technical Report WAPD-T-2438, Bettis Atomic Power Energy, 1971.
- [10] R. W. Bowring. WSC-2: a subchannel dryout correlation for water-cooled clusters over the pressure range 3.4-15.9 MPa (500-2300 psia). Technical report, United Kingdom Atomic Energy Authority, 1979.
- [11] R.W. Bowring. HAMBO - a computer program for the subchannel analysis of the hydraulic and burnout characteristics of rod clusters. Part 2: the Equations. Technical Report AEEW-R582, 1968.
- [12] Alan Burns, Thomas Frank, Ian Hamill, and Jun-Mei Shi. The Favre averaged drag model for turbulent dispersion in Eulerian multi-phase flows. In *Proceedings of the 5th International Conference on Multiphase Flow (ICMF 2004)*, Yokohama, Japan, 2004.
- [13] L. N. Carlucci, N. Hammouda, and D. S. Rowe. Two-phase turbulent mixing and buoyancy drift in rod bundles. *Nuclear Engineering and Design*, 227:65–84, 2004.

- [14] Frank S. Castellana and Joseph E. Casterline. Subchannel flow and enthalpy distribution at the exit of typical nuclear fuel core geometry. *Nuclear Engineering and Design*, 22:3–18, 1972.
- [15] D. Chang and S. Tavoularis. Unsteady numerical simulations of turbulence and coherent structures in axial flow near a narrow gap. *Transactions of the American Society of Mechanical Engineers*, 127:458–466, 2005.
- [16] H. Chelemer et al. THINC-IV - an improved program for thermal-hydraulic analysis of rod bundle cores. Technical Report WCAP-7956, 1973.
- [17] B. Chexal, G. Lellouche, J. Horowitz, and J. Healzer. A void fraction correlation for generalized applications. *Progress in Nuclear Energy*, 27(4):255–295, 1992.
- [18] D. Chisholm. Void fraction during two-phase flow. *Journal of Mechanical Engineering Science*, 15:235–236, 1973.
- [19] R. Clift, J. R. Grace, and M. E. Weber. *Bubbles, drops and particles*. Academic Press, New York, U.S.A., 1978.
- [20] M. Courtaud, R. Deruaz, and L. G. D’Aillon. The French thermal-hydraulic program addressing the requirements of future pressurized water reactors. *Nuclear technology*, 80:73–82, 1988.
- [21] M. Dalle Donne. CHF-KFK-3: a critical heat flux correlation for triangular arrays of rods with tight lattices. Technical report, Kernforschungszentrum Karlsruhe, 1991.
- [22] F. W. Dittus and L. M. K. Boelter. *Heat transfer in automobile radiators of the tubular type*. University of California publications in engineering, 1930.
- [23] J. H. Ferziger and M. Peric. *Computational methods for fluid dynamics*, chapter 9.4 RANS models, pages 292–306. Springer, 2002.
- [24] T. Frank, P. J. Zwart, E. Krepper, H.-M. Prasser, and D. Lucas. Validation of CFD models for mono- and polydisperse air-water two-phase flows in pipes. *Nuclear Engineering and Design*, 238:647–659, 2008.
- [25] Thomas Frank, Junmei Shi, and Alan D. Burns. Validation of Eulerian multiphase flow models for nuclear safety applications. In *Proceedings of the 3rd International Symposium on Two-Phase Flow Modelling and Experimentation*, 2004.
- [26] S. Geçay, Alberto Teyssedou, and Peter Tye. Lateral mixing mechanisms in vertical and horizontal interconnected subchannel two-phase flows. *Nuclear Technology*, 138: 140–161, 2002.
- [27] J. S. Gellerstedt, R. A. Lee, W. J. Oberjohn, R. H. Wilson, and L. J. Stanek. Correlation of critical heat flux in a bundle cooled by pressurized water. *Two-Phase Flow and Heat Transfer in Rod Bundles*, pages 63–71, 1969.
- [28] Markus Glück. *An overview about modelling approaches for turbulent mixing and void drift in sub-channel analysis*, chapter 2. Nova Science Publishers, Inc., 2009.
- [29] J. M. Gonzalez-Santalo and Peter Griffith. Two-phase flow mixing in rod bundle sub-channels. *ASME*, 72-WA/NE-19, 1972.
- [30] H. Grotjans and F. Menter. Wall functions for general application cfd codes. In *Proceedings of the 4th ECCOMAS Computational Fluid Dynamics Conference*, 1998.

- [31] H. Herkenrath, W. Hufschmidt, U. Jung, and F. Weckermann. Experimental investigation of the enthalpy- and mass flow-distribution in 16-rod clusters with BWR+PWR-geometries and conditions. Technical Report EURO 7575, Joint Research Center Ispra Establishment-Italy, 1981.
- [32] Akitoshi Hotta, Hiroshi Shirai, Mie Azuma, Michio Sadatomi, Akimaro Kawahara, and Hisashi Ninokata. A modified equilibrium void distribution model applicable to subchannel-scale vapor-liquid cross flow model for conventional square and tight lattice BWR fuel bundles. *Nuclear Engineering and Design*, 235:983–999, 2005.
- [33] D.-H. Hwang, Y.-J. Yoo, W.-K. In, and S.-Q. Zee. Assessment of the interchannel mixing model with a subchannel analysis code for BWR and PWR conditions. *Nuclear Engineering and Design*, 199(3):257–272, 2000.
- [34] D.-H. Hwang, J.-J. Jeong, and B.-D. Chung. NUPEC BFBT subchannel void distribution analysis using the MATRA and MARS code. *Nuclear Engineering and Technology*, 41(3):295–306, 2009.
- [35] M. Ishii and N. Zuber. Drag coefficient and relative velocity in bubbly, droplet or particulate flows. *AIChE Journal*, 25:843–855, 1979.
- [36] G. Janssens-Maenhout. *Contribution to the Modelling and Computational Fluid Dynamics of Two-Phase Flows with Heat Transfer*. PhD thesis, University Karlsruhe (TH), 1999. in German.
- [37] A. Kawahara, K. Kano, M. Sadatomi, and M. Tezuka. Experiment and analysis of air-water two-phase flow redistribution due to void drift between subchannels for hydrodynamic non-equilibrium flow. In *Proceedings of The 6th International Conference on Nuclear Thermal Hydraulics, Operations and Safety (NUTHOS-6)*, Nara, Japan, 2004.
- [38] A. Kawahara, M. Sadatomi, K. Kano, Y. Sasaki, and H. Kudo. Void diffusion coefficient in two-phase void drift for several channels of two- and multi-subchannel systems. *Multiphase Science and Technology*, 18(1):31–54, 2006.
- [39] Akimaro Kawahara, Michio Sadatomi, T. Tomino, and Y. Sato. Prediction of turbulent mixing rates of both gas and liquid phases between adjacent subchannels in a two-phase slug-churn flow. *Nuclear Engineering and Design*, 202:27–38, 2000.
- [40] Akimaro Kawahara, Michio Sadatomi, Keiko Kano, and Yuichi Sasaki. Flow redistribution phenomena due to void drift in triangle tight lattice subchannels. In *Proceedings of the 5th International Conference on Multiphase Flow (ICMF'04)*, 2004.
- [41] Akimaro Kawahara, Michio Sadatomi, and Tatsuya Higuchi. Effects of surface tension on two-phase void drift between triangle tight lattice subchannels. *Journal of Engineering for Gas Turbines and Power*, 131:012903/1–8, 2009.
- [42] J. E. Kelly, S. P. Kao, and M. S. Kazimi. THERMIT-2: A two-fluid model for light water reactor subchannel transient analysis. Technical Report MIT-EL-81-014, MIT Energy Laboratory Electric Utility Program, 1981.
- [43] *Input instructions of MATRA X0*. Korea Atomic Energy Research Institute (KAERI), 2003.
- [44] E. Krepper, B. Koncar, and Y. Egorov. CFD modelling of subcooled boiling - concept, validation and application to fuel assembly design. *Nuclear Engineering and Design*, 237:716–731, 2007.

- [45] Eckhard Krepper, Dirk Lucas, and Horst-Michael Prasser. On the modelling of bubbly flow in vertical pipes. *Nuclear Engineering and Design*, 235:597–611, 2005.
- [46] N. Kurul and M. Z. Podowski. On the modelling of multidimensional effects in boiling channels. In *ANS Proceedings of 27th National Heat Transfer Conference*, Minneapolis, MN, USA, 1991.
- [47] R. T. Lahey, Jr and F. J. Moody. *The thermal-hydraulics of a boiling water nuclear reactor*, chapter 4 Boiling Heat Transfer, pages 122–138. American Nuclear Society, 1977. ISBN 0-89448-010-3.
- [48] R. T. Lahey, Jr, B. S. Shiralkar, and D. W. Radcliffe. Mass flux and enthalpy distribution in a rod bundle for single- and two-phase flow conditions. *Journal of Heat Transfer*, 93(2):197–209, 1971.
- [49] R. T. Lahey, Jr, B. S. Shiralkar, D. W. Radcliffe, and E. E. Polomik. Out-of-pile subchannel measurements in a nine-rod bundle for water at 1000 psia. *Progress in Heat and Mass Transfer*, 6:345–363, 1972.
- [50] B.E. Launder and D.B. Spalding. The numerical computation of turbulent flows. *Computer Methods in Applied Mechanics and Engineering*, 3:269–289, 1974.
- [51] S. Levy. Prediction of two-phase pressure drop and density distribution from mixing length theory. *Journal of Heat Transfer*, 85:137–152, 1963.
- [52] S. Levy. Forced convection subcooled boiling - prediction of vapor volumetric fraction. *International Journal of Heat and Mass Transfer*, 10:951–965, 1967.
- [53] P.J. Linstrom and W.G. Mallard, editors. *NIST Chemistry WebBook, NIST Standard Reference Database Number 69*. National Institute of Standards and Technology, Gaithersburg MD, 20899, <http://webbook.nist.gov>, (retrieved January 31, 2013).
- [54] T. J. Liu and S. G. Bankoff. Structure of air-water bubbly flow in a vertical pipe-I. liquid mean velocity and turbulence measurements. *International Journal of Heat and Mass Transfer*, 36(4):1049–1060, 1993.
- [55] D. Lucas, E. Krepper, and H.-M. Prasser. Development of co-current air-water flow in a vertical pipe. *International Journal of Multiphase Flow*, 31:1304–1328, 2005.
- [56] J. Mahaffy et al. Best practice guideline for the use of CFD in nuclear reactor safety applications. Technical report, Nuclear Energy Agency, 2007.
- [57] Kaichiro Mishima and Mamoru Ishii. Flow regime transition criteria for upward two-phase flow in vertical tubes. *International Journal of Heat and Mass Transfer*, 27(5):723–737, 1984.
- [58] K. V. Moore and W. H. Retting. RELAP4: a computer program for transient thermal-hydraulic analysis. Technical Report ANCR-1127, Aerojet Nuclear Company, Idaho Falls, ID, 1973.
- [59] B. Neykov, F. Aydogan, L. Hochreiter, and K. Ivanov. NUPEC BWR full-size fine-mesh bundle test (BFBT) benchmark, volume I: Specifications. Technical Report NEA/NSC/DOC(2005)5 Version 02, OECD Nuclear Energy Agency, 2006.
- [60] R. Plas. Flica iii m - code de calcul thermohydraulique de reacteurs ou de boucles d'essais. Technical Report CEA-N-2418, Commissariat k l'Energie Atomique (CEA), 1984.

- [61] Horst-Michael Prasser, Dirk Lucas, Eckhard Krepper, Dieter Baldauf, Arnd Böttger, Ulrich Rohde, Peter Schütz, Frank-Peter Weiss, Cornelius Zippe, Winfried Zippe, and Jochen Zschau. Strömungskarten und modelle für transiente zweiphasenströmungen. Technical Report FZR-379, Forschungszentrum Rossendorf e.V., 2003. in German.
- [62] D. G. Reddy and C. F. Fighetti. Parametric study of CHF data, Volume 2: a generalized subchannel CHF correlation for PWR and BWR fuel assemblies. Technical Report NP-2609, Volume 2, Electric Power Research Institute, 1983.
- [63] J. T. Rogers and R. G. Rosehart. Mixing by turbulent interchange in fuel bundles. Correlations and influence. *ASME*, 72-HT-53:6–9, 1972.
- [64] J. T. Rogers and A. E. E. Tahir. Turbulent interchange mixing in rod bundles and the role of secondary flows. *ASME*, 75-HT-31, 1975.
- [65] J. T. Rogers and N. E. Todreas. Coolant interchannel mixing in reactor fuel rod bundles single-phase coolants. *Heat Transfer in Rod Bundles*, pages 1–56, 1969.
- [66] E. R. Rosal, J. O. Cermak, L. S. Tong, J. E. Casterline, S. Kokolis, and B. Matzner. High pressure rod bundle dnb data with axially non-uniform heat flux. *Nuclear Engineering and Design*, 31(1):1–20, 1974.
- [67] D. S. Rowe. Crossflow mixing between parallel flow channels during boiling part I. COBRA - computer program for coolant boiling in rod arrays. Technical Report BNWL-371 PT1, Battelle-Northwest, Richland, Wash. Pacific Northwest Lab., 1967.
- [68] D. S. Rowe. COBRA IIIC: a digital computer program for steady state and transient thermal-hydraulic analysis of rod bundle nuclear fuel elements. Technical Report BNWL-1695, Battelle, Pacific Northwest Laboratories, 1973.
- [69] D. S. Rowe and C. W. Angle. Crossflow mixing between parallel flow channels during boiling part II. measurement of flow and enthalpy in two parallel channels. Technical Report BNWL-371 PT2, Battelle-Northwest, Richland, Wash. Pacific Northwest Lab., 1967.
- [70] D. S. Rowe, R. B. Macduff, and R. E. Collingham. Thermal hydraulic subchannel model based on void drift. In *Heat Transfer 1990, Proceedings of the 9th International Heat Transfer Conference*, volume 3, pages 401–406, 1990.
- [71] Henrik Rusche. *Computational fluid dynamics of dispersed two-phase flows at high phase fractions*. PhD thesis, Imperial College of Science, Technology & Medicine, Department of Mechanical Engineering, 2002.
- [72] M. Sadatomi, A. Kawahara, and Y. Sato. Flow redistribution due to void drift in two-phase flow in a multiple channel consisting of two subchannels. *Nuclear Engineering and Design*, 148(2-3):463–474, 1994.
- [73] M. Sadatomi, A. Kawahara, K. Kano, and S. Tanoue. Flow characteristics in hydraulically equilibrium two-phase flows in a vertical 2x3 rod bundle channel. *International Journal of Multiphase Flow*, 30(9):1093–1119, 2004. ISSN 0301-9322.
- [74] M. Sadatomi, K. Kano, A. Kawahara, and N. Mori. Void fraction and pressure drop in two-phase equilibrium flows in a vertical 2x3 rod bundle channel & assessment of correlations against the present subchannel data. *JSME International Journal Series B Fluids and Thermal Engineering*, 49(2):279–286, 2006.

- [75] Michio Sadatomi, Akimaro Kawahara, Tsukasa Kuno, and Keiko Kano. Two-phase void drift phenomena in a 2x3 rod bundle: flow redistribution data and their analysis. *Nuclear Technology*, 152:23–37, 2005.
- [76] Y. Sato and K. Sekoguchi. Liquid velocity distribution in two-phase bubbly flow. *International Journal of Multiphase Flow*, 2:79, 1975.
- [77] Y. Sato, M. Sadatomi, and H. Tsukasima. Two-phase flow characteristics in interconnected subchannels with different cross-sectional areas. In *Proceedings of the 1987 ASME/JSME Thermal Engineering Joint Conference*, volume 5, pages 389–395, 1987.
- [78] L. Schiller and Z. Naumann. A drag coefficient correlation. *Zeitschrift Verein Deutscher Ingenieure*, 77:318, 1935.
- [79] F. A. Schraub, R. L. Simpson, and E. Janseen. Air-water flow structure data for a round tube, concentric and eccentric annulus, and nine-rod bundle. Technical Report GEAP-5739, U.S. Atomic Energy Commission, 1969.
- [80] Kotohiko Sekoguchi, Masayuki Takeishi, Kengo Morikawa, and Katsunori Harada. On the gas-liquid two-phase flow inside two adjacent subchannels with different cross-sectional areas. *Bulletin of the Japan Society of Mechanical Engineers*, 28(236):292–300, 1985.
- [81] G. Sengler, F. Forêt, G. Schlosser, R. Lisdat, and S. Stelletta. EPR core design. *Nuclear Engineering and Design*, 187:79–119, 1999.
- [82] Akimi Serizawa. Turbulence structure of air-water bubbly flow - II. local properties. *International Journal of Multiphase Flow*, 2:235–246, 1975.
- [83] M. E. Shawkat, C. Y. Ching, and M. Shoukri. Bubble and liquid turbulence characteristics of bubbly flow in a large diameter vertical pipe. *International Journal of Multiphase Flow*, 34:767–785, 2008.
- [84] S. L. Smith. Void fractions in two-phase flow: A correlation based upon an equal velocity head model. In *Proceedings of the Institution of Mechanical Engineers*, volume 184, pages 647–664, June 1969.
- [85] R. W. Sterner and R. T. Lahey, Jr. Air-water subchannel measurements of the equilibrium quality and mass-flux distribution in a rod bundle. Technical Report NUREG/CR-3373, Rensselaer Polytechnic Inst., Troy, NY (USA). Dept. of Nuclear Engineering, 1983.
- [86] C. W. Stewart, C. L. Wheeler, R. J. Cena, C. A. McMonagle, J. M. Cuta, and D. S. Trent. COBRA-IV: The model and the method. Technical Report BNWL-2214, BATTELLE Pacific Northwest Laboratories, 1977.
- [87] Satoru Sugawara and Yoshihiro Miyamoto. FIDAS: Detailed subchannel analysis code based on the three-fluid and three-field model. *Nuclear Engineering and Design*, 120: 147–161, 1990.
- [88] Satoru Sugawara, T. Sakai, K. Watanabe, and H. E. C. Rummens. Subchannel analysis by the FIDAS code based on the three-fluid model. *Nuclear Engineering and Design*, 132:253–264, 1991.
- [89] T. Kajishima T. Ikeno. Analysis of dynamical flow structure in a square arrayed rod bundle. *Nuclear Engineering and Design*, 240:305–312, 2010.

- [90] A. Tapucu. Studies on diversion cross-flow between two parallel channels communicating by a lateral slot. I: Transverse flow resistance coefficient. *Nuclear Engineering and Design*, 42(2):297–306, 1977.
- [91] A. Tapucu, S. Y. Ahmad, and S. Geçay. Behaviour of two-phase flow in two laterally interconnected subchannels. In *Heat Transfer 1982, Proceedings of the 7th International Heat Transfer Conference*, volume 5, pages 361–366, 1982.
- [92] A. Tapucu, M. Geçkinli, N. Troche, and R. Girard. Experimental investigation of mass exchanges between two laterally interconnected two-phase flows. *Nuclear Engineering and Design*, 105(3):295–312, 1988.
- [93] A. Tapucu, A. Teyssedou, P. Tye, and N. Troche. The effect of turbulent mixing models on the predictions of subchannel codes. *Nuclear Engineering and Design*, 149(1-3): 221–231, 1994.
- [94] N. E. Todreas and M. S. Kazimi. *Nuclear systems, Volume I: thermal hydraulics fundamentals*, chapter 11.6 Pressure-drop relations, pages 638–665. CRC Press, 2012.
- [95] Akio Tomiyama, Hidesada Tamai, Iztok Zun, and Shigeo Hosokawa. Transverse migration of single bubbles in simple shear flows. *Chemical Engineering Science*, 57(11): 1849 – 1858, 2002.
- [96] L. S. Tong. Prediction of departure from nucleate boiling for an axially non-uniform heat flux distribution. *Journal of Nuclear Energy*, 21:241–248, 1967.
- [97] L. S. Tong. Critical heat fluxes on rod bundles. In *Two-phase flow and heat transfer in rod bundles*, 1969.
- [98] L. S. Tong and G. F. Hewitt. Overall viewpoint of flow boiling CHF mechanisms. *ASME*, 72-HT-54, 1972.
- [99] A. A. Troshko and Y. A. Hassan. A two-equation turbulence model of turbulent bubbly flows. *International Journal of Multiphase Flow*, 27:1965–2000, 2001.
- [100] A. Tsuge, K. Sakata, and Y. Hirao. Abnormal characteristics of two-phase flow in vertical tube banks. *Fluid Flow and Heat Transfer Over Rod or Tube Bundles*, pages 129–142, 1979.
- [101] T. van der Ros. *On two-phase flow exchange between interacting hydraulic channels*. PhD thesis, Eindhoven University of Technology, 1970.
- [102] S. K. Wang, S. J. Lee, O. C. Jones, Jr, and R. T. Lahey, Jr. 3-D turbulence structure and phase distribution measurements in bubbly two-phase flows. *International Journal of Multiphase Flow*, 13(3):327–343, 1987.
- [103] Xia Wang and Xiaodong Sun. Three-dimensional simulations of air-water bubbly flows. *International Journal of Multiphase Flow*, 36:882–890, 2010.
- [104] David C. Wilcox. *Turbulence modelling for CFD*. DCW Industries, Inc., 2006.
- [105] R. H. Wilson, L. J. Stanek, J. S. Gellerstedt, and R. A. Lee. Critical heat flux in a nonuniformly heated rod bundle. *Two-Phase Flow and Heat Transfer in Rod Bundles*, pages 56–62, 1969.
- [106] Yeon-Jong Yoo, Dae-Hyun Hwang, and Don. Evaluation of interchannel exchange models with a subchannel analysis code. In *Heat Transfer 1998, Proceedings of the 11th International Heat Transfer Conference*, volume 6, pages 23–28, 1998.

BIBLIOGRAPHY

- [107] Yeon-Jong Yoo, Dae-Hyun Hwang, and Dong-Seong Sohn. Development of a sub-channel analysis code MATRA applicable to PWRs and ALWRs. *Journal of the Korean Nuclear Society*, 31(3):314–327, 1999.



ISSN 1869-9669
ISBN 978-3-7315-0219-7

